The development of electrical plasma diagnostics for HiPIMS discharges

Thesis submitted in accordance with the requirements of
the University of Liverpool for the degree of Doctor in Philosophy
by
Phitsanu Poolcharuansin

September 2012

Abstract

High power impulse magnetron sputtering (HiPIMS) is a plasma-based thin film deposition technique in which extremely high power pulses are applied to a conventional magnetron sputtering source. As a result, the plasma density in HiPIMS discharges is considerably increased up to $10^{19}\,\mathrm{m}^{-3}$, about three orders of magnitude higher than that in conventional direct current magnetron sputtering (DCMS) discharges. Hence the vapour of the sputtered species becomes highly ionised, leading to remarkable improvement in the microstructure and the properties of depositing films.

To better control the deposition process, it is important to gain insights into the properties and the dynamics of the HiPIMS plasmas. This thesis is associated with the investigations on HiPIMS plasmas using a number of electrical diagnostic tools including a Langmuir probe, a retarding field energy analyser and a gridded quartz crystal microbalance.

It was shown, using a Langmuir probe analysis, that there are three distinct groups of electrons generated during first the $4\,\mu$s of the HiPIMS pulse. These electrons are super-thermal or beam-like electrons with effective temperatures of up to 100 eV, hot electrons with temperatures up to 7 eV and cold electrons with temperatures < 1 eV. As time progresses, however, these electrons develop into single-temperature Maxwellian electrons. Using the retarding field energy analyser located at typical substrate positions, it was found that ions travel to a grounded substrate with an average energy of up to 10 eV during $20-40\,\mu$s into the HiPIMS pulse, and with an energy of $3-5$ eV for the rest of the pulse. Ions escaping to the side of the discharge axis are also investigated using the movable and rotatable retarding field analyser. It was found that ions, circulating with a similar direction as the electron E×B drift in the magnetised region, are able to azimuthally escape from the discharge with a mean velocity of $8\times10^{3}\,\mathrm{m\,s}^{-1}$, unless there are collisions with residual gases. Together with the knowledge of radial electric field, determined from plasma potential, the equations of circular motion of an ion fluid element have been solved numerically. Using a biased quartz crystal microbalance in combination with a gridded electrode, the ionised metal flux fraction in a HiPIMS discharge has been investigated. The average discharge power was varied from 0.3 to 1.3 kW and, irrespective of the power control method used, an associated decrease in the flux fraction (from 50% to 30%) was observed. The mechanisms responsible for this decrease in the time-averaged flux fraction of metal ions are associated with the probability of ionisation of the sputtered species and the effect of the ions returning to the target. Finally, a technique of the superposition of a dc pre-ioniser and a HiPIMS power supply is proposed to operate a HiPIMS discharge at a pressure down to 0.08 Pa. The pre-ioniser provides a background plasma with a density of $10^{15}\,\mathrm{m}^{-3}$ to assist the HiPIMS build-up at the low-pressure range. Using an energy-resolved mass spectrometer, it was demonstrated that the average energy and charge state of ions can be enhanced in the low-pressure operation.

Publications

"Short- and long-term plasma phenomena in a HiPIMS discharge"
P. Poolcharuansin and J.W. Bradley
Plasma Sources Sci. Technol. **19** (2010) 025010

"Plasma parameters in a pre-ionized HIPIMS discharge operating at low pressure"
P. Poolcharuansin, B. Liebig, and J. Bradley
IEEE Trans. Plasma Sci. **38** (2010) 3007

"Time-resolved Langmuir probe measurements in preionised HiPIMS discharge"
P. Poolcharuansin, J.W. Bradley and P.J. Kelly
Materials Technology. **26** (2011) 25

"The evolution of the IEDFs in a low-pressure HiPIMS discharge"
P. Poolcharuansin, J.W. Bradley
Surf. Coat. Technol. **205** (2011) S307

"More evidence for azimuthal ion spin in HiPIMS discharges"
P. Poolcharuansin, B. Liebig and J.W. Bradley
Plasma Sources Sci. Technol. **21** (2012) 015001

"Ionized metal flux fraction measurements in HiPIMS discharges"
P Poolcharuansin, M Bowes, T J Petty, J W Bradley
J. Phys. D: Appl. Phys. **45** (2012) 322001

"Low pressure HiPIMS operation using a pre-ionizer technique"
P. Poolcharuansin and J.W. Bradley
53rd Conference proceedings of the society of vacuum coaters. (2010) 36

"Time-resolved ion energy distribution functions in a HiPIMS plasma using a retarding field analyzer"
P. Poolcharuansin, J.W. Bradley
54th Conference proceedings of the society of vacuum coaters. (2011) 166

"Azimthal ion spin in HiPIMS discharges"
J.W. Bradley, P. Poolcharuansin and B. Liebig
55th Conference proceedings of the society of vacuum coaters. (2012), in accepted

Acknowledgement

This is an opportunity to say “thank you” to people who supported and guided me during my course in University of Liverpool.

I am very grateful to thank my supervisor Prof. James W Bradley for the advice and the help given to me over the years.

I would like to thank Dr Dmitry Samsonov, Dr Paul M Bryant and Dr James L Walsh for their useful comments and discussions.

I also wish to thank Mr Alan Edwards, Mr John Owens and Mr Alan Roby for their technical support in electrical and mechanical works.

Special thanks I would give to all my friends here in technological plasmas group for their nice friendship. Bernd Liebig for his informative comments and collaborations. Dr Jun-Seok Oh for daily discussions during our tea break time. Anurag Mishra for the training he has given during the beginning of the course. Michael Bowes and TJ for fruitful collaborations and their comments on my thesis writing.

I acknowledge the Ministry of Science and Technology in Thailand for a studentship funding.

Contents

List of Figures

List of Tables

Chapter 1

Introduction

Plasmas are ionised gases consisting of a large number of free charged particles, i.e. electrons and ions, in a volume of background neutral species. Unlike ordinary gases, plasma dynamics are dominated by long-range Coulomb interactions instead of short-range head-on collisions. In general, plasmas can be classified thermodynamically into thermal and non-thermal equilibrium states. In the latter case, which is often referred to as technological plasmas, the average temperature of the electrons is about 100 times higher than the temperature of the ions and the neutral species (which are near a room-temperature). These energetic electrons can essentially provide a variety of low-temperature free-space active species, e.g. photons, radicals and ions that are advantageous to many technological applications. For example, photons in the ultraviolet energy range can be emitted from plasmas exciting the phosphor in fluorescent lamps and in flat-panel displays. Chemically active radicals in plasmas can sterilize biomedical tools, purify drinking water and clean up air pollution. Moreover, positive and negative ions generated from plasmas are crucial for instances in chemical etching during microelectronic fabrication and in physical vapour deposition during thin film material synthesis and engineering.

Ionised physical vapour deposition (IPVD) is a plasma-based thin film deposition technique in which the vapour of depositing material is dominated by ionic species rather than neutral particles [1]. Having high fluxes of the ionic species, IPVD potentially offers technological advantages over conventional physical vapour depositions. Firstly, depositing ions can be collimated by the plasma sheath resulting in anisotropic deposition for filling vias and trenches in micro-electronic fabrication. Secondly, bombardment by depositing ions can enhance the surface mobility of a depositing material leading to a denser microstructure and higher adhesion for tribological coatings. Finally, the kinetic energy of depositing ions can be controlled by biasing the substrate, enabling one to adjust the properties of the deposited film.

High power impulse magnetron sputtering or HiPIMS is a recent IPVD device developed by Kouznetsov *et al.* [2] in 1999. HiPIMS is essentially magnetically enhanced

sputtering operated in a pulsed mode in which low-frequency ($50 - 1000$ Hz), short-duration ($0.5 - 20\%$ duty cycle), high-power pulses ($0.2 - 3.0\,\mathrm{kWcm^{-2}}$) are employed to increase the density of magnetised electrons up to $10^{19}\,\mathrm{cm^{-3}}$. As a result, the degree of ionisation of sputtered species is substantially increased. These plasma conditions give rise to considerable improvements to the micro-structure and properties of growing films. The micro-structure of thin films deposited from HiPIMS processes are very dense, void-free structures, with low surface roughness and high adhesion. Consequently, film properties, for example the wear resistance coefficient of CrN, the hardness of TiN and the refractive index of TiO, are remarkably improved in comparison to that of the films grown in a conventional dc magnetron sputtering (dcMS) discharge.

In the last decade, HiPIMS is increasingly interesting not only in thin film industry but also in fundamental research. Many efforts have been made to gather basic parameters and to understand the physics of HiPIMS plasmas through experimental and theoretical works. Basic parameters of HiPIMS plasmas have been spatially and temporally measured using a variety of diagnostic tools. For example, temperature, density and energy distribution of electrons can be measured using Langmuir probes. The composition of the plasmas can be obtained using mass spectrometry or optical emission spectroscopy. The energy distribution of ionic species can be obtained by the use of energy analysers. The density of neutral species both in ground and metastable states can be determined from optical absorption spectroscopy. These basic parameters of HiPIMS plasmas also reveal interesting regimes in the physical phenomena, for example, self-sustained sputtering, discharge runaway, strong gas rarefaction and cross-field azimuthal ion spin. Some of these phenomena in HiPIMS plasmas are not fully understood and need to be investigated in more details, which is the aim of this thesis.

The main propose of this thesis is to better understand physical phenomena in HiPIMS by plasma investigations using a number of plasma diagnostic tools including Langmuir probes, a retarding field analyser and a biased quartz crystal microbalance.

In this thesis, the basic principles of HiPIMS plasmas and research issues are given in Chapter 2. The details of plasma diagnostics are presented in Chapter 3. The investigation of plasma electrons using a Langmuir probe are discussed in Chapter 4. The technique to operate a HiPIMS discharge in a very low pressure range is demonstrated in Chapter 5. The measurements of the ion velocity distribution function and related parameters using a retarding field analyser are performed in Chapter 6. Chapter 7 deals with the nature of azimuthal ions spinning in HiPIMS plasmas. The ionised metal flux fraction is investigated in Chapter 8. Finally, the conclusions of the thesis and suggestions for future work are given in Chapter 9.

Chapter 2

Literature review

In this chapter, fundamental concepts underpinning HiPIMS plasmas are summarised. It includes general concepts and processes of plasmas and magnetron sputtering. Further comprehensive details of these concepts and processes are given in the textbooks of plasma processes and thin film deposition [3–6]. In the latter part of this chapter, the general perspective on HiPIMS plasmas is also given to point out issues that are relevant to this thesis.

2.1 Plasmas in general concepts

Plasmas have been recognized as the fourth state of matter in addition to solids, liquids and gases. Atoms in a solid have low kinetic energy, and are bound into a rigid structure by, for example an ionic bond. Breaking the bond using sufficient thermal energy, the state can be changed to liquid and then gas through melting and vaporisation, respectively. By supplying more thermal energy, gas atoms may be ionised, becoming free electrons and ions, due to collisions with energetic atoms. The state in which gases are ionised to become charged particles is referred to as the plasmas state.

The most fundamental characteristic of plasmas is its ability to neutralise the electrical charges. In other words, plasmas are quasi-neutral, i.e., charges in plasmas are conserved. For example, in singly charged plasmas, the electron density is approximately equal to the density of singly charged ions. Any perturbation from external electric fields is shielded within a specific space and time. The length from the perturbing sources that plasmas can shield is determined by the Debye length, λ_{De}. The time that plasmas can respond to shield is given by the inverse of plasma frequency, ω_e. Both λ_{De} and ω_e depend on the fundamental parameters including electron temperature T_e and electron density n_e. Other plasma parameters involved with space and time are often considered as a function of λ_{De} and ω_e, respectively.

Plasmas can be classified into two main groups, namely, thermal and non-thermal plasmas. On the one hand, plasmas generated in high temperature environments are often referred to as thermal plasmas. In these kinds of plasmas, the temperature of con-

stituent species, i.e., electrons, ions and neutrals, are nearly identical and much higher than room temperature. In technological applications, thermal plasmas are suitable for processes that require extremely high temperatures, e.g., plasma spraying, welding and cutting. Plasmas, on the other hand, can also be generated at lower temperature. In this case, electrons are heated, using external electric fields, to temperatures on the order of 10^5 K. Gas atoms can be ionised effectively during inelastic collisions with energetic electrons. In this way, the temperature of ions and neutrals remains at room temperature. These types of plasmas are known as non-thermal plasmas and are the subject of the thesis.

2.1.1 Fundamental processes of non-thermal plasmas

Gas state processes, both in the plasma bulk and at the boundary, are mainly involved with neutral particles. Unlike ordinary gases, non-thermal plasmas contain an amount of charged particles in addition to the residual neutral atoms. In the plasma bulk, collisions between charged particles and residual neutrals are of importance, in addition to collisions between neutrals. At the boundary, charged particles also interact with any surface that is adjacent to it. The collisions in the plasma bulk and interactions at the plasma boundary cause a number of subsequent processes that are vital in technological applications. The important processes in non-thermal plasmas are summarised as follows.

Inelastic collisions between electrons and residual neutrals are one of the most important events in the plasma bulk. The kinetic energy of the electrons is effectively transferred to the neutrals causing a variety of collisions processes, e.g. dissociation, excitation, ionisation. As a result, radicals, excited species, photons and positive or negative ions can be generated. Those species generated in the plasma bulk are crucial and employed in a wide range of applications. For example, radicals such as ozone (O_3), are utilised to purify water. Photons in a specific energy range are used in laser technology and lighting systems. Positive and negative ions are useful for surface engineering, by chemically and physically reacting with a surface.

Plasmas are separated from any surfaces, e.g. the vessel wall, electrodes or probes, by a space charged sheath, called a plasma sheath. A plasma sheath is formed due to the fact that electrons move much faster than massive ions. For example, electrons collide with a floating wall more often than ions in a set time. This means that the electron flux at the wall is higher than the flux of ions. Given that the wall is electrically floating, the electron and ion flux at the wall must be identical. To balance these fluxes of charge carriers, electrons need to be suppressed out, and ions need to be accelerated in, to the wall. This requirement breaks down the neutrality and forms a thin layer of positive space charged sheath or plasma sheath due to the build-up of ions near the wall.

Plasma sheaths accelerate ions from the plasma bulk to the walls with a particular kinetic energy depending on the potential different between the wall and the plasmas. If the wall potential is negative with respect to the plasma potential, positively charged ions are thus accelerated to the wall and may cause a number of processes which are described below.

Secondary electron emission: A solid surface, when bombarded by energetic particles, can emit free electrons. Ions accelerated through a plasma sheath can be used as the energetic particles bombarding a surface in the vicinity of the plasma. The free electrons produced from a surface are crucial to generate and sustain non-thermal plasmas. These free electrons are often known as secondary electrons. Secondary electrons can effectively couple or absorb the energy from the electric field in the plasma sheath. When entering to plasma bulk, the secondary electron transfers its energy to other species via inelastic collisions. The number of secondary electrons produced by an incident ion is referred to as secondary electron emission yield, γ_{se}. Normally, γ_{se} is about 0.1 for metals.

Sputtering: If the kinetic energy of the bombarding ions is high enough, atoms of the bombarded surface can be ejected out into a vapour. This process is known as sputtering. The vapour of sputtered atoms then diffuse from the target surface and condense as a thin film on other surfaces nearby. This is one of the established methods to deposit thin films. The details of sputtering as a thin film deposition tools are given in the next section.

2.2 Sputtering

Sputtering is the physical process in which atoms are ejected from a surface due to bombardment by energetic particles. The energetic particles may be neutral particles or ions. In most cases, ions at the plasma boundary are used as sputtering particles due to them being accelerated towards a surface. In thin film technology, sputtering is categorised as a physical vapour deposition (PVD) technique. To understand the principles of sputtering processes for thin film deposition, a simple dc diode system is employed as shown in figure 2.1.

A dc diode sputtering system consists of a vacuum system, a sputter source, a negative dc power supply and a substrate. The vacuum system including the vessel, the pumps and the relevant vacuum devices is used to establish, monitor and control the operating pressure of the order of a few hundred mTorr. The diode sputter source is simply a metallic electrode used as a target in the sputtering process. The target is connected to a negative dc power supply, while the vessel is electrical grounded. A substrate, the object that is being deposited with the sputtered vapour, is placed several centimetres away from the target surface.

In thin film deposition, there are three fundamental processes to be considered,

namely vapour generation, transportation and condensation. Initially, a plasma of an inert gas, commonly argon, is formed. The ions at the plasma boundary in the vicinity of the target are accelerated through a high voltage plasma sheath toward the target surface. The kinetic energy of the sputtering ions can be gained to the energy that corresponds to the target voltage which is normally in the range of several hundred volts. Atoms at the target surface are sputtered by momentum transfer and cascade collision mechanisms. The sputtered vapour then diffuses outward from the target surface toward the substrate. When the sputtered flux reaches the substrate surface, where the temperature is lower than the melting point of the target material, it condenses back to a solid state, forming a thin film over the substrate surface.

The main drawback of sputtering is the low rate of deposition compared with that from other PVD techniques, for example thermal and electron-beam evaporations. The rate of deposition for a given target material and a target voltage mainly depends on the density of the argon ions which relates directly to the density of the argon neutrals and the electrons in the system. Through increasing the number of argon neutrals in the chamber by increasing the operating pressure, the population of the positive argon ions in the plasma may be potentially increased. Nevertheless, numerous researches have shown that there is an optimum point for the operating pressure to achieve a high deposition rate. It means that the deposition rate will be reduced if the processes are operated at a pressure higher or lower than the critical pressure. Alternatively, increasing the electron density by plasma confinement near the target surface using external magnetic fields is the most effective means for increasing the density of argon ions. This strategy is one of the breakthroughs of sputtering technology and it is referred to as "magnetron sputtering".

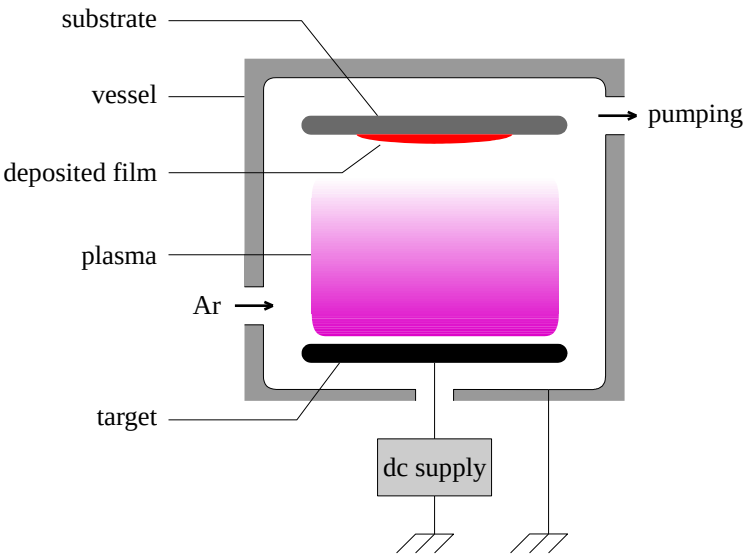

Figure 2.1: A simple diagram of a dc diode sputtering system

2.3 Magnetron sputtering

Magnetron sputtering is a magnetically enhanced sputtering technique in which an external magnetic field with a specific design is used to increase the plasma density, and hence deposition rate. Magnetron sputtering can operate with a higher deposition rate at a lower working pressure (1-5 mTorr) and a lower electric potential (300 – 700 V) in comparison with conventional sputtering [7]. Thornton has given the definition of the magnetron sputtering source in [8] as follows:

"Magnetron sputtering sources can be defined as diode devices in which magnetic fields are used in concert with the cathode surface to form electron traps which are so configured the E×B electron-drift currents can close on themselves."

Over decades, various types of magnetron sputtering sources have been invented and investigated. Magnetron sources may be separated into three main categories using the criteria of target shape, magnetic configuration and driving power supply.

A sputtering target connected to a magnetron source may be presented in different geometries, including post, hollow cylinder, conical, hemispherical and planar magnetron. The planar magnetron sources, being one of the oldest geometries, is still one of the most commonly used today. In additional to planar sources, there have been two types of target shapes: a disk shape and a rectangular shape, referred to as the circular magnetron and rectangular planar magnetron, respectively [7–10].

The second criterion is the configuration of magnetic field lines in front of the target surface, known as balanced and unbalanced configurations. In the case of balanced magnetrons, the magnetic field lines are very dense and extend only short distances from target surface. It means that the substrates placed far away from the target are almost separated from the magnetized plasma. The structure of thin films developed in a balanced configuration has been found to be far from a fully dense structure due to the lack of ion bombardment during the film growth. In an unbalanced configuration, magnetic fields extend from the target region toward the substrate region. This extension of the magnetic fields guides the electrons, and hence ions, from the confinement zone to the depositing area. Bombardment of the ions during the film growth can increase the surface mobility of the depositing atoms. As a result, the microstructure of growing films significantly improves.

The last criterion to classify the magnetrons is the type of driving power applying to the target. A negative dc power source is a very simple and inexpensive configuration compared with other types of power supply. However, dc power supplies are only suitable for metallic or or metallic compound targets, not for non-metallic targets. When using a dc power supply for a non-metallic target, positively charged particles can build up on the target causing arcing and instability during the sputtering process. Radio frequency (RF) power supplies, operated at a frequency in the range of 5 – 30 MHz, can be employed to deposit the insulated film, in a stable and arcing-free environment.

Nevertheless, a RF sputtering system needs a special design and a matching network to operate, therefore high-cost and complexity need to be taken into account for industrial scales. Alternatively, in a more simplistic way, a pulsed dc power supply can be employed to deposit highly insulating material, especially ceramic films. The pulse waveforms can be either unipolar or bipolar types operated in the range of several hundred kilohertzs [11–13]. Recently, high power pulsed power supplies are employed to increase the degree of ionisation of the sputtered vapour, hence enhance microstructure and properties of depositing films [2].

2.4 High power impulse magnetron sputtering

In 1999, Kouznetsov *et al.* [2] introduced a novel thin film deposition technique which is referred to as high power impulse magnetron sputtering or HiPIMS. They applied voltage pulses with a peak between $-900\,\mathrm{V}$ and $-1600\,\mathrm{V}$ to a conventional magnetron source and found that the peak current density of up to $5\,\mathrm{Acm}^{-2}$ and the peak power density of $2.8\,\mathrm{kWcm}^{-2}$ can be achieved. These values of current and power density for HiPIMS are much higher than that for DCMS which are typically $< 0.05\,\mathrm{Acm}^{-2}$ and $< 0.05\,\mathrm{kWcm}^{-2}$, respectively [14]. Due to the very high peak power, a dense plasma can be produced with a peak ion current density of up to $3.4\,\mathrm{Acm}^{-2}$. Consequently, 70% of the depositing flux at a substrate were then ionised turning the discharge from the metal-neutral-rich to be metal-ion-rich environment. Even though an extremely high power was employed, the average power at the target was still low due to the low repetition rate ($\sim 50\,\mathrm{Hz}$) and the low duty cycle ($< 1\%$) of the voltage pulses. The magnetron was then not over heated in HiPIMS mode.

Several target materials have been employed in HiPIMS discharges to deposit a variety of thin films using non-reactive and reactive processes.

The transition metals such Ti, Cu, Al and Ti have mainly been used as the target in order to investigate the fundamental physics, discharge dynamics and properties of metallic films during a non-reactive HiPIMS process. Metallic films are potentially applied for metallisation in microelectronic fabrications. The challenge of improving the performance of microelectronic devices comes down to depositing metal films in a high-aspect-ratio structure [6]. Metal ions in HiPIMS plasmas are accelerated through the plasma sheath forming in front the substrate [15]. Consequently, metal ions can travel with a normal direction and arrive at the bottom part of the high-aspect-ratio substrate. Carbon is another target material used in non-reactive HiPIMS discharges to deposit amorphous carbon films. Amorphous carbon films in hydrogen-free tetrahedral structure (ta-C) are of interest in a wide range of applications, e.g. for protective coatings and corrosion barriers [16]. DeKoven *et al.* [17] have reported that carbon films deposited using HiPIMS discharges can have densities of up to 2.7 $\mathrm{g/cm}^3$. However, the structure of the films was described as graphite-like rather than diamond-like. This

may be due to a relative low density of carbon ions produced in a HiPIMS plasma. Aijaz *et al.* [18] proposed the method to increase the number of carbon ions using argon and neon as a mixed sputtering gas. Since neon gas has a relatively high ionisation energy (21.56 eV), the electron temperature in the plasma is increased and promotes a high degree of carbon ionisation. They claimed that carbon films with densities of up to 2.8 g/cm^3 can be achieved. The technique suggested in [18] may be another feature of non-reactive HiPIMS discharges used to produce ta-C films.

When a reactive gas (e.g. N_2 and O_2) is introduced, the process is then in a reactive mode and compound films can be formed. Several industrial use films have been implemented using reactive HiPIMS discharges, e.g. Al_2O_3 as a wear protective layer for cutting tools, CrN as anti-corrosion layers, TiN as a diffusion barrier for microelectronic circuits and TiO as a high refractive index layer or a photocatalytic active layer [19–23]. Compared to conventional DC magnetron systems, reactive HiPIMS discharges provide additional process parameters enabling a capability to adjust the phases, structures and properties of growing films. For example, Aiempanakit *et al.* [24] have demonstrated that the density and the refractive index of TiO_2 films can be controlled via the discharge repetition rate. They claim that the maximum film density (4.3 g/cm^3) and the highest refractive index (2.63 at a wavelength of 550 nm) can be achieved using the HiPIMS repetition rate of 2.0 kHz. As reviewed in [25], in addition, the hysteresis problem and the instability of transition zones during reactive modes, for e.g. Al_2O_3, can be alleviated in a HiPIMS discharge. Consequently, stoichiometric films can be synthesised with a high deposition rate.

The main feature of HiPIMS is ability to provide a large number of ions of sputtered material (film ions). This feature lead to the significant improvement in microstructure and properties of the growing films due to the presence of large fluxes of film ions and the ability to control the direction and the energy of the film ions using substrate bias technique [25]. The detail on thin film deposition using HiPIMS can be found in the recent articles reviewed by Sarakinos *et al.* [26] and by Lundin and Sarakinos [25]. However, some thin film applications using the features of HiPIMS are highlighted as follows.

Large ion fluxes for film growth: The ability of the depositing particles to move over a substrate surface, the surface mobility of adatoms, is of importance for film production with a columnar-less microstructure, a smooth morphology and a high film density. The increase of substrate temperature is one of the means to increase the mobility of adatoms, however it is not applicable for thermal-sensitive substrates [27]. Momentum transfer from arriving ions to adatoms during the film growth is an effective approach to increase the surface mobility of adatoms for non thermal-sensitive substrates [25]. Numerous works revealed that the large flux of bombarding ions avail-

able in HiPIMS introduces the high efficiency of momentum transfer to the adatoms resulting in smooth films with a fully dense microstructure [28–30].

Controlling the direction of ions forming the film: Alami *et al.* successfully demonstrated the ability to control the direction of ions forming the film in HiPIMS technique [31]. They synthesized a Ta film on a Si biased substrate located along side a trench using HiPIMS in comparison with DCMS. The Ta films using HiPIMS was developed in the direction normal to the substrate surface. The explanation is that the film ions follow the electric field of the plasma sheath forming adjacent to the substrate. In contrast, the growth direction of DCMS films followed the direction of neutral flux of sputtered species because of the the relatively low density of film ions. The ability to guide the direction of film ions by plasma sheath has also been implemented in the deposition for complex-shaped substrates [32] and for nanometer-size vias [15].

Controlling the energy: In order to tailor the phase composition and hence film properties, one needs to control the energy of film ions by the substrate bias technique. Konstantinidis *et al.* [20] have shown that the high temperature phase of titanium oxide films (rutile phase) can be synthesised using HiPIMS with the substrate bias technique. In fact, the rutile phase can be formed on the grounded substrate but it was more pronounced on the $-150\,\mathrm{V}$ biased substrate. The effect of substrate bias on the phase composition of films can be found in [33]. Lin *et al.* have reported that the phase of Ta films changed from the beta phase to the alpha phase when the substrate bias voltage varied from zero voltage to $-100\,\mathrm{V}$ [33].

Sub-plantation of bombarding ions: Pre-deposition as an inter-layer by HiPIMS has been presented in a number of articles. Lattemann *et al.* reported that owing to cleaning by ion bombardment and intermixing of film ions with a $-400\,\mathrm{V}$ biased substrate during HiPIMS pretreatment, adhesion of CrN film on steel can be significantly enhanced [34]. The critical load L_c from scratch tests, indicating the adhesion of the films, for the DCMS films is typically less than 40 N but can increase up to 65 N for the HiPIMS films. Other studies also show a similar result in which the adhesion of the depositing films can be improved using HiPIMS interfacing layers [35, 36]. The high value of the film adhesion obtained by the HiPIMS process can be explained by the sub-plantation of film ions. Using high voltages between $-600\,\mathrm{V}$ and $-1000\,\mathrm{V}$ biased on a substrate, film ions can gain an energy of $600-1000\,\mathrm{eV}$ for singly charged ions. These energetic ions are able to penetrate in the range of $5-8\,\mathrm{nm}$ beneath the substrate surface and serve as the interfacing layer between the substrate and the growing films.

2.4.1 HiPIMS discharge processes

HiPIMS is a plasma-based deposition technique, meaning that the plasma plays a crucial role in generation, transportation and film formation of depositing species. For example, plasma ions are accelerated toward the magnetron target and cause the ejection of atoms of the target material. The sputtered atoms after moving into the dense plasma can be ionised by the electron-impact ionisation mechanism. Ions of the target material or film ions can either be transported to the substrate for deposition or return back to the target for self-sputtering [37]. In addition, film ions gain more kinetic energy due to acceleration through the plasma sheath forming adjacent to the substrate surface. The energy of film ions can then be controlled by varying the negative voltage applied on the substrate. As a result, microstructure and hence the properties of the depositing film can be adjusted [25]. Understanding the plasma processes and properties in HiPIMS discharges, therefore, is the key to optimise the deposition process and the consequent quality of films.

Several phenomena in HiPIMS discharge are thus far different from other magnetron discharges, e.g DC, RF and pulsed-DC discharges. The physics of HiPIMS discharges has been reviewed by several authors e.g. Helmersson *et al.* [1], Sarakinos *et al.* [26], Anders [38], Lundin and Sarakinos [25] and Gudmundsson *et al.* [14]. Base on these review articles, a brief overview of the physics involved with HiPIMS is summarised as the following paragraphs.

Metal ionisation: There are several mechanisms to ionise the sputtered species in a magnetron sputtering system, e.g. penning ionisation, electron impact ionisation and ion charge exchange [4]. Using a zero dimension global model, it has been shown in [6] that the penning ionisation is important in discharges having $n_e < 10^{17}\,\mathrm{m}^{-3}$, while the electron impact ionisation is the main mechanism to produce metal ions when $n_e > 10^{17}\,\mathrm{m}^{-3}$. Gudmundsson [39] has developed a time-dependent global model to investigate the ionisation mechanism in a HiPIMS discharge. It was reported in [39] that during the pulse on-time phase, where $n_e \sim 10^{19}\ \mathrm{m}^{-3}$, sputtered species are mainly ionised by the electron impact ionisation. In the afterglow plasma when n_e decays, the ion charge exchange mechanism is important in the ionisation process. Recently, Raadu *et al.* [40] established a time-dependent global model that specifically concerns the ionisation region (IR) above the magnetron target. The IR model can be employed to predict internal parameters (e.g. electron temperature, electron density and the degree of ionisation of both the metal and the argon species) of the HiPIMS plasma using discharge variables as the input parameters. For example, using a HiPIMS current with at peak of 100 A, the electron density density can be increased up to $2 \times 10^{19}\,\mathrm{m}^{-3}$. As a result, the degree of ionisation of aluminium reaches a peak of 80-85% [40].

Gas rarefaction: Basically, heating a gas that can expand gives a low density. In a conventional magnetron sputtering system, the density of the sputtering gas can be decreased by momentum transfer from the energetic sputtered particles. A decrease of gas density due to gas heating by the sputtered vapour is known as gas rarefaction. Gas rarefaction is more pronounced in a HiPIMS discharge where considerable fluxes of energetic sputtered species are generated. There have been a number of studies of gas rarefaction in HiPIMS [14]. Alami *et al.* [41] employed optical emission spectroscopy to monitor emission lines from excited atoms (Ar^0 and Cr^0) for different HiPIMS current densities. It was shown in [41] that the temporal ratio intensity of Ar^0/Cr^0 tends to decrease during a HiPIMS pulse of $2.8\,Acm^{-2}$. Kadlec [42] employed the Monte Carlo method to simulate the flow of neutral particles in a HiPIMS discharge. The results in [42] agree well with with measurements in [41] in which sputtering gas density significantly decreases from the initial value during the HiPIMS pulse. Vitelaru *et al.* [43] performed time-resolved tunable diode-laser absorption spectroscopy measurements to determine the temperature and density of the argon metastable (Ar^m) atoms in a HiPIMS discharge. They found that the temperature of Ar^m increases from room temperature at the pulse beginning up to $\sim$1300 K during the pulse on-time. In addition, the temporal densities of Ar^m indicated that the strongest gas rarefaction occurs at the peak of the HiPIMS current waveform. Using an ionisation region model, however, Huo *et al.* [44] have reported that the strong gas rarefaction occurs behind the peak of discharge current with a delay of a few ten microseconds. In HiPIMS discharges, gas rarefaction can directly affect the production of secondary electrons at the magnetron target. To sustain the magnetron plasma, it is important to sustain the generation of the secondary electrons. The number of secondary electrons generated at a target can be determined from the ionisation energy of the bombarding ions [14, 45]. Anders *et al.* [45] pointed out that singly charged metal ions cannot satisfy the condition for secondary electron emission as argon ions do. As a result, the secondary electron emission and the resultant discharge current tend to decrease when the gas rarefaction develops during a HiPIMS pulse. Lundin *et al.* [46] have proposed that the gas rarefaction causes the transition from a high to a low regime of a discharge current waveform.

Self-sputtering: When the peak power density at a magnetron target is greater than $0.5\,kWcm^{-2}$, the electron density in the plasma increases up to $10^{19}\,m^{-3}$ resulting in a considerable ionisation degree of sputtered species. The sputtered species that are ionised near the target can experience the electric field of the cathode fall. This electric field forces low energy ions to return back to the target as sputtering particles. The process, of a target being sputtered by its own particles, is known as self-sputtering. The parameters used to determine the level of self-sputtering is defined as $\Pi_{ss} = \alpha\beta Y_{ss}$,

where α is the ionisation probability of the sputtered neutrals, β is the returning probability of the metal ions and Y_{ss} is the self-sputtering yield [37, 38]. Using the self-sputtering parameter, Π_{ss}, HiPIMS discharges can be operated in: (1) the DCMS-like mode when $\Pi_{ss} < 0.1$, (2) the partially self-sputtering mode when $0.1 < \Pi_{ss} < 1$, (3) the sustained self-sputtering mode when $\Pi_{ss} = 1$ and (4) the runaway self-sputtering mode when $\Pi_{ss} > 1$ [14]. Most HiPIMS discharges can be operated in the DCMS-like and the partially self-sputtering modes. Using a high self-sputtering yield target material such as Cu, Zn and Ag, the discharge can meet the conditions necessary for sustained and runaway self-sputtering. For example, Andersson and Anders [47] reported that a HiPIMS discharge with a copper target can be operated in a mode of sustained self-sputtering at a base pressure of 1.1×10^{-4} Pa. They specified this mode as gasless self-sputtering [47]. Recently, Anders *et al.* [48] proposed a generalised runaway condition by introducing the role of recycling gas particles that outgas from the target. It was shown in [48] that HiPIMS with a low sputtering yield target material, e.g. carbon, can be operated in the runaway mode using a target voltage of > 1150 V at 1 Pa of argon.

Deposition rates: In HiPIMS discharges, the deposition rates (R_{HiPIMS}) are typically lower than the deposition rates (R_{DC}) from a conventional DC magnetron sputtering operating with the same average power, i.e. $R_{\mathrm{HiPIMS}}/R_{\mathrm{DC}} < 1$, depending on the target material [14]. For example, Samuelsson *et al.* [49] reported that $R_{\mathrm{HiPIMS}}/R_{\mathrm{DC}} \sim 0.30$ for a Ti target, while $R_{\mathrm{HiPIMS}}/R_{\mathrm{DC}} \sim 0.70-0.85$ for Ag, Ta and Pa targets. Apart from the choice of target material, losing the sputtered species (metal ions) is the main cause for low deposition rates during the HiPIMS process. In HiPIMS discharges, low energy metal ions can return back to the target due to the extension of the plasma presheath adjacent to the target. As a result, only some energetic ions can overcome the potential barrier and arrive at the substrate. Mishra *et al.* [50] have suggested that weakening the magnetic field strength of the magnetron source can decrease the effect of the presheath barrier. Metal ions returning back to the target can further decrease the deposition rate due to the low value of the self-sputtering yield [51]. The self-sputtering precess can significantly develop as the HiPIMS pulse progresses. Therefore, the deposition rate can also decrease in a long HiPIMS pulse width [52]. During the early phase of a HiPIMS pulse, argon ions dominate the discharge i.e. there is less self-sputtering. Operating HiPIMS with a short pulse is an option to improve the deposition rate. For example, $R_{\mathrm{HiPIMS}}/R_{\mathrm{DC}}$ is about 0.70 for a 5 μs pulse width compared with 0.20 for a 20 μs pulse width [52]. Lundin *et al.* [53] proposed that some of the metal ions can flow to the side walls due to the azimuthal force, lowering the number of metal ions travelling along the discharge axis and the resultant deposition rate.

2.4.2 Plasma investigations

During the last decade, there has been extensive studies to understand the physics of HiPIMS discharges by plasma investigations. Using a variety of plasma diagnostic tools to measure the basic parameters of plasmas is one of strategy to better understand the physics of HiPIMS discharges. Some plasma investigation from the literature are summarised as follows.

The main mechanism of ionisation in HiPIMS discharge is electron-impact ionisation [54]. The properties and dynamics of electrons is thus paramount in HiPIMS discharge. The Langmuir probe is a common diagnostic tool to spatially and temporally measure the properties of electrons in HiPIMS, including the energy distribution function, the density and the temperature [55,56]. Bohlmark *et al.* showed that electron density just above the magnetron racetrack is very high up to $10^{19}\,\mathrm{m}^{-3}$, three order of magnitude higher than in DCMS ($\sim 10^{16}\,\mathrm{m}^{-3}$) [56]. During the on time of HiPIMS pulses, the temperature of electrons is relatively lower than that in DCMS [55]. Gudmundsson *et al.* explained in [55] that the electron cooling in HiPIMS is mainly due to the existence of a larger amount of sputtered metal during the discharge. Since the ionisation and excitation energy of metal is lower than the argon gas, the electrons thus lose their energy more effective in HiPIMS (metal dominated) than in DCMS (argon dominated).

HiPIMS provides not only dense electrons but also dense metal ions. Optical emission spectroscopy (OES) is one of the diagnostic tools employed to indicate the relative amount of metal ions specifies in HiPIMS. In DC [57] and pulsed-dc plasmas [58], emission lines emitted form metal species are typically dominated by transitions in neutrals species. In HiPIMS, the emission lines of metal ions can be observed with a significant intensity [57, 59].

As mentioned in the previous section, the energy of the bombarding ions at the substrate can determine the microstructure of growing films. Energy-resolved mass spectrometry is another diagnostic tool used to measure energy distribution functions and hence average energies for each ion species in HiPIMS. Numerous studies have shown that the maximum energy of metal ions observed in HiPIMS, can be higher than 50 eV [60, 61]. In contrast to DCMS the maximum energy of less than 25 eV is commonly observed [62]. The energetic population of metal ions have been found to increase when one operates HiPIMS at low pressure [63] or with high pulse energy [64].

Since the HiPIMS plasma is central to and directly correlates with film properties, the focus of this thesis is therefore on plasma investigations using a variety of diagnostic tools. Specifically, electrical plasma probes have been developed and employed to extract the relevant information on plasma properties and dynamics. The probes used in this thesis include a cylindrical Langmuir probe, a retarding field energy analyser and a gridded quartz crystal microbalance. Langmuir probe measurements can reveal

the properties of electrons. The retarding field energy analyser is used to obtain ion energy distribution function and the related parameters such as the flux and the average energy of ions. The gridded quartz crystal microbalance is employed to measure the ionised metal flux fraction arriving at a substrate. The detail of each technique is give in the next chapter.

2.5 Conclusions

In this chapter, the general concept of low-pressure non-thermal plasmas have been given. This kind of plasma is widely used in technological applications. Using ions in the plasma, atoms at a solid surface can be ejected out as a vapour known as sputtering which is a physical method to deposit thin films. Magnetron sputtering has been developed using the manipulation of magnetic and electric fields to confine electrons and hence increase deposition rate. Ion bombardment during the film growth can be implemented in unbalanced magnetron sputtering. The efficiency of the ion bombardment can be enhanced when film ions are used. HiPIMS is a recent thin film deposition technique that is able to provide large amount of films ions. HiPIMS is typically operated in a high-power, low-frequency, short-pulsed mode. Applying a peak power density of $> 0.5\,\mathrm{kWcm^{-2}}$ to the magnetron, a dense plasma and high degree of ionisation of sputtered species can be obtained. Since the plasma has strong influence on thin film production, plasma investigations using a variety of diagnostic tools is the main subject of this thesis.

Chapter 3

Plasmas diagnostics

3.1 Background

Plasma diagnostics are an important subject in plasma science and technology as it can experimentally provide internal information which is vital for understanding and optimising the diagnosed plasmas. Generally, there are two main approaches to diagnose plasmas namely non-invasive and invasive approaches. The former, non-invasive approaches, involves the observation of electromagnetic waves originated either from the plasma itself or from interaction between the plasma and external waves. Examples of non-invasive approaches are optical emission spectrometry (OES), optical absorption spectrometry (OAS), interferometry, Thomson scattering etc. Unlike those diagnostics, invasive approaches are those in which physical probes are directly immersed into the plasma. Interactions between a probe and a plasma are able to connect to the internal parameters of the plasma. Examples of invasive approaches are electric, magnetic and thermal probes as well as mass spectrometry.

Plasma diagnostics tools used in the thesis are categorised as invasive approaches, including the Langmuir probe (LP), the retarding field analyser (RFA) and the gridded quartz crystal microbalance (g-QCM). The Langmuir probe is used to measure basic properties of electrons in the plasma such as density, temperature and energy distribution functions. The retarding field analyser is employed to obtain directional ion flux, ion temperature and ion velocity distribution functions. The gridded quartz crystal microbalance is utilised to determine the fraction of metal ion flux in the total depositing flux. In this Chapter those plasma diagnostic tools, i.e. LP, RFA and g-QCM, are described. The basic principle, probe design and data analysis are given for each diagnostic tools. Since HiPIMS plasmas are pulsed plasmas, it is necessary to apply the time-resolved technique in order to investigate time-dependent plasma parameters during and after a pulse. The detail for time-resolved technique is also included in this chapter.

3.2 Langmuir probe

3.2.1 Principle

One of the most straightforward technique to extract fundamental plasma parameters is the use of an electrical probe known as a Langmuir probe. Basically, a Langmuir probe is an electrode immersed in a plasma as presented in figure 3.1(a). Since the plasma is an electrical conductor having free electrons and ions as charge carriers, biasing the probe with an external potential source essentially causes a flow of those charge carriers (i.e. electric currents) through the probe. The probe current as a function of the bias voltage, often referred to as the I-V characteristic, is a result of probe-plasma interactions and can inform on some internal parameters of the diagnosed plasmas.

A typical I-V characteristic of a Langmuir probe is shown in figure 3.1(b). The vertical axis represents the probe current (I_p) while the horizontal axis represents the bias voltage (V_b) driven by an adjustable voltage source. Since there are two kinds of charge carriers in the plasma, I_p is thus the summation of electron current (I_e) and ion current (I_i) drawn from the plasma. It is common to assign the I_p to be positive when $I_\mathrm{e} > I_\mathrm{i}$ and vice versa.

Using a range of the bias voltage (V_b) with respect to the plasma potential (Φ), the probe characteristic can be generally divided into three regions: the electron saturation when $V_\mathrm{b} \gg \Phi$, the electron retardation when $V_\mathrm{b} < \Phi$ and the ion saturation when $V_\mathrm{b} \ll \Phi$. Note that a plasma potential is a potential of the plasma bulk, where n_e

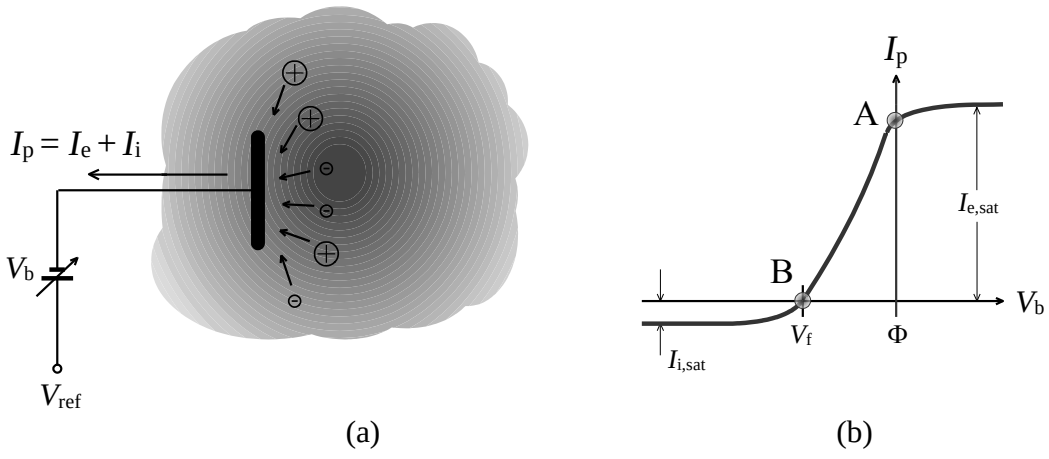

Figure 3.1: (a) A diagram presenting an electrical probe immersed in a plasma. Internal plasma parameters (e.g. n_e, T_e and EEDFs) can be deduced from the relationship between probe currents (I_p) and probe voltages (V_b) as so-called probe characteristics. Note that I_p is the summation of electron current (I_e) and ion current (I_i) drawn from the plasma. (b) A sketch of the probe characteristic presenting a curve of I_p as a function of V_b. Point A on the curve presents the character when V_b is equal to the plasma potential (Φ), while the point B shows the character when V_b is equal to the floating potential (V_f) and $I_\mathrm{p} = 0$, i.e. $I_\mathrm{e} = I_\mathrm{i}$.

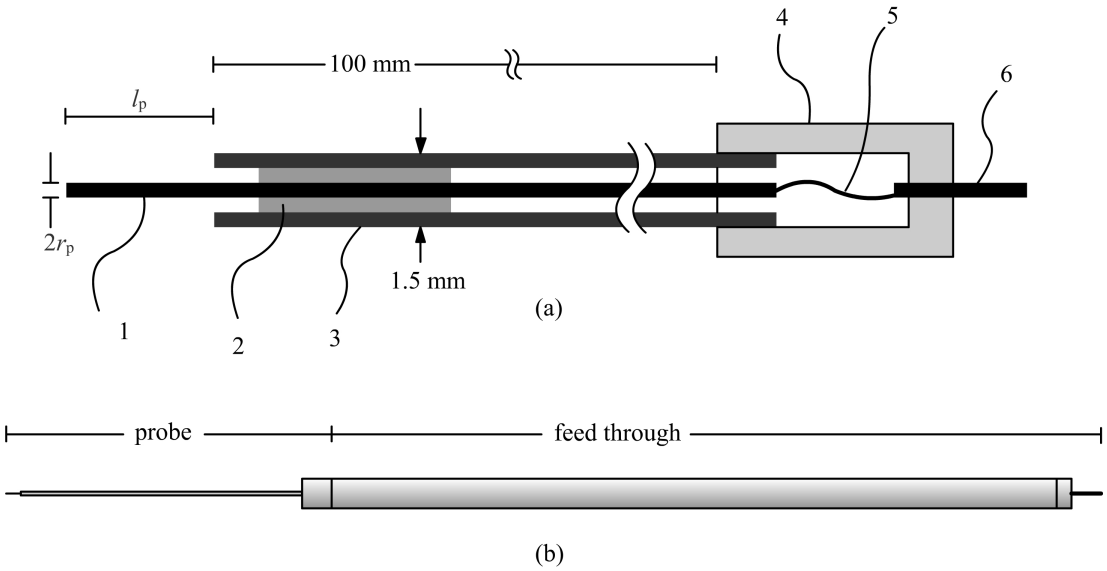

Figure 3.2: (a) A schematic diagram of the Langmuir probe consists of 1) tungsten wire, 2) inner ceramic tube, 3) outer ceramic tube, 4) probe support, 5) copper wire and 6) connector. (b) A sketch of the probe attached to a stainless-steel feedthrough.

$= n_i$, with respect to the grounded walls. When V_b is much higher than Φ, ions are repelled from the probe due to a large positive potential at the probe while electrons are attracted to the probe. In the electron saturation region, the probe current is ideally constant at a level of $I_{e,sat}$ which is then related to the electron flux (Γ_e) arriving at the probe. If the V_b is less than the Φ, electrons are partially repelled back to the plasma. The probe current decreases from $I_{e,sat}$ to $I_p = 0$, i.e. $I_e = I_i$, at the floating potential (V_f). In other word the floating potential V_f may be defined as the probe potential at which the electron flux to the probe is identical with the ion flux. The function of the probe current in the electron retarding region can yield the electron temperature (T_e) as well as electron energy distribution functions (EEDFs). When V_b is much less than Φ, in the ion saturation region, the negative potential at the probe almost stops the electrons from the plasma allowing only ions to flow to the probe. The probe current as a function of V_b in the ion saturation region depends on geometry of the probe and the theory used to describe the ion motion and collection [65].

3.2.2 Probe design

In practice, Langmuir probes can take a number of different shapes, for example a flat disk, cylinder or sphere. The current-voltage probe characteristic from different shaped probes will vary due to the way ions and electrons are collected. For example, the charged particles can travel in straight lines to a disk probe, but describe orbits in the vicinity of cylindrical or spherical probes. In this thesis, a cylindrical Langmuir probe was used since it is convenient to construct and modify. Using an appropriate model for charged particle collection in collisionless conditions, the ion and electron density can

be determined directly from the saturation regions of the I-V characteristic without the knowledge of electron temperature.

Figure 3.2(a) is a schematic diagram of a cylindrical Langmuir probe consisting of (1) a tungsten wire, (2) an inner ceramic tube, (3) an outer ceramic tube, (4) a probe support, (5) a copper wire and (6) a connector. The tungsten wire has a radius (r_p) of 0.05 mm with a protruding length (l_p) between 3 mm and 6 mm from the end of the outer ceramic tube. The wire forming this tip was held in place by an inner ceramic tube situated in the outer ceramic tube so forming a re-entrant structure. The re-entrant structure of probe tip reduced problems of deposition flux short-circuiting the probe current to ground through the surface of the outer ceramic tube. The outer ceramic tube had a radius of 1.5 mm and a length of 100 mm, and was attached to the front of probe support. In addition, the tungsten wire was connected to the connector, located at the back of the support, using a copper wire. The probe in figure 3.2(a) was attached to a stainless-steel feedthrough ($\sim$1 m long) as sketched in figure 3.2(b).

To be able to assume collision-less sheath conditions and therefore a simple probe analysis, the probe radius and the Debye screening length, $\lambda_\mathrm{De} = (\epsilon_0 T_\mathrm{e}/e n_\mathrm{e})^{1/2}$, should be less than both the electron-neutral λ_en and ion-neutral λ_in mean-free-paths [66, 67]. In HiPIMS discharges, with plasma densities varying typically between 10^9 to $10^{12}\,\mathrm{cm}^{-3}$, one calculates that λ_De $\sim$0.010 – 0.19 mm, λ_en $\sim$20 – 117 mm, λ_in $\sim$9 – 27 mm for electron energies typically between 5 and 100 eV and therefore the conditions $\lambda_\mathrm{en}/\lambda_\mathrm{De}$, $\lambda_\mathrm{in}/\lambda_\mathrm{De} > 1$ are satisfied.

3.2.3 Data analysis

Using information from the probe characteristic, basic plasma parameters including the floating potential (V_f), the plasma potential (Φ), the ion density (n_i), the electron density (n_e), the electron temperature (T_e) and the electron energy distribution functions (EEDFs) can be extracted as detailed in the following:

Floating potential V_f: Floating potential can be defined as a bias voltage at which electron current and ion current drawn to the probe are identical. In other words, V_f is the bias voltage at which the probe current is zero at the crossing point on the x-axis. For unusual probe characteristics in which there is no the crossing point in the range of V_b, floating potentials may be obtained using the probe biasing technique as shown in figure 3.3. The circuit consisted of a capacitor (C) connected to a resistor (R). A voltmeter (VM) was used to read the floating potential for the time, t, at which the voltage across the resistor is zero. The voltage across the resistor was measured by an oscilloscope. The capacitor was charged by an external DC power supply before was connected to the probe.

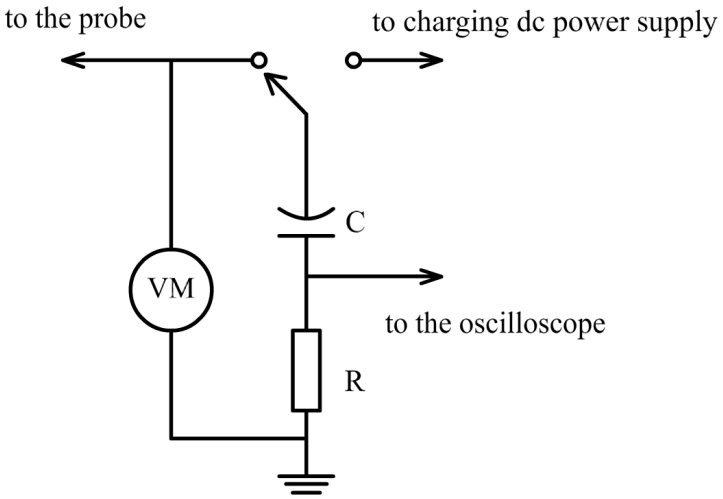

Figure 3.3: A diagram of the probe biasing technique to obtain floating potentials.

Plasma potential Φ: It is possible to use the voltage at the crossing point of extrapolated line from electron retarding and electron saturation regions as the plasma potential. However, a more reliable approach to determine the plasma potential is from the bias voltage at which the second derivative of the I-V probe characteristic $\left(\mathrm{d}^2 I_\mathrm{p}/\mathrm{d}V_\mathrm{b}^2\right)$ is zero.

Ion density: The Orbital Motion Limited theory (OML) is used to interpret ion current and ion density. For OML theory to be valid, the sheath surrounding the probe should be collision-less, which is generally valid for the condition $\xi = (r_\mathrm{p}/\lambda_\mathrm{De}) < 1$ [66]. However, the OML theory has been found to hold very well even when the sheath dimensions become smaller that the probe radius [67]. In our case where $0.2 < \xi < 5.6$, the OML theory is still valid according to [67]. Using the formulation in [66,67] the ion current $I_\mathrm{i,OML}$ (in the ion attracting region of the characteristic) follows the equation

$$I_\mathrm{i,OML} \approx \frac{\sqrt{2}}{\pi} e A_\mathrm{p} n_\mathrm{i,OML} \sqrt{\frac{e(\Phi - V_\mathrm{b})}{M_\mathrm{i}}}, \tag{3.1}$$

where e is the electron charge and M_i the ion mass, and A_p $(= 2\pi r_\mathrm{p} l_\mathrm{p})$ is the probe area. Taking the square of the equation 3.1, we get

$$\left(I_\mathrm{i,OML}\right)^2 \approx \frac{eK}{M_\mathrm{i}}\Phi - \frac{eK}{M_\mathrm{i}} V_\mathrm{b}, \tag{3.2}$$

and

$$K = \left(2\sqrt{2} e r_\mathrm{p} l_\mathrm{p} n_\mathrm{i,OML}\right)^2 \tag{3.3}$$

From equation 3.2 we can see that the square of the probe current $(I_\mathrm{i,OML}^2)$ is a linear function with bias voltage V_b. It implies that the I_p^2-V_b plots in the ion saturation

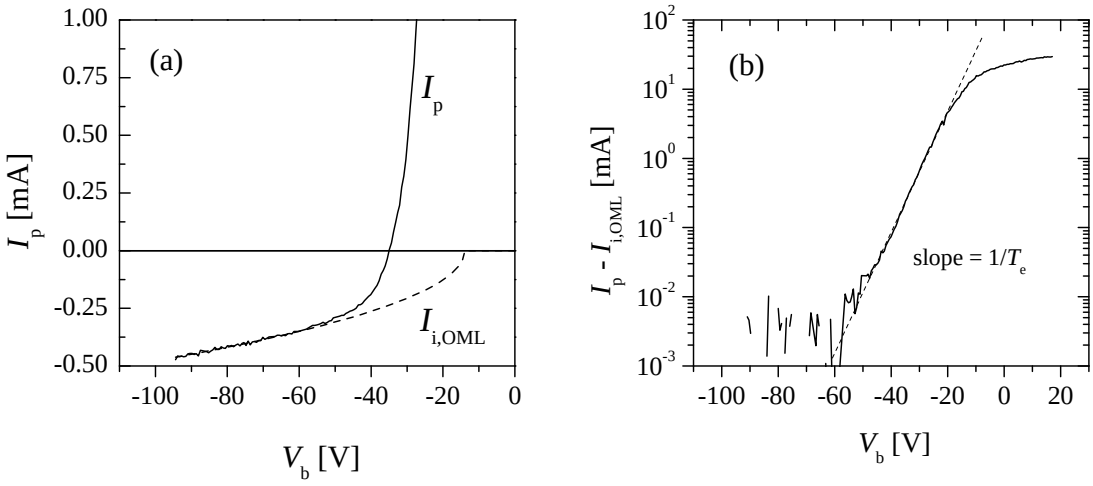

Figure 3.4: (a) An I-V characteristic of the Langmuir probe with a determined $I_{\mathrm{i,OML}}$. (b) The logarithm of the electron current after subtraction of $I_{\mathrm{i,OML}}$ from the total current. The Maxwellian electron temperature can be found from the inverse of the linear part when $V_{\mathrm{b}} < \Phi$

region can yield a linear portion with a negative slope of X with a magnitude of eK/M_{i}. Once the slope X has been obtained from the plot of I_{p}^2-V_{b}, the ion density $n_{\mathrm{i,OML}}$ is then given by

$$n_{\mathrm{i,OML}} \approx \sqrt{\frac{XM_{\mathrm{i}}}{2e}} \left(\frac{1}{2er_{\mathrm{p}}l_{\mathrm{p}}} \right). \tag{3.4}$$

Electron density: To determine the electron densities, three different analysis methods were used. Firstly, the analysis of probe current in the electron and ion saturation regions, $n_{\mathrm{e,OML}}$ and $n_{\mathrm{i,OML}}$ can be determined using the OML theory. Secondly, using the electron current at the plasma potential together with the electron temperature, the electron density ($n_{\mathrm{e,sat}}$) can also be calculated. This calculation approach is useful especially when there is the presence of multiple electron groups in the plasma. Their respective temperatures can be found from the electron-retarding region of the probe characteristic and used to determine the different group population densities. Thirdly, electron density can be determined from the electron energy distribution function $g_{\mathrm{e}}(\varepsilon)$. The electron density calculated from EEDFs is denoted as $n_{\mathrm{e,EDF}}$. A comparison of the electron densities derived from those three methods ($n_{\mathrm{e,OML}}$, $n_{\mathrm{e,sat}}$, $n_{\mathrm{e,EDF}}$) gives a general picture of the validity of the probe methods.

Electron temperature: In each probe characteristic the ion current component estimated from the OML theory needs to be subtracted from the total current I_{p} to obtain the electron component I_{e}, as demonstrated in figure 3.4(a). Using I_{e} the temperature T_{e} of Maxwellian electrons can be derived from the inverse gradient of a semi-logarithm plot of I_{e} versus V_{b} [4] as shown in figure 3.4(b).

EEDF: To determine the dynamics of the electron energy distribution functions (EEDFs), the Druyvesteyn formulation was employed. The EEDF is given by

$$g_{\mathrm{e}}(V) \approx \sqrt{\frac{2eV}{m_e}} \cdot \frac{2m_{\mathrm{e}}}{e^2 A_{\mathrm{p}}} \cdot \frac{\mathrm{d}^2 I_{\mathrm{e}}}{\mathrm{d}V^2}, \tag{3.5}$$

where $V = \Phi - V_{\mathrm{p}}$ is the voltage equivalent to the electron energy ε. It is worth noting that the Savitzky-Golay method was used to smooth the electron current [68] with 15 data points in smoothing window and a polynomial order of two. The chosen smoothing window does not change significantly the form of the EEDFs in terms of the position of the most probable energy and the width of the distribution. The electron density can then be estimated from

$$n_{\mathrm{e,EEDF}} = \int_0^\infty g_e(\varepsilon)\ \mathrm{d}(\varepsilon). \tag{3.6}$$

The effective electron temperature T_{eff} can be found from this method via

$$T_{\mathrm{eff}} = \frac{2}{3n_{\mathrm{e,EEDF}}} \int_0^\infty \varepsilon g_e(\varepsilon)\ \mathrm{d}(\varepsilon). \tag{3.7}$$

3.2.4 I-V Acquisition system

To obtain an I-V characteristic of the Langmuir probe, a varying voltage from $V_{\mathrm{b}} \gg \Phi$ to $V_{\mathrm{b}} \ll \Phi$ is need, accompanied with a measure of the probe current for each probe voltage value; establishing an I-V curve for a given condition. In addition, an ability to obtain the I-V curve for a specific time is vital to investigate the plasma parameters in pulsed discharges.

In the thesis, an automated acquisition system having 16 bit A-to-D resolution was used to acquire the probe data. The acquisition system (SmartProbe from Scientific System Ltd) has ability to bias the probe voltages from -95 to $+95$ V with a minimum voltage step of 25 mV. The maximum obtainable probe currents were 250 mA with a resolution of 0.1 μA. The typical measured noise level in the current signal was $\sim 0.5\,\mu$A, with a maximum signal-to-noise ratio of less than 8%. However, a measured current of lower than 1 μA is not acceptable for probe measurements.

To acquire an I-V curve for a specific of time during the discharge, a time-resolved mode was used with an optimum time-resolution of 0.5 μs. In this mode, the equipment was triggered from a TTL pulse tapped off from the discharge voltage signal using a $\times 100$ voltage probe (Textronix P5100) in conjunction with a time delay generator (DG535 Stanford Research Systems). Each probe voltage V_{b} and current I_{p} data point in the probe characteristic was obtained at the rising edge of the triggering pulse. The initial time $t = 0\,\mu$s is defined as the time when the discharge voltage lifts off from its initial value. In each full probe characteristic 200 data points (V_{b}, I_{p}) were collected for each required time in the discharge pulse cycle. The recorded Langmuir probe data

was obtained from the average of three complete sweeps across the bias voltage range, and no smoothing of the characteristics was performed, except in the derivation of the electron energy distribution functions.

3.3 Retarding field analyser

3.3.1 Principle

A retarding field analyser (RFA) is a plasma diagnostic tool used to measure the velocity or energy distribution functions of charge particles in a sampling plasma. The RFA is essentially a planar probe in which electrons (or ions) are removed from the fluxes of charge particles travelling perpendicularly toward the probe allowing only ions (or electrons) to be collected. Using a retarding potential wall, the kinetic energy of the collected particles can be determined. Consequently, velocity or energy distribution functions of the collected particles can then be obtained.

In technological plasmas, the RFA has been extensively employed to determine the velocity distribution functions of the ions bombarding a grounded or biased substrate immersed in DC [69], RF [70–75] and pulsed plasmas [76,77] for depositing and etching applications.

The principle of the RFA, used to measure ion velocity distribution functions (IVDFs), is based on the use of electrostatic fields from a number of electrically biased grids for electron repulsion and for ion energy discrimination (energy selection). Ions with a selected energy range are then collected at a collector electrode. Ion current at the collector as a function of the discriminating voltage establishes an I-V characteristic of the RFA. The ion velocity distribution function (IVDF) is proportional to the first derivative of the I-V characteristic of the RFA.

3.3.2 Modes of operation

The RFA can typically be operated in a filter mode and a normal mode. In the filter mode, the discriminating voltage is applied on one of the grids (ion discriminator), while ion current is measured at the collector located behind the grids [71, 74, 78]. Depending on the number of the grids used, the RFA operated in the filter mode can have different configurations as shown in figure 3.5. In a two-gridded configuration, in figure 3.5(a), the electrons from the sampling plasma are repelled by the negative voltage V_r at the repelling grid (R), while the sampled ions are discriminated by the positive potential V_d biased at the ion discriminator grid (D). The ions with a kinetic energy of less than $e(\Phi - V_\mathrm{d})$ are filtered out from the contribution in current at the negatively biased collector (C). Ions bombarding the collector can cause the secondary electron emission at the collector resulting in an excessive current reading. To solve this problem, an additional electron suppressor can be used in a three-gridded configuration

shown in figure 3.5(b). In this configuration, the voltage at the collector is slightly higher than that at the electron suppression grid (S). The secondary electrons created at the collector with energy of less than $e(V_c - V_s)$ can thus return back to the collector obtaining the corrected ion current. Since the first grid of the two-gridded and the three gridded configurations are biased to the negative voltage V_r, the measured IVDFs thus correspond to the distribution function of ions bombarding to a biased substrate. The additional grounded grid (G) can be added as a sampling grid for IVDFs of ions bombarding to a grounded substrate as shown in figure 3.5(c).

Unlike the filter mode, the discriminating voltage is applied directly to the collector when the RFA is in the normal mode of operation [70, 73, 79]. The diagram of a two-gridded RFA, similar in design to that used by Ingram and Braithwaite [70] is shown in figure 3.6(a). The RFA consists of a sampling grid (G), an electron repelling grid (R) and an ion collector (C). The sampling grid G is electrically grounded corresponding to a grounded substrate. The grid R is biased with a negative voltage (V_r) in order to repel electrons having energy less than $e(\Phi - V_r)$. The collector C is directly biased by a discriminating voltage (V_d). The ions with kinetic energy greater than $e(\Phi - V_d)$ are then collected and have a contribution in current I_c measured at the collector.

Obviously, operating the RFA in the normal mode is basically similar to traditional planar-type Langmuir probe measurements. It means that an acquisition system used to obtain the I-V characteristics of a Langmuir probe is compatible to obtain that of the RFA. Moreover, with the probe acquisition system as described in the previous section, IVDF for a particular time during a HiPIMS pulse can thus be measured. The RFA used in this thesis is therefore operated in the normal mode accordingly.

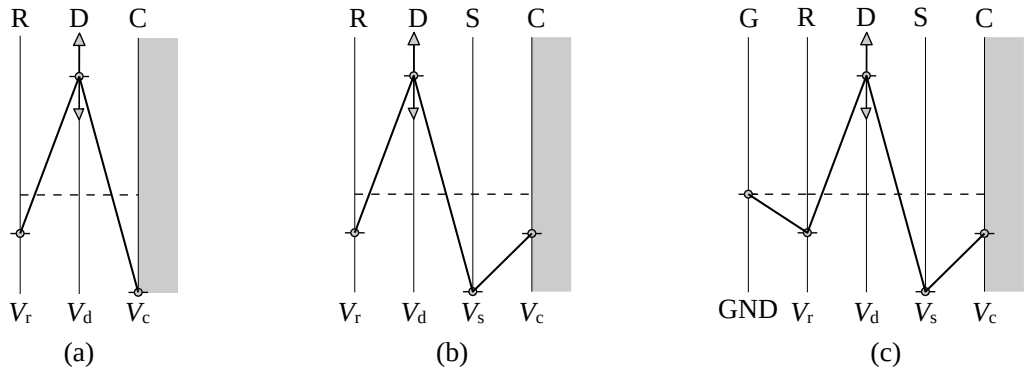

Figure 3.5: Diagram of voltage distribution inside the RFA operated in the filter mode with (a) two-gridded, (b) three-gridded and (c) four-gridded configurations. The sampled ions enter to the RFA at the grid R and terminate at the collector C. The letter R denotes for the electron repelling grid, D the ion discrimination grid, C the ion collector, S electron suppressor grid, G grounded sampling grid. Voltage applied to the grid R, D, S and the collector C is denoted by V_r, V_d, V_s and V_c while the system ground (GND) is applied to the sampling grid G.

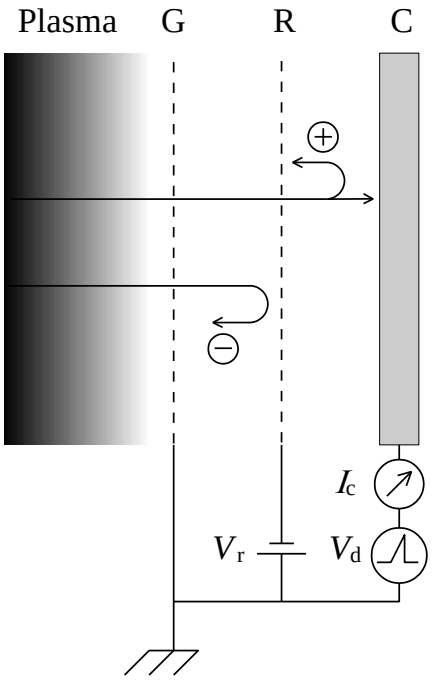

Figure 3.6: A schematic diagram of the two-gridded retarding field analyser (RFA) arranged for the normal mode of operation as proposed in [70]. The RFA, immersed in a plasma having a local potential Φ, includes a sampling grid (G), a repelling grid (R) and a collector (C). The outermost grid G is electrically grounded corresponding to a grounded substrate. The grid R is biased to a negative voltage V_r to repel electrons with energy of less than eV_r back to the grid G. The collector C is connected to an I-V acquisition system at which a range of discriminating voltages V_d is scanned and the ion current I_c is measured. Only ions with kinetic energy greater than eV_d can be collected and have a contribution in the I_c measured at the collector.

3.3.3 The probe requirements

For the IVDF of ions entering the analyser not be changed on their transit through the instrument two requirements for the RFA should be satisfied as suggested by in [70,71]. Firstly, the hole size of the outermost grid or the grid G has to be small enough to prevent the penetration of the plasma into the RFA. Secondly, the total distance between the grid G and the ion collector C need to be less than the mean free path for the collision events that may alter the IVDFs. The details of these two requirements are summarised as follows.

Basically, a plasma sheath with a planar structure having a thickness of l_{sh} is formed in adjacent to a planar substrate immersed in a quasi-neutral plasma. In the case of a planar grid-type substrate as the sampling grid of the RFA, however, the plasma tends to penetrate into the grid if the space between the grid bars is larger than the critical value of $2l_{sh}$. This results in the collapse of the planar structure of the plasma sheath as depicted in figure 3.7. Although l_{sh} is typically a few electron Debye length λ_{De}, the suggested value of $2\lambda_{De}$ for the space between the grid is not only to prevent the plasma penetration [71] but also to sustain a well-defined planar sheath structure.

In HiPIMS, plasma density and electron temperature at a typical substrate position (5 – 10 cm from a magnetron) is in the order of $1 \times 10^{12}\,\mathrm{cm}^{-3}$ and 3 eV resulting in λ_{De} $\sim 13\,\mu$m. The hole size of a grid used for the sampling grid should thus be less than $\sim 26\,\mu$m for those plasma conditions.

The second requirement is associated with collision events inside the RFA. One of these events is the resonant charge exchange collisions in which an ion of one element can capture electrons from a neutral of the same element as the reaction of

$$\mathrm{Ar}^{+}_{\mathrm{fast}} + \mathrm{Ar}_{\mathrm{slow}} \rightarrow \mathrm{Ar}_{\mathrm{fast}} + \mathrm{Ar}^{+}_{\mathrm{slow}}$$

and

$$\mathrm{Ti}^{+}_{\mathrm{fast}} + \mathrm{Ti}_{\mathrm{slow}} \rightarrow \mathrm{Ti}_{\mathrm{fast}} + \mathrm{Ti}^{+}_{\mathrm{slow}}.$$

for argon and titanium, respectively. In these type of collisions, the fast ions along the way to the collector may change to be fast neutral and not contribute in the collector current. Therefore, total distance between the gird G and the collector C need to be less than the mean free path of those resonant charge exchange collisions.

The mean free path of the charge exchange collisions (λ_{iex}) can be obtained from the equation of

$$\lambda_{\mathrm{iex}} = \frac{1}{n_{\mathrm{n}}\sigma_{\mathrm{iex}}},$$

where n_{n} is neutral density of an element and σ_{iex} is cross section of the charge exchange collisions between ions and neutrals of the same element. For argon and titanium ions at an energy of 0.1 eV, the cross section σ_{iex} is 72×10^{-20} and $220 \times 10^{-20}\,\mathrm{m}^2$, respectively [80]. The neutral density of argon is $\sim 3.3 \times 10^{19}\,\mathrm{m}^{-3}$ at an operating pressure of 0.133 Pa (1 mTorr). The λ_{iex} for argon and titanium is thus ~ 42.1 and 13.8 mm, respectively. Therefore, the distance between the sampling gird and the collector of the RFA should be less than 13.8 mm for those process conditions.

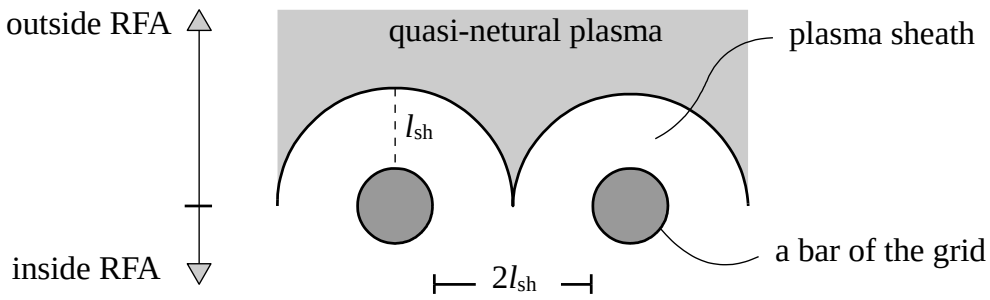

Figure 3.7: A diagram showing a critical hole size of a sampling grid to prevent the plasma penetration into the RFA. The plasma with a sheath thickness of l_{sh}, a few electron Debye length λ_{De}, cannot invade into the RFA if the space between bars or the hole size of the sampling grid is less than $2l_{\mathrm{sh}}$. However, in order to sustain a well-defined planar structure of the plasma sheath, the hole size should be less than $2\lambda_{\mathrm{De}}$. This condition is one of the crucial requirements for the RFA designing as suggested in [70, 71].

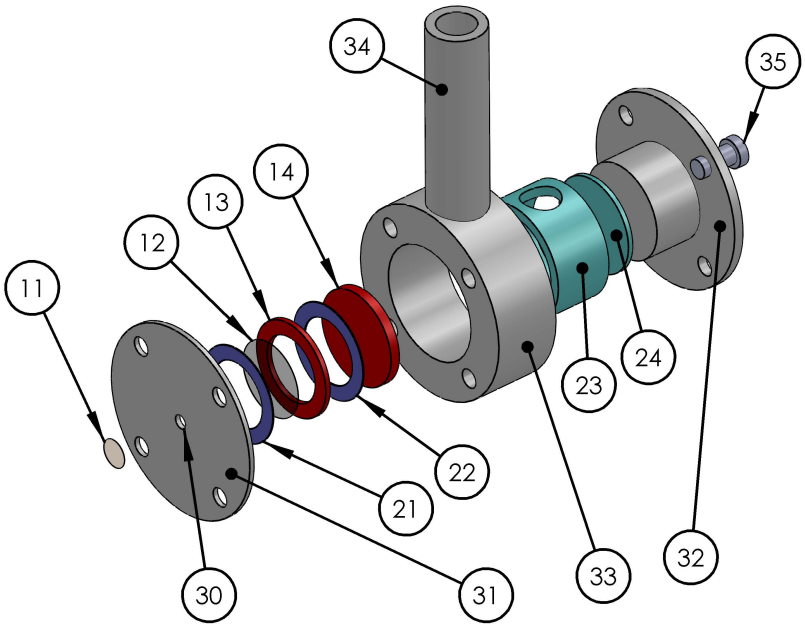

Figure 3.8: A layout presenting components of the two-gridded RFA.

3.3.4 Probe design

The RFA assembled in the present work consists of a number of components which were stacked together in a disk-like housing as presenting in figure 3.8. The detail of the RFA assembling and components are given as follows.

The RFA housing composes of three pieces of stainless steel namely a body (33) with an extruded tube (34), a front cap (31) with a 1.5 mm aperture (30) and an end cap (32). A sampling grid (11) is concentrically placed on top of the front cap (31). The front (31) and end cap (32) can firmly compress all components inside the RFA using four M2 screws (35) for each cap. The machinable insulators (23) and (24) are used to align and to electrically isolate electrodes inside the RFA from the housing. The essential components inside the RFA include insulator-washers (21) and (22), an electron repelling grid (12) on a metal-washer (13) and an ion collector (14). Two electric wires (not shown) inserted along the extruded tube (34) are soldered with the metal-washer (13) and the ion collector (14) allowing to apply the electron repelling voltage V_r and the ion discriminating voltage V_d to those electrodes, respectively.

As stated in the previous section, there are two crucial requirements in designing of the RFA. Firstly, the hole size of the sampling grid (11) has to be less than $2\lambda_\mathrm{De}$, which is 26 μm for a plasma with $n_\mathrm{e} \sim 1 \times 10^{12}\,\mathrm{cm}^{-3}$ and $T_\mathrm{e} \sim 3\,\mathrm{eV}$. To satisfy this requirement, ultrafine grid with a hole size of $7.5 \pm 3\,\mu$m was utilised as the sampling grid (11) of the RFA. The grid, typically used for transmission electron microscopy applications, is made of nickel and 3.05 mm in diameter, $35 \pm 5\,\mu$m in thickness and 36% optical transparency. This delicate grid can be adhered to the front cap (31) by

the use of silver conductive paint. Another requirement in the RFA design is that the total distance between the sampling grid (11) and the ion collector (14) need to be less than 13.8 mm (λ_{iex} of titanium at 0.13 Pa). However, the RFA is designed to have a short total distance of 1.55 ± 0.02 mm which is the summation of the thickness of the front cap (0.75 ± 0.02 mm), the repelling grid (0.09 ± 0.02 mm), two insulator-washers ($2 \times 0.13 \pm 0.02$ mm) and the metal-washer (0.45 ± 0.02 mm). With this total distance, the RFA is able to employ in plasmas operated at a maximum pressure of 1.18 Pa.

Since there are no critical requirements for the electron repelling grid (12), a rather strong mesh, made of stainless steel with a hole size of 0.14 mm and a transparency of 51%, was used for the grid (12). The mesh is placed on the metal-washer (13) and is tolerant enough to be compressed in the RFA.

The assembled RFA is mounted on a grounded feedthrough with the same axis of the extruded tube (34). With this configuration, the RFA is thus able to be translated along and rotated around the feedthrough axis. The translation and rotation of the RFA facilitate spatial-resolved and angular-resolved IVDF measurements. The feedthrough has two vacuum-shielded electrodes. Inside the vacuum, the electrodes are connected to the electrons repelling grid and ion collector. Outside the vacuum, the electrode for the grid R is biased with a negative voltage V_{r} from an external dc power supply. The collector electrode is connected directly to the automated commercial data acquisition system where the discriminating voltage V_{d} is applied and the ion current I_{c} is measured, as shown in figure 3.6. A data set of (V_{d}, I_{c}) establishes an I-V characteristic of the RFA for specific plasma conditions in which an IVDF and other information of the sampling ions can be obtained.

3.3.5 Data analysis

A sketch of a typical collector current I_{c} as a function of discriminating voltage V_{d} or an I-V curve of the RFA is shown in figure 3.9. The I-V curve can be separated into two regions namely an ion saturation region and an ion retarding region. In the ion saturation region, all ions, in the ion velocity distribution function (IVDF), are collected at the collector resulting in a constant value which is referred to as an ion saturation current $I_{\text{i,sat}}$. In ion retarding region, only ions with kinetic energy greater than potential energy of $e(\Phi - V_{\text{d}})$ are able to reach the collector and contribute in the collector current. The I_{c} in this region thus gradually decreases associated with the distribution of ion velocities. A function of the velocity distribution $f_{\text{i}}(v)$ for singly charged ions can be obtained from the I-V curve by taking the first derivative of the collector current I_{c} with respect to the discriminating voltage V_{d} [71, 79] (see Appendix A.3):

$$f_{\text{i}}(v) = -\frac{M_{\text{i}}}{\chi e^2 A}\frac{\mathrm{d}I_{\text{c}}}{\mathrm{d}V_{\text{d}}}, \tag{3.8}$$

where χ is the total transparency of the grids used (18%). A is the area of the aperture of the sampling grid ($1.8 \times 10^{-6}\,\mathrm{m}^2$), M_i is the ion mass (7.9×10^{-26} kg for an titanium ion, 6.6×10^{-26} kg for an argon ion) and e is the elementary charge (1.6×10^{-19} C).

To obtain an IVDF curve, $f_\mathrm{i}(v)$ from equation 3.8 was suggested by Allen [81] to be plotted against the ion velocity (v) which is related to the discriminating voltage V_d as

$$v = \sqrt{\frac{2eV_\mathrm{d}}{M_\mathrm{i}}}. \tag{3.9}$$

The other fundamental information of the sampled ions can then be extracted from $f_\mathrm{i}(v)$ including the density n_i, most probable velocity, $v_\mathrm{i,most}$, mean velocity $\langle v_\mathrm{i} \rangle$, mean square velocity $\langle v_\mathrm{i}^2 \rangle$, flux Γ_i, energy E_i, and energy density Ψ_i from the following expressions [82]:

$$n_\mathrm{i} = \int_0^\infty f_\mathrm{i}(v)\,\mathrm{d}v, \tag{3.10}$$

$$\langle v_\mathrm{i} \rangle = \frac{1}{n_\mathrm{i}} \int_0^\infty v f_\mathrm{i}(v)\,\mathrm{d}v \tag{3.11}$$

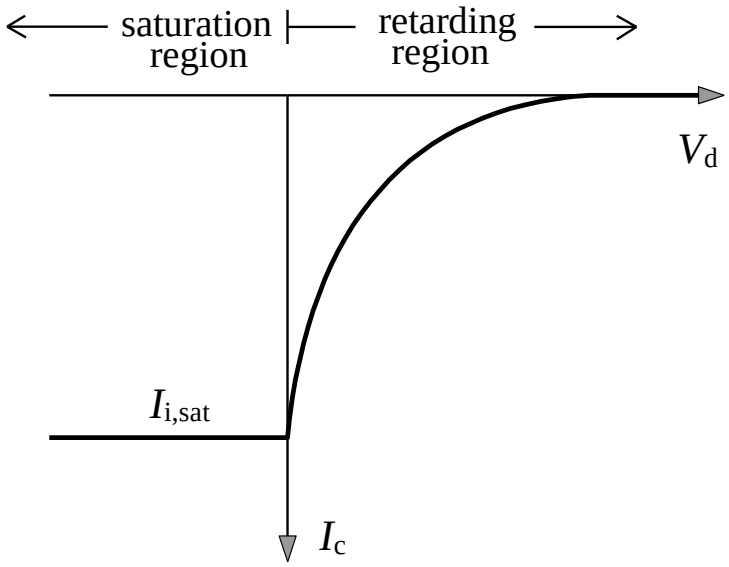

Figure 3.9: A simple sketch of an I-V characteristic of the RFA. The x-axis is the discriminating voltage V_d biased to the ion collector. The y-axis presents ion current I_c measured at the collector. Note that the I_c is assigned to be negative value for current carried by ions. Typically, there are two region in an I-V curve: ion saturation and ion retarding region. The ion current is constant in the ion saturation region, while it gradually decrease in the retarding region. The IVDFs of the sampled ions is then obtained from the I-V curve by taking the first derivative of I_c with respect to V_d.

$$\left\langle v_{\mathrm{i}}^2 \right\rangle = \frac{1}{n_{\mathrm{i}}} \int_0^\infty v^2 f_{\mathrm{i}}(v)\,\mathrm{d}v \tag{3.12}$$

$$\Gamma_{\mathrm{i}} = \langle v_{\mathrm{i}} \rangle\, n_{\mathrm{i}} \tag{3.13}$$

$$E_{\mathrm{i}} = \frac{1}{2} M_{\mathrm{i}} \left\langle v_{\mathrm{i}}^2 \right\rangle \tag{3.14}$$

$$\Psi_{\mathrm{i}} = \frac{1}{2} M_{\mathrm{i}} \left\langle v_{\mathrm{i}}^2 \right\rangle n_{\mathrm{i}} \tag{3.15}$$

The ion energy distribution functions (IEDF) assigned as $f_{\mathrm{i}}(\varepsilon)$ were calculated from ion velocity distribution function $f_{\mathrm{i}}(v)$ using the well-known expression:

$$f_i(\varepsilon) = \frac{1}{\sqrt{2M_{\mathrm{i}}\varepsilon}} f_{\mathrm{i}}(v), \tag{3.16}$$

where ε $(= eV_{\mathrm{d}})$ is the kinetic energy of singly charged ions. The mean ion energy $\langle \varepsilon_{\mathrm{i}} \rangle$ can then be obtained from:

$$\langle \varepsilon_{\mathrm{i}} \rangle = \frac{1}{n_i} \int_0^\infty \varepsilon f_i(\varepsilon)\,\mathrm{d}\varepsilon \tag{3.17}$$

3.4 Gridded quartz crystal microbalance

A gridded quartz crystal microbalance (g-QCM) is essentially a combination between a quartz crystal microbalance (QCM) and biasing metal grids. The g-QCM has been used to measure ionised metal flux fraction (IMFF) in ionised physical vapour deposition (IPVD) processes [83–86]. In this section, the principle and the design of g-QCM are given.

3.4.1 Principle

A QCM is an *in situ* technique to measure the thickness of the deposited film and growth rate in real-time during a deposition process. Principally, when being excited by an external oscillator circuit, a quartz sensor, made from a piezoelectric material, can be mechanically vibrated with an resonant frequency of several megahertz. One of the parameters influencing to the resonant frequency is the total mass of the sensor. The resonant frequency tends to decrease with an increase of the total mass. In deposition processes, the total mass of the quartz is changed by films being deposited onto the quartz surface. The difference in frequency between loaded and unloaded crystal thus relates directly to the thickness of the depositing films. Consequently, the growth rate of the film can also be calculated by using the change of film thickness and the depositing time interval.

In conventional magnetron sputtering, depositing flux consists almost only sputtered atoms. The thickness and the growth rate monitored by the QCM is thus caused by the neutral flux of the sputtered particles. In HiPIMS, however, a significant amount of the sputtered particles are ionised and then have a remarkable contribution in the depositing fluxes. In order to distinguish the metal ions flux and the metal neutral flux arriving to the QCM, the approach of ion repelling by the use of a positive potential with respect to the local plasma potential has essentially been adopted. The positive biasing voltage to repel the metal ion flux may be applied to the additional metal grids placed in vicinity of the QCM [83–86] or to the QCM itself [87, 88].

Rossnagel and Hopwood [83] have originally employed two grids with a grounded QCM to measure IMFF in an IPVD process. The first grid was grounded to shield the QCM from the plasma, while the second grid was electrically biased to repel or admit ions to the QCM. When the grid biasing voltage is lower than the local plasma potential, the total deposition rate R_{t} which is the summation of metal ion deposition rate R_{i} and neutral deposition rate R_{n} can be obtained. In contrast, when biasing voltage is higher than the plasma potential, ions are repelled back allowing only neutrals to reach the QCM surface with the rate of R_{n}. The ionised metal flux fraction (IMFF) can principally be calculated from the total deposition rate R_{t} and the neutral deposition rate R_{n}.

Green *et al.* [84]and Meng *et al.* [86] have pointed out that in order to obtain a more reliable IMFF, it is necessary to determine the geometric factor (G) of the sensor in addition to the measurement of the total deposition rate R_{t} and the neutral deposition rate R_{n}. The factor G is associated with the fact that neutral deposition rate at the quartz surface is attenuated not only by the total transparency of the gird (T) used, but also by the distribution of the neutral particles and geometry of the g-QCM. If R_{N} is the actual deposition rate of neutrals at the first grid, the neutral deposition rate reading at the quartz surface R_{n} is

$$R_{\mathrm{n}} = R_{\mathrm{N}} \cdot G \cdot T. \tag{3.18}$$

Since the metal ion flux is anisotropic travelling through the plasma sheath, the deposition rate caused by the ions R_{i} at the quartz surface is reduced from the actual rate R_{I} only by the transparency T, expressed as:

$$R_{\mathrm{i}} = R_{\mathrm{I}} \cdot T. \tag{3.19}$$

If the total deposition rate measured at the quartz surface R_{t} is the summation between R_{n} and R_{i} or

$$R_{\mathrm{t}} = R_{\mathrm{i}} + R_{\mathrm{n}}, \tag{3.20}$$

the ionised metal flux fraction IMFF can be written as

$$\mathrm{IMFF} = \frac{R_{\mathrm{I}}}{R_{\mathrm{I}} + R_{\mathrm{N}}} = \frac{R_{\mathrm{t}} - R_{\mathrm{n}}}{R_{\mathrm{t}} - R_{\mathrm{n}} + (R_{\mathrm{n}}/G)}. \tag{3.21}$$

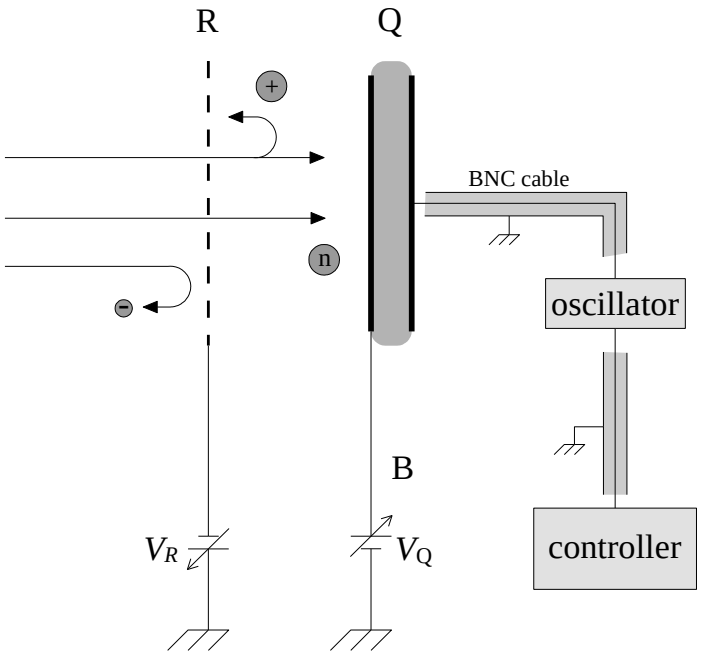

Figure 3.10: A schematic diagram of an *in situ* flux fraction analyser for metal ions. The analyser consists of an electron repelling grid (R) and a biasing quartz sensor (Q). The grid R connected to negative voltage V_R is used to reduce the perturbation of the electron. For the quartz sensor, one side of its surface, the deposited side, is biased by a V_Q while the other side is connected to the oscillator circuit via BNC cables.

It is worth noting that 3.18 to 3.21 are adopted from [86] with the assumption that the deposition rates are proportional to their depositing fluxes, e.g., $R_n \propto \Gamma_n$.

In order to repel ions and collect only neutrals, the voltage used to filter out the ions may bias directly to the quartz sensor. Using this technique, the number of grids used can be reduced [87] or even be eliminated [88] leading to a faster measuring rate (the thickness and growth rate at the quartz surface). In the present work, a g-QCM similar in design to that used by Nakamura *et al.* [87] was adopted to achieve the fastest measuring rate. The detail of the g-QCM design is given in the next section.

3.4.2 Probe design

The figure 3.10 shows a schematic diagram of an *in situ* flux fraction analyser for metal ions. The analyser is basically a modified energy analyser in which a quartz crystal microbalance is employed to be a particle collector. The analyser consists of an electron repelling grid (R) stacked over a biasing quartz sensor (Q). The grid R was made of stainless steel with a mesh number of 400 lines per inch, a wire thickness of 30 μm and optical transparency of $\sim$20%. The grid R was biased to a negative voltage V_R to effectively repel the electrons from the sampling flux. The grid R was located in an aluminium housing stacked on top of the quartz sensor, yielding a 5 mm gap between the grid and the sensor. The quartz was a gold coated piezoelectric disk with

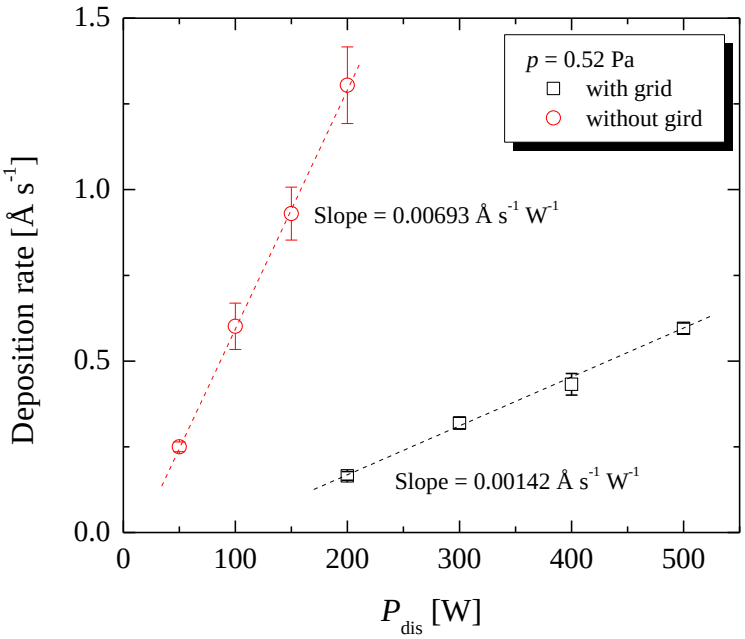

Figure 3.11: Plots of deposition rate D as a function of discharge power P_{dis} during DC magnetron sputtering at a pressure p of 0.52 Pa, with and without the grid. Using the slopes for those two cases together with the grid transparency of 28%, the geometric factor G of the analyser in the equation 3.22 was approximately 0.73.

a diameter of the exposed area of 8.2 mm, a thickness of 0.3 mm and an initial resonant frequency of 6 MHz. In a typical configuration, one side of the quartz surface (exposing side) is connected to ground while the other side was connected to the oscillator circuit (MAXTEK 400) via BNC cables. In the modified version for IMFF measurements, however, the exposed side of the sensor was connected to an external dc power supply for the bias voltage V_{Q}. When V_{Q} is lower than the local plasma potential Φ, metal ions along with the metal neutrals are able to have a contribution in the measured deposition rate or the total deposition rate R_{t}. In contrast, when $V_{\text{Q}} > \Phi$, metal ions are then removed from the depositing flux yielding the deposition rate R_{n}, the result from the metal neutral flux only.

As suggested in [84], the factor G, for a given operating pressure, can be experimentally determined by comparing the neutral deposition rate with and without the grid (R_{wg} and R_{wog}, respectively) together with the knowledge of grid transparency (T), expressed as

$$R_{\text{wg}} = R_{\text{wog}} \cdot G \cdot T \tag{3.22}$$

To determine the factor G of the analyser used in the present work, the deposition rate in DC discharges with and without the grid were plotted for a number of discharge powers, P_{dis}, at a pressure of 0.52 mTorr, as shown in figure 3.11. Using the normalized static deposition rates (the slopes of those two cases) and the grid transparency of

~ 0.20, the factor G of the g-QCM was approximately 0.73.

From the calculated value of IMFF, it is possible to determine the deposition rates of metal neutrals R_{N} and of metal ions R_{I} at the grid (the same deposition rates as would be seen at a substrate biased to the same potential as the grid R) from

$$R_{\mathrm{N}} = \frac{R_{\mathrm{n}}}{G \times T} \tag{3.23}$$

and

$$R_{\mathrm{I}} = \frac{R_{\mathrm{N}}}{(1/\mathrm{IMFF}) - 1} \tag{3.24}$$

The total deposition rate R_{T} at the grid is the summation of R_{N} and R_{I}.

3.5 Summary

In this chapter, details of the main plasma diagnostic tools employed in the thesis have been described. It includes the Langmuir probe, the retarding field analyser and the gridded quartz crystal microbalance. The cylindrical Langmuir probe was used to determine properties of electrons in plasma including density, temperature and energy distribution function. The RFA was used to determine directional ion flux and ion energy distribution functions. The RFA used in the thesis operated in the normal mode in which the process to collect the probe characteristic is the same as Langmuir probe. In this manner, an acquisition system typically used for Langmuir probe measurements is suitable to obtain RFA probe characteristics. The gridded quartz crystal microbalance has been applied to measure the ionised metal flux fraction in the HiPIMS discharge.

Chapter 4

Short and long term phenomena

4.1 Background

To optimize the plasma processes and therefore the resultant thin film properties in HiPIMS processes, a better understanding of the dynamics of the plasma is required. The understanding can take the form of basic plasma parameter measurements, particularly with adequate temporal resolution.

One relatively straightforward technique to determine the plasma parameters is the Langmuir probe. For instance, Macák *et al.* [59] used planar probe at a fixed electrical bias in the ion saturation region of the probe characteristic to infer metal ion densities up to $10^{12}\,\mathrm{cm}^{-3}$. Recently, however a more sophisticated Druyvesteyn formulation has been used to extract not only the electron densities and effective electron temperatures but also the form of electron energy distribution function (EEDF) from the probe characteristics [55, 89–92].

The structure of the HiPIMS plasma has been studied by Alami *et al.* [93] using a triple Langmuir probe with the observation of two temporally separated peaks in the electron density at a relatively high pressure of around 2.7 Pa. The first density peak seen in the on-time was assumed to be as a result of combined argon and metal ionisation with the second peak, appearing some $100\,\mu$s later (during the off time) due to the reflection of a plasma ion acoustic wave from the vessel walls. However, Vetushka and Ehiasarian [90] who also observe this second peak suggested it might be due to the slow diffusion of plasma directly from the target. Interestingly, Vetushka and Ehiasarian [90] found using a Druyvesteyn probe formulation method, the existence of two distinct groups of electrons at the early stages of the pulse on-time (i.e. at times $t < 40\,\mu$s) with 'hot' temperatures of $6-7\,$eV cooling to merge with a 'cold' distribution of temperature about 1 eV after $60\,\mu$s. Pajdarová *et al.* [91], employing a similar probe method, confirmed the presence of two electron groups at the early stages of the voltage pulse with the 'hot' group having sufficient energy to ensure that no floating potential (and no discernable ion saturation region) in the probe characteristics could be seen. Their results indicated strongly the existence of electrons with energies in the range

100 – 200 eV and the authors argue these 'hot' or 'beam-like' electrons may result from an electron avalanche phenomenon in the early stages of the voltage pulse evolution. This energetic-electron generation phenomenon is further explored in this study.

Despite the excellent Langmuir probe work carried out recently in HiPIMS discharges, many of the observations have suffered from a lack of sufficient time-resolution to distinguish clearly fast phenomena. In addition, most measurements are not made over the full discharge cycle so no full picture of the plasma evolution is revealed. In this chapter, the electron dynamics during the early stage of the pulsed discharge are investigated. In addition, the dynamics of electrons in the afterglow plasma are also investigated to observe the long-term decay characteristics of the plasma.

4.2 Experimental arrangement

4.2.1 The HiPIMS system

A schematic diagram of experiment arrangement is shown in figure 4.1. The plasma source consists of an unbalanced circular planar magnetron (supplied by GENCOA Ltd) equipped with 150 mm diameter titanium target. The maximum value of the parallel component (B_r) of magnetic field at the target was measured as $B_r = 50\,\mathrm{mT}$. The magnetron source was installed in a cylindrical vacuum chamber 40 cm in diameter and 60 cm in length. The chamber was evacuated to a base pressure of $6 \times 10^{-4}\,\mathrm{Pa}$ by a 1000 Ls^{-1} turbo-molecular pump backed by a vane rotary pump. High purity 99.995 % argon gas was introduced into the chamber via a mass flow controller at a fixed flow rate of 30 sccm. An exhaust throttle valve was used to control the working pressure at the chosen values of 0.5, 1.1 and 1.6 Pa, monitored by a Baratron pressure gauge.

The HiPIMS supply for the experiments presented this Chapter was a Sinex3 (from Chemfilt AB Ltd) operated with fixed set-point voltage amplitudes between $-650\,\mathrm{V}$ and $-850\,\mathrm{V}$ depending on the chosen peak target power density. The pulse width and frequency of the voltage pulse were a fixed at $100\,\mu\mathrm{s}$ and 100 Hz, respectively, for all experiments. Discharge voltage waveforms (V_{dis}) were monitored by $\times 100$ voltage probe (Textronix P5100), while a high-current transformer (Textronix CT4) in conjunction with a current probe (Textronix TCP202) was used to measure the discharge current waveforms (I_{dis}). Both waveforms were recorded on a four channel digital oscilloscope (Textronix TDS3014) having a 100 MHz bandwidth and transferred to a computer via an RS-232 port using an interfacing program. The peak discharge power density at the cathode (P_{dis}) used as a chosen operating parameter in this study is taken as the maximum in the calculated product of the I_{dis} and V_{dis} waveforms divided by the total cathode area $177\,\mathrm{cm}^2$.

The Langmuir probe was placed at one fixed location on the discharge centreline, 100 mm from the target. This position was 35 mm beyond the magnetic null ($B_z = 0$)

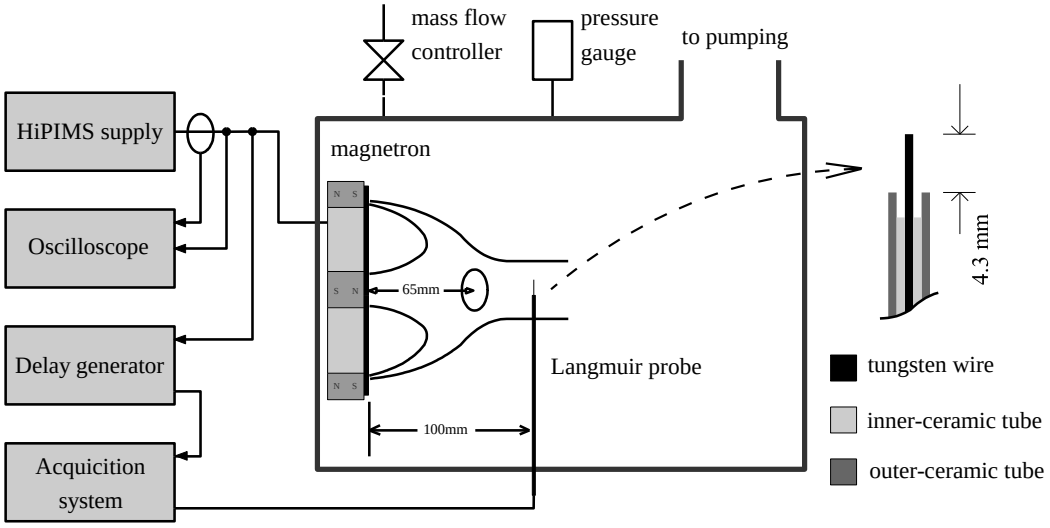

Figure 4.1: A schematic diagram of the experimental setup showing; the magnetron source, the general magnetic field configuration (including the extent of the magnetic trap region), the Langmuir probe design and its position in the discharge. The magnetic field geometry was determined from Hall probe measurements.

present on the discharge axis and shown in figure 4.1. The cylindrical probe tip was oriented with its length parallel to the target surface, as shown in figure 4.1. To ensure electron collection at the probe was not distorted by the presence of the magnetic field (i.e. the electrons do not experience a magnetic field), the probe radius r_{p} should less than the electron gyro radius r_{gy}. Using typical electron temperature of 3 eV and a measured magnetic-field strength of 1.5 mT at the probe position, r_{gy} was calculated to be $\sim 0.10 - 0.70$ mm yielding $r_{\mathrm{gy}}/r_{\mathrm{p}} > 1$. Therefore, the magnetic field has only a small perturbing effect on the collected electron current.

As described in section 3.2.4 the I-V probe characteristics were obtained from the acquisition system (the SmartProbe). Since each probe characteristic contains 200 data points, the acquisition system thus needs 200 HiPIMS pulses to plot an I-V curve representing for an acquiring time. To increase the signal-to-noise ratio, three I-V curves for the acquiring time were obtained and averaged.

The plasma parameters (electron density n_{e}, ion density n_{i}, electron temperature T_{e}, plasma potential Φ floating potential V_{f} and form of the EEDF) were determined throughout a pulse period from $t = 0.5 - 9000\,\mu$s with different time steps. For example, during the pulse beginning at $t = 0.5 - 10\,\mu$s, the time step of the measurements was $0.5\,\mu$s, while the time step was larger than $100\,\mu$s during the afterglow (i.e. $t > 100\,\mu$s). Two chosen peak power densities P_{dis} of 500 and 1000 Wcm^{-2} and three argon pressures of 0.5, 1.1, 1.6 Pa were selected as the process parameters for this study. No substrate holder was used in this study.

An important finding in this study is that during the early stages of the voltage

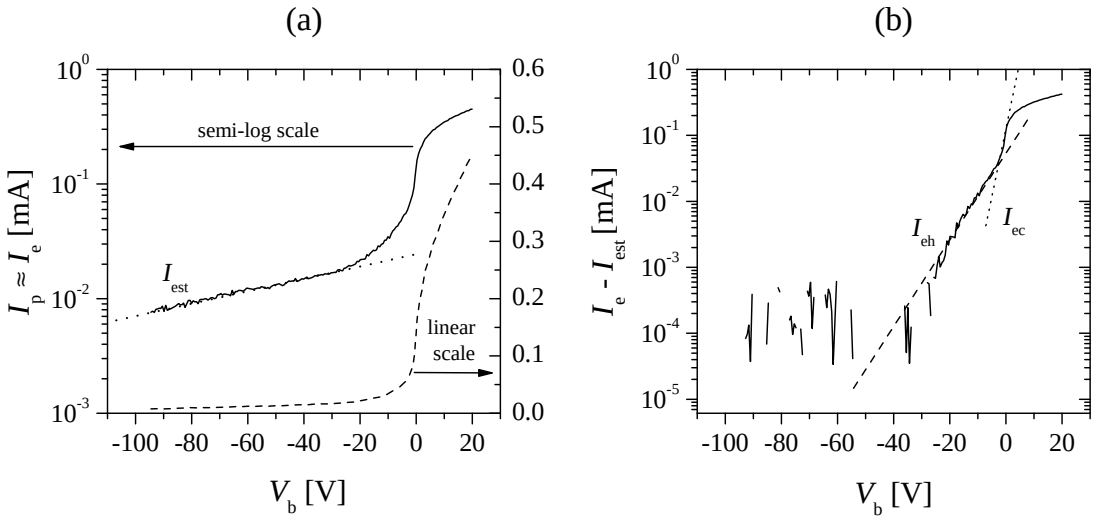

Figure 4.2: (a) The abnormal probe I-V characteristics showing no more ion current in the range of probe potential V_b. The probe characteristic is plotted in a linear and log scale, showing the hottest electron component, I_{est}. (b) A plot of electron current after subtracting the I_{est} component revealing hot (I_{eh}) and cold (I_{ec}) components.

pulse $t \sim 1 - 4\,\mu$s up to three electron current components can be observed in the probe characteristics. These components are apparent in the form of the recorded probe I-V curves on a linear plot, but they become particularly clear in a semi-log plot as illustrated in the example used in figure 4.2(a). The distinct straight-line forms of the latter indicate the presence of three electron groups, each indistinguishable from Maxwellian distributed electrons. These electron current components are denoted by I_{est}, I_{eh}, I_{ec} as a consequence of super-thermal, hot and cold electron distributions respectively.

In this early phase of the pulse, no floating potential V_f in the probe characteristic can be observed since V_f is considerably more negative than the available probe potential of the acquisition system (-95 V). As a consequence no discernable positive ion current can be observed in the I-V characteristics, that is, the total probe current I_p never changes sign to fall below the $I_p = 0$ line. Since the theoretical ion currents are smaller in magnitude than any of the total currents measured, even at the deepest obtainable negative probe potential of -95 V, the probe current I_p (as shown by the linear-scale dashed line in figure 4.2(a)) is approximately equal to the total electron current I_e. In other words, $I_p \approx I_e$ when $V_f < -95$ V.

The individual electron components can be readily retrieved from the total electron current I_e as follows. The I_{est} component (the dotted line in figure 4.2(a)) can be determined directly from the linear portion of the semi-logarithm plot of the total electron current I_e (the solid line in figure 4.2(a)). After subtracting the I_{est} component from the I_e (see the solid line in figure 4.2(b)), the I_{eh} and I_{ec} components are then obtained from the dashed and dotted lines construction as also shown in figure 4.2(b).

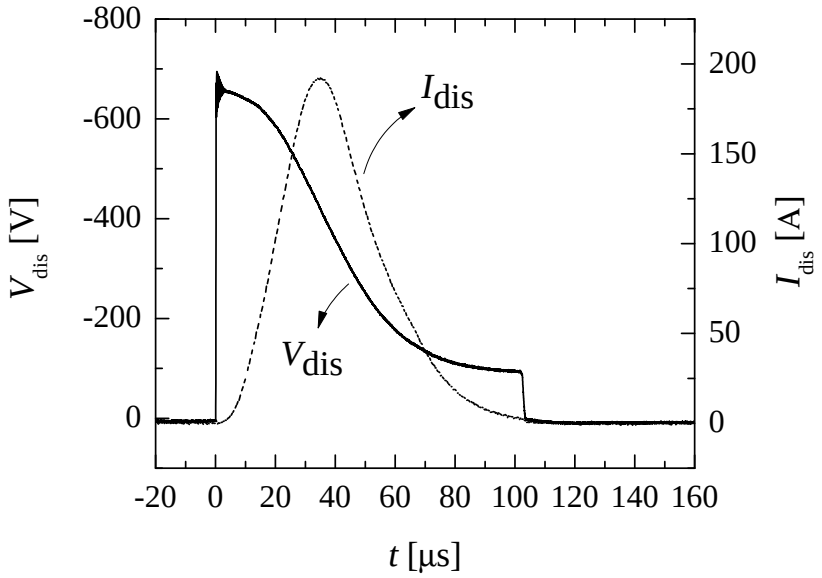

Figure 4.3: Plots of discharge voltage (V_{dis}) and current waveforms (I_{dis}).

The characteristic Maxwellian temperatures and densities of the electron groups are T_{est}, T_{eh}, T_{ec} and n_{est}, n_{eh}, n_{ec} respectively. As described in the Chapter 3, temperatures of Maxwellian electrons can be calculated from slopes of the linear portions of $\mathrm{Ln}(I_{\mathrm{e}})$ versus V_{b} plot. A simple extrapolation of the linear portions of the semi-log plot back to the plasma potential Φ can yield the individual electron saturation current components $I_{\mathrm{ex,SAT}}$ from which the electron densities of each group can be found using,

$$n_{\mathrm{ex}} = \frac{I_{\mathrm{ex,SAT}}}{eA_{\mathrm{p}}\sqrt{(k_{\mathrm{B}}T_{\mathrm{ex}})/(2\pi m_{\mathrm{e}})}}, \tag{4.1}$$

where the subscript x represents either the super-thermal, hot or cold electron groups respectively. Here A_{p} ($= 2\pi r_{\mathrm{p}} l_{\mathrm{p}}$), is the probe surface area, k_{B} the Boltzmann constant and m_{e} the electron mass (see Appendix A.2). Note that the plasma potential Φ was taken by the second derivative of the I-V characteristics as described in section 3.2.3.

4.3 Results and discussions

4.3.1 Characteristic of the discharge

The discharge voltage V_{dis} and current I_{dis} waveforms of the HiPIMS plasma are shown in figure 4.3 for a peak power density of $500\,\mathrm{Wcm}^{-2}$, operated at the pressure of 0.5 Pa. A noticeable oscillation of V_{dis} is observed initially for a few microseconds becoming flat in the period $t \sim 4-10\,\mu$s. The voltage V_{dis} was sustained at a set-point level of $-650\,$V during the first $5\,\mu$s while the plasma impedance remains high ($> 100\ \Omega$). However, the voltage gradually falls throughout the pulse to about -100 V at $t \sim 100\,\mu$s as the plasma impedance decreases (to $\sim 2\ \Omega$). As the discharge develops, I_{dis} climbs up to

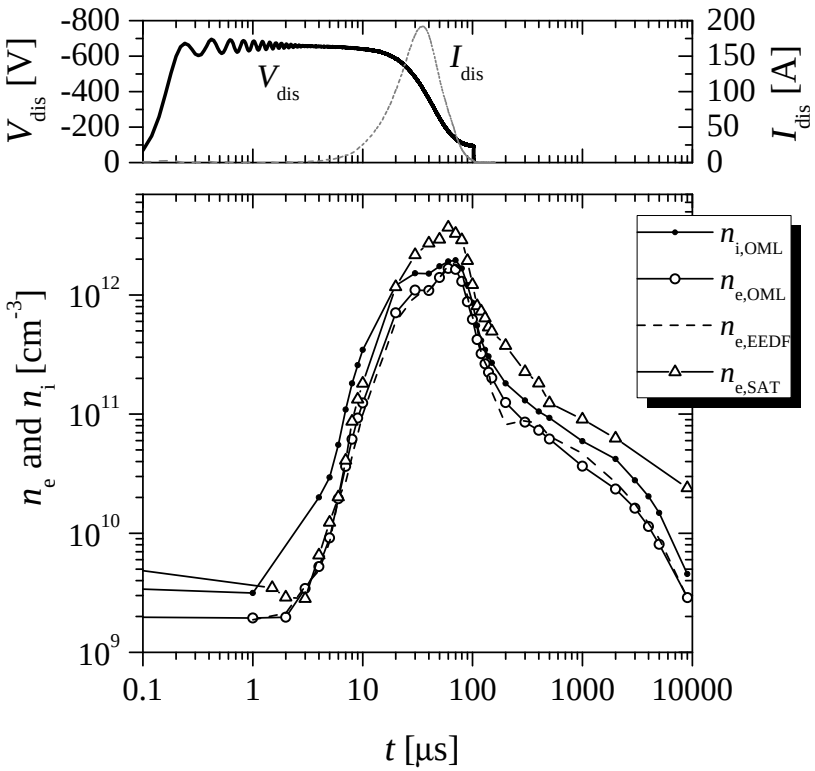

Figure 4.4: The temporal density of electrons (n_e) and ions (n_i) (in a log scale) calculated from the OML theory, the EEDF plots and the electron saturation points.

its peak of 200 A at $t \sim 35\,\mu$s before decreasing rapidly down to its termination at $\sim 103\,\mu$s.

In figure 4.4 the temporal electron densities throughout the HiPIMS period are plotted compared for three calculating methods. The electron densities were calculated from (1) the OML theory, (2) the EEDFs integration from Druyvesteyn formulation and (3) the electron current at the plasma potential. In addition, the comparison between temporal electron and ion densities obtained from the OML analysis is also shown. The EEDF and OML techniques agree well (within 15 %) showing electron densities rising up from an initial value of $\sim 2 \times 10^9$ cm^{-3} at $t < 1\,\mu$s to a first peak value of $\sim 1 \times 10^{12}$ cm^{-3} at $t \sim 35\ \mu$s and a larger second peak value of $\sim 2 \times 10^{12}$ cm^{-3} at $t \sim 70\ \mu$s as clearly seen in a linear scale in figure 4.5. Here the two peaks in the temporal electron density are observed during the pulse on-time which is in contrast to the results of Alami *et al.* [93], who observed for the relative high pressure of 20 mTorr two similar peaks, however with the second peak occurring in the pulse off-time. Here, the first peak occurs at a time corresponding to the maximum in the discharge current ($I_{\text{dis}} \sim 200$ A), however the second peak occurs when the discharge current has already fallen to ~ 50 A. This bimodal distribution of plasma density in time has also be observed by optical emission spectroscopy (OES) [59] and mass spectrometry (MS) [60] in other titanium HiPIMS discharges, with evidence that the first density peak is due to

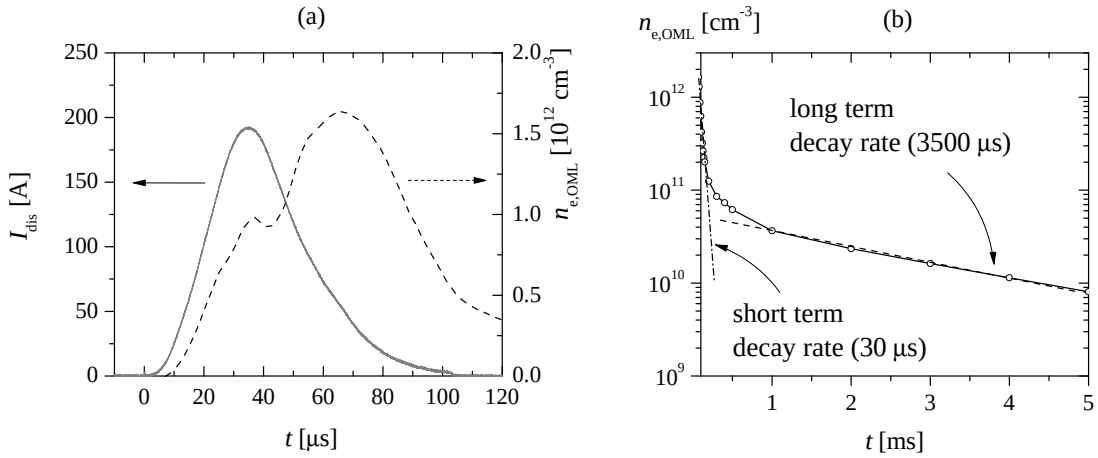

Figure 4.5: (a) A temporal $n_{\mathrm{e,OML}}$ mapping with I_{dis} in a linear scale showing two peaks of n_e during the pulse on-time. (b) A temporal $n_{\mathrm{e,OML}}$ during afterglow period showing two terms of the decay rate.

the dominance of Ar^+ ions while the second peak is due largely to Ti^+. Using the 40 μs time delay between the first and second density peaks, the drift velocity of titanium ions travelling from the cathode region to the probe is approximately $2.5 \times 10^3\,\mathrm{m\,s^{-1}}$ which correspond to an energy of 1.6 eV. Macák *et al.* [59] reported the average drift velocity of sputter Ti to be approximately $2.1 \times 10^3\,\mathrm{m\,s^{-1}}$ for a HiPIMS operating pressure of 1.1 Pa. The value of the speed obtained here may be marginally higher due to the lower operating pressure of 0.5 Pa.

After reaching its peak value at $t \sim 70\,\mu$s, the electron density falls for the remainder of the pulse cycle, however with two characteristic decay times τ_{n1} and τ_{n2}. The first rapid decay phase occurs from $t \sim 70 - 200$ μs with $\tau_{n1} \sim 30$ μs while the second slower phase from $t \sim 1000 - 9000$ μs has a τ_{n1} of ~ 3500 μs as shown from a plot of the logarithm of electron density versus time in figure 4.5(b). Table 1 shows these τ_{n1} and τ_{n2} values for a range of pressures and target power densities. Long-lived plasmas with significant charged particle densities remaining up to 20 ms into the HiPIMS discharge afterglow at pressures ~ 0.12 Pa have also been observed by Anders and Yushkov [94]. This phenomenon is not understood but has been speculated in [94] to be associated with the existence of long-living metastable Ar atoms ($1s_3$ and $1s_5$) in the plasma that prop-up the plasma density. The main mechanism during the afterglow is the inelastic collision between an electron and the metastable atoms as written as

$$\mathrm{e} + \mathrm{Ar}^* \rightarrow 2\mathrm{e} + \mathrm{Ar}^+.$$

The existence of a relatively dense remnant plasma ($n_e \sim 2 \times 10^9$ cm^{-3}) at the beginning of the subsequent on-time will seed the discharge and aid discharge development.

From figure 4.4 we can see that despite good agreement between the OML and EEDF methods, the electron density $n_{\mathrm{e,SAT}}$ determined from the electron saturation

current is consistently higher than that found from the OML method (with value of $n_{e,sat}/\ n_{e,OML}$ approximate to 2.5) during the on-time. This may have been due to an overestimation in the measured values of Φ; however, the overall density trends in time between methods are very consistent. It can also be seen from figure 4.4 that the OML estimation of ion density $n_{i,OML}$ is higher than the electron density $n_{e,OML}$ by a factor between 2 and 4. This can be understood by considering the transport of low energy electrons to the probe in the presence of the magnetic field at the probe position. When T_e is small, i.e. during the decay phase when $T_e < 0.5$ eV the electron gyro radius r_{gy} can become comparable to the sheath dimensions λ_{De} (or probe radius r_p) and the collected electron current can be reduced. This effect, due to the magnetic field, has been observed and modelled for pulsed DC magnetron plasmas [95] and can account for the difference between $n_{i,OML}$ and $n_{e,OML}$ observed here extremely well using a value of the B-field at the probe position.

The evolution of the plasma Φ and floating V_f potentials are shown in figure 4.6. Their initial values in the period $0 < t < 1\,\mu$s are +2.7 V and 0 V, respectively, indicating the presence of a remnant plasma from the previous off-phase. For times up to $t \sim 3\,\mu$s, Φ does not vary however it does decrease monotonically to -13 V at $t \sim 10\,\mu$s, after which it climbs to positive values (up to +6.5 V) after $t > 50\,\mu$s.

The observation of negative values of Φ over the first half of the on-time phase is somewhat different from those of measured experimentally by Gudmundsson *et al.* [92] and predicted through modelling by Brenning *et al.* [96] who both showed positive values of Φ in this phase. However Mishra *et al.* [50] has revealed that the Φ profile, measured from an emissive probe, depends strongly on the B-field strength and its configuration, with lower field strengths elevating Φ towards ground potential. Lower B-fields at the target lead to less electron trapping in the closed magnetic flux and as predicted by Van Der Straaten *et al.* [97] less negative space charge and weaker bulk plasma electric fields. The different between the results here and those of Gudmundsson *et al.* [92] and Brenning *et al.* [96] may therefore be due to the significantly stronger magnetic field strengths in the magnetron used in this study compared to those in aforementioned

Table 4.1: The short-term and long-term decay times of the plasma parameters obtained in the off-time for a number of different argon pressures p and peak discharge target densities P_{dis}.

P_{dis} (Wcm^{-2})	Pressure (Pa)	$n_{e,OML}$ decay time (μs)		T_e decay time (μs)		Φ decay time (μs)	
		Short	Long	Short	Long	Short	Long
500	0.5	30	3550	52	150	260	420
500	1.1	35	3970	34	85	193	575
500	1.6	39	4290	38	85	134	575
1000	0.5	34	2980	164	746	292	493

studies.

The time at which Φ reaches ground potential corresponds to a time close to the maximum in the plasma density. It is interesting that for at least 50 % of the pulse on-time Φ remains significantly below ground potential, and hence only very energetic sputtered ionised metal particles in this period ($E_{\text{sputter}} > 10 - 20$ eV) could overcome the potential barrier to reach a grounded substrate or vessel walls. In the off time, Φ initially decays with a short-term decay time constant of ~ 200 μs lengthening to a long-term constant of ~ 500 μs (see table 1).

In contrast to Φ, the floating potential V_{f} has a more dynamic form, particularly in the first 4 μs, where V_{f} rapidly decrease to very negative values, well below the -95 V detection limit of the Langmuir probe acquisition system. To determine V_{f} during the period $t \sim 1 - 4$ μs, another probe bias technique with an external resistor on the bench top was employed (see section 3.2.3). The floating potential V_{f} obtained from the bias technique is plotted in figure 4.7 in comparison with that obtained from Langmuir probe and from electron temperature data. Note that V_{f} is not necessary to in phase with and Φ i.e. the moment at which V_{f} and Φ reach the minimum point are not on the same time. The difference between V_{f} and Φ for an acquiring time strongly depends on the electron temperature for that moment.

After the initial 4 μs V_{f} then follows Φ in profile (see figure 4.6), obtaining values

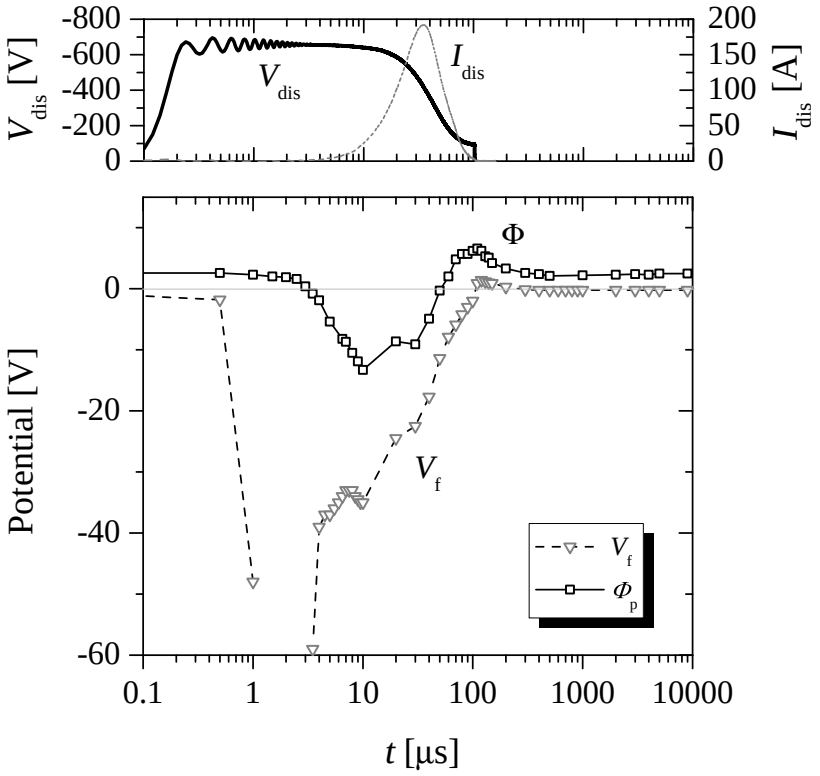

Figure 4.6: The temporal floating (V_{f}) and plasma (Φ) potential.

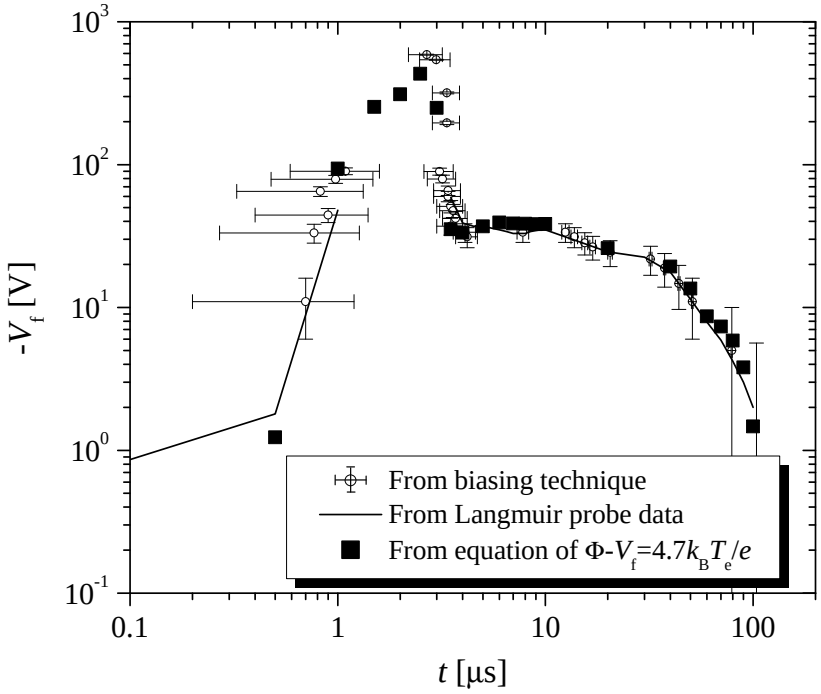

Figure 4.7: A comparison of the temporal evolution of the floating potential obtained from three different methods, namely from the Smart probe acquisition system, from the biasing technique and estimated from the measured electron temperature (T_e) and plasma potential (Φ) values using the relation $V_f \sim \Phi - 4.7 k_B T_e/e$, where T_e is the hottest electron group in the discharge, i.e. T_{est}

between 0 and −40 V. One possibility for the extremely deep floating potentials in this initial 4 μs (when the plasma potential remains constant) is the presence of energetic electrons in the plasma which are known to be able push the floating potential very negative even when they are in very small concentrations (i.e. $< 0.1\%$ of the bulk electron density) [98]. This picture of the short-lived existence of energetic electrons is borne out by the electron temperature measurements shown in figure 4.8.

To determine the electron temperature T_e throughout a cycle, the inverse gradient of the semi-log plot of electron current versus probe bias is determined. During the time $t \sim 0 - 1$ μs, when plasma density is very weak ($\sim 2 \times 10^9$ cm^{-3}) and for times $t > 4$ μs, as the plasma builds up, the electron temperature can be directly determined from a single slope indicating one temperature component in the plasma. In the initial discharge stage $t \sim 0 - 1$ μs these electrons are cold with the temperature T_{ec} while the temperature of the single Maxwellian electrons for $t > 4$ μs is designed as T_e, see figure 4.8. During $t \sim 1 - 4$ μs when the deep negative V_f measurements are obtained the ion saturation current cannot be detected (due to the limit in the negative voltage range of the probe system), however as described previously, three distinct slopes in the semi-log plot can be observed indicating the simultaneous presence of three groups of electrons (indistinguishable for Maxwellian electrons) in that period, see figure 4.2. It is worth

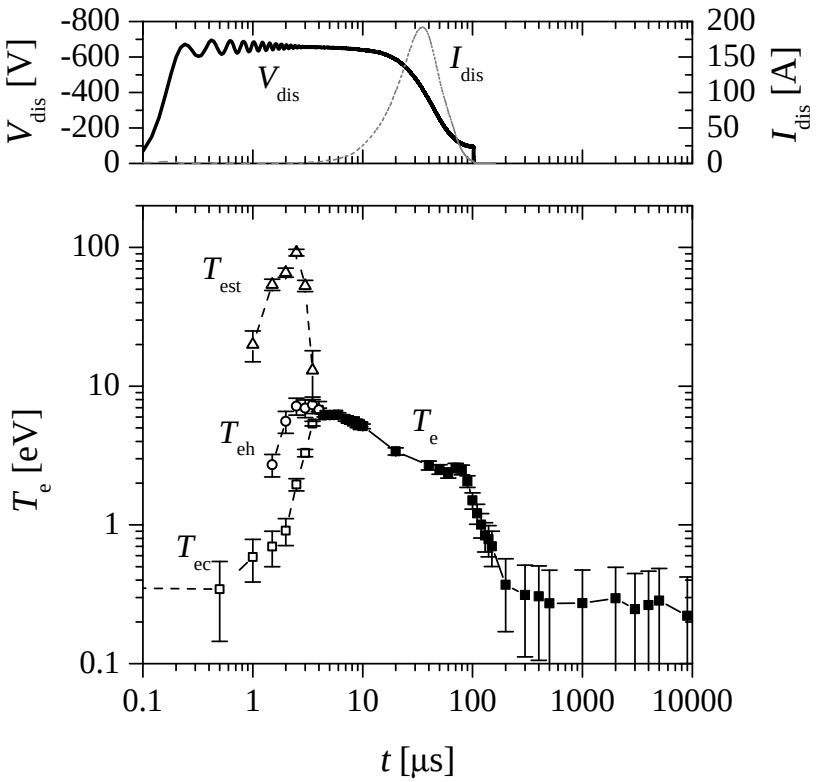

Figure 4.8: The temporal temperature of a different groups of electrons namely supter-thermal, hot and cold electrons.

emphasising that the lack of ion saturation current in the probe characteristics during this period is a consequence of deep floating potentials and not a current off-set of error in the measurement. Despite the lack of detection and removal of $I_{\mathrm{i,OML}}$ from the total current I_{p} it does not affect the interpretation that the slope in the tail of the measured current at deep biases is due to super-thermal electrons. These super-thermal or beam-like electrons are generated by the dynamic motion of the sheath and they have T_{est} values up to 100 eV and persist for a duration of 3 μs. After subtracting the super-thermal electron current component from the total probe current I_{p}, a subsequent plot of $\mathrm{Ln}(I_{\mathrm{p}} - I_{\mathrm{est}})$ versus V_{p} can be used to determine the temperatures of the hot T_{eh} and cold T_{ec} groups respectively, see figure 4.2(b).

The temporal evolution of electron temperature over the full cycle, shown in figure 4.8, reveals a complex structure with some coupling between the three distributions. It can be seen that the cold electrons are heated from an initial value of T_{ec} of 0.2 eV to 7 eV over the first 4 μs while the hot and super-thermal groups both increase and then decrease in temperature reaching the same equilibrium temperature as the heated cold electrons. The maximum effective temperatures of super thermal and hot electron groups are $\sim$ 100 eV and $\sim$ 7 eV at $t \sim 2.5$ μs respectively. For $t > 4$ μs, only one (merged) electron group with a single temperature T_{e} can be observed. For the remainder of the on-time, T_{e} falls as the plasma density rises, reaching $T_{\mathrm{e}} \sim 2.5$ eV

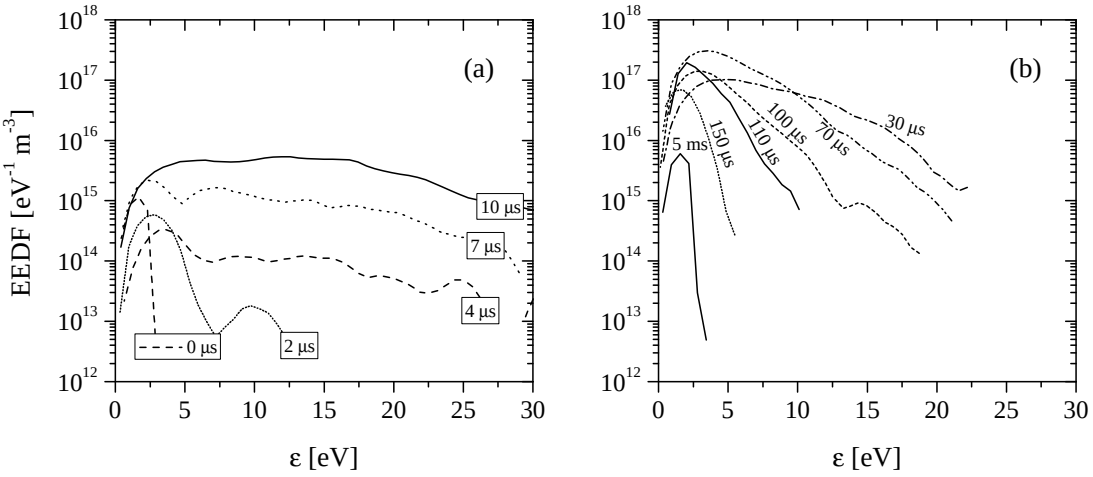

Figure 4.9: The evolution of the EEDFs at selected times during the entire pulse cycle (a) t = 0 −10 μs and (b) t = 30 μs − 5 ms.

at the end of the on-time. After the pulse termination, T_e falls to 0.2 eV at $t \sim 300\,\mu$s and remains for the rest in the pulse off-time.

The relationship between the floating V_f and plasma Φ potentials in figure 4.6 can be understood from the measured electron temperatures T_e in figure 4.8. Assuming OML ion collection and Maxwellian electrons of highest temperature component T_e, the floating potential V_f can be found simply by equating the OML ion currents (see equation 3.1) and the Maxwellian electron currents I_e where

$$I_e \approx eA_p n_e \sqrt{k_B T_e / 2\pi m_e}\, \exp\left(-e(\Phi - V_b)/k_B T_e\right). \tag{4.2}$$

Assuming plasma quasi-neutrality, $n_e = n_{i,OML}$ with $V_b = V_f$, the solution of $\Phi - V_f = 4.7 k_B T_e/e$ is thus obtained numerically. From this relationship V_f has been estimated using Φ and the highest instantaneous value of electron temperature during the pulse on-time. For example, T_{est} is used in the calculation for $t \sim 1 - 4\,\mu$s. The calculated V_f are shown in figure 4.7 (the solid square dots). There is clearly good agreement between these calculated values, the measured Langmuir probe results and the separate biasing technique data as described above, indicating strongly that the super-thermal electrons do exist and have effective temperatures T_{est} up to 100 eV so pushing the floating potential down to below −500 V in the period $1 < t < 4\,\mu$s. The existence of super-thermal electrons during the early stages of the voltage pulse may aid the establishment of the plasma and enhance the build-up of the discharge current through extra ionising collisions. In addition, residual plasma ions from the previous pulse may get accelerated to high energy in the very deep negative floating potentials so bombarding insulating surfaces in the vessel. This would effectively lead to some beneficial ion cleaning.

Using equation 3.5 the electron energy distribution functions (EEDFs) at a number

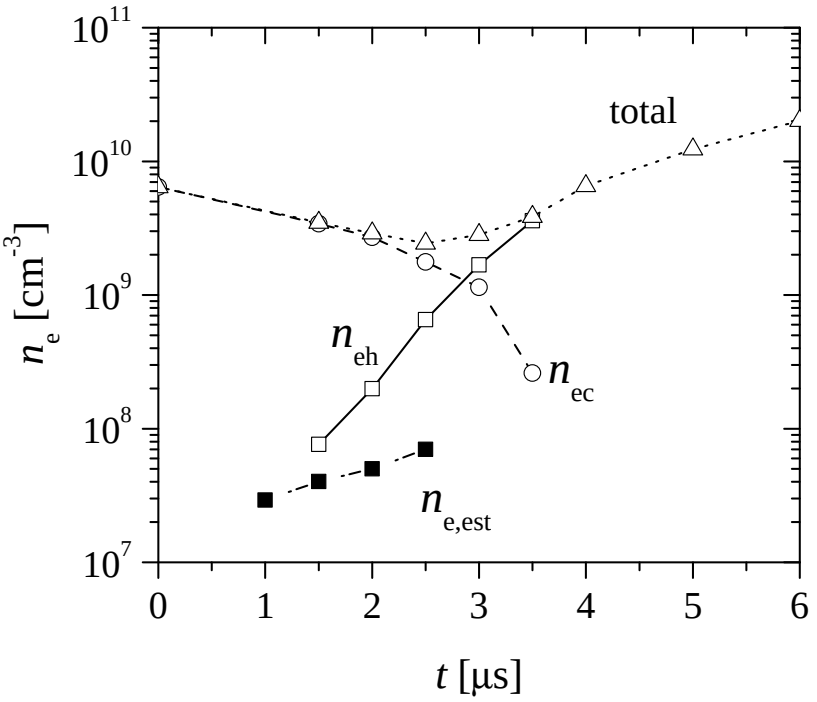

Figure 4.10: A plot of the calculated electron densities for the three identified electron groups in the discharge, namely the super-thermal, hot and cold groups during the first 6 μs of the on-time. The electron density values where determined from the magnitude of the electron current components extrapolation to the plasma potential.

of chosen times during the on and off phases of the pulse have been found for the same magnetron conditions as above, namely a peak target power density of 500 Wcm^{-2} and an argon pressure of 0.5 Pa and these are shown in figure 4.9. At $t \sim 0\,\mu$s, $g_e(V)$ has small amplitude and little extension in tail energy, consistent with the electron density $n_{e,OML}$ and T_{ec} measurements in figures 4.4 and figure 4.8. For the period $2 < t < 4\,\mu$s the distribution functions have extended tails indicating the presence of energetic electrons, however all three temperature component (T_{est}, T_{eh}, T_{ec}), as determined from the semi-log plots (figure 4.2), can not be observed. This may be due to a lot of noise in the second derivative data.

It is interesting to note that during the time interval $0 < t < 4$ μs, the amplitude (and integrated area) of high-energy tails of the EEDF increases while the low-energy portion in the EEDF decreases. This indicates that the hot group increases at the expense of the cold group and agrees qualitatively with the more precise density measurements of each group (n_{eh}, n_{ec}) derived directly from the electron current (using equation 4.1) as shown in figure 4.10. In particular, we can see that n_{ec} decreases from its initial value of 6×10^9 cm^{-3} at $0\,\mu$s to 2×10^8 cm^{-3} at $4\,\mu$s while n_{eh} increases from 8×10^7 cm^{-3} to 5×10^9 cm^{-3} and dominates the total electron density ($n_{est} + n_{eh} + n_{ec}$) for the rest of the pulse. For the super-thermal group, n_{est} increases marginally from 3×10^7 cm^{-3} to 6×10^7 cm^{-3} during the period $1 < t < 3\,\mu$s. These densities are less

than 3 % of the total electron density. For times, $t > 4\,\mu$s the super-thermal electrons cannot be detected due to their associated electron current is below the current detection limit of the probe system. The low energy electrons ($T_e \sim 0.2\,$eV) remaining in the plasma from the previous pulse gain energy in the evolving bulk plasma electric field to establish a growing hot group. Also, a few microseconds after pulse initiation, ion sputtering of the target will generate secondary electrons and these may collisionally relax contributing to the increasing hot group. For times $t > 4\ \mu$s only a single electron distribution is observed which cools both in the remainder of the on-time and for all of the off-time.

Beam-like or super-thermal electrons have already been detected in other pulsed magnetron plasmas during the initiation of the voltage pulse [98]. It has been conjectured that they result from acceleration to high energies in the rapidly advancing cathode sheath that transports them to the plasma bulk. It has also been argued that such sheath motion in the presence of large magnetic fields at the cathode can lead to stochastic bulk electron heating as described in [99, 100]. From figure 4.8 we see that there is a delay of about $1.0\,\mu$s after the voltage pulse initiation before the energetic electrons first reach the probe (a distance 10 cm from the cathode), and a further delay of $1.4\,\mu$s before the highest temperatures ($T_{est} \sim 100$ eV) are established. This gives an estimate of effective drift velocity of the super-thermal group to be up to 10^5 ms^{-1}, which is considerably slower than the average thermal speed of electrons in the distribution, which is $\sim 6 \times 10^6$ ms^{-1}, however such slow diffusion or collective drift speeds have been observed in pulsed DC magnetrons [101] at lower operating powers. The transport of these energetic electrons from the sheath region just above the racetrack, across the closed magnetic field lines of the magnetic trap to the probe is discussed in more detail in [102].

The two other groups detected here, namely the hot ($T_{eh} \sim 6 - 7$ eV) and cold ($T_{ec} \sim 1 - 2$ eV) distributions have also seen in the early stages of other HiPIMS discharges, derived from an analysis of the EEDF [90]. However the two groups reported in [90] persist together for times up to $40\,\mu$s before merging to a single distribution and not just a few microsecond as reported here. Hot electrons ($\sim 17\,$eV) and anomalously deep associated floating potentials (more negative than $-160\,$V) have also been observed at time less than $10\,\mu$s from pulse initiation in the relative low peak current (5 A) HiPIMS sputtering of Cu [91]. The hot groups reported in [90, 91] may correspond to the hot group observed here, however they certainly have very different temperatures and temporal dynamics to the super-thermal electrons found in this study.

4.3.2 Effect of operating pressure

The effects of operating pressure p on the plasma parameters have also been investigated. Figure 4.11 shows that with increasing pressure (from 0.5 to 1.6 Pa) the plasma

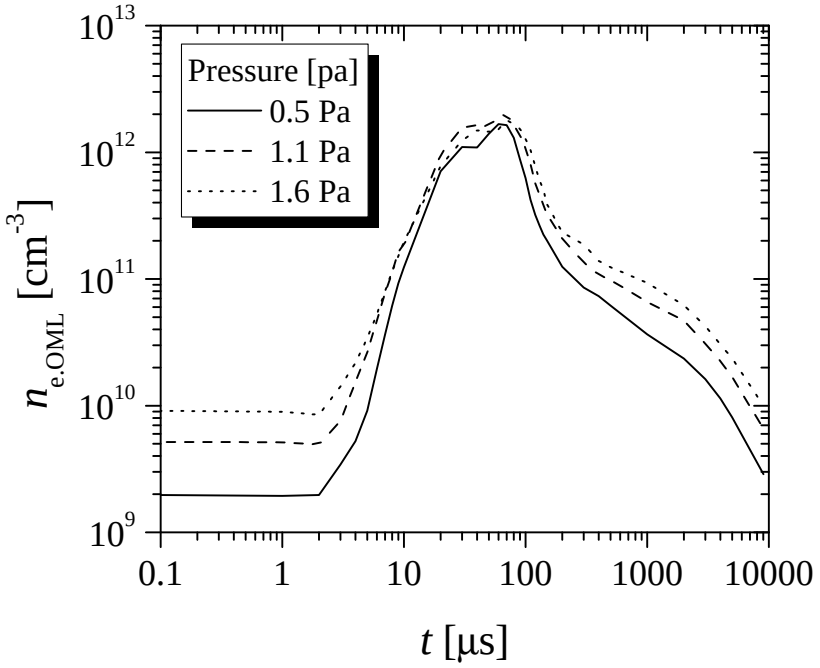

Figure 4.11: Plots of temporal total electron density ($n_{\mathrm{e,OML}}$) estimated from an OML analysis for different operating pressure.

density increases at all times in the pulse cycle except for the peak density ($t \sim 70$ μs), which is insensitive to pressure (varies from only 1.6×10^{12} to 2.1×10^{12} cm^{-3}). This may be due to the fact that the discharge density is dominated by the sputtered post-ionised metal rather than the argon gas ions. The argon plasma density at the start of the on-time (i.e. the remnant from the previous off-time) is clearly sensitive to pressure, with the density increasing from 3×10^9 to 1×10^{10} cm^{-3} over the pressure range. During the pulse off-time, an increased operating pressure results in a marked increase in both the short-term and long-term plasmas density decay times, for instance τ_1 increase from 30 to 39 μs and τ_2 increases from 3550 to 4290 μs (see Table 1). This can be understood from increased total (in-elastic and elastic) collision rates ν_{c} which reduces the effective diffusion coefficient for electrons transported across the plasma [103]. The long-term decay time can also be calculated from the effective time ions fall through the decaying sheaths at the grounded walls, given by $\tau_2 \sim L/C_{\mathrm{s}}$ where L is the characteristic plasma dimension and C_{s} the ion acoustic speed $C_{\mathrm{s}} = \sqrt{k_{\mathrm{B}} T_{\mathrm{e}}/M_{\mathrm{i}}}$. In our case, L, (the mean distance from the plasma axis to the vessel wall) ~ 0.20 m and $T_{\mathrm{e}} \sim 0.2$ eV giving a longest decay time ~ 0.3 ms which is one order of magnitude lower than measured values (τ_2) of $3-4$ ms. Since this simple model of the ion transport ignores the role of excited species such as Ar metastables, it indicates that such species may be important in maintaining the plasma density in the afterglow as suggested by Anders and Yushkov [94].

The temporal evolution of the plasma Φ and floating potentials V_{f} are shown in

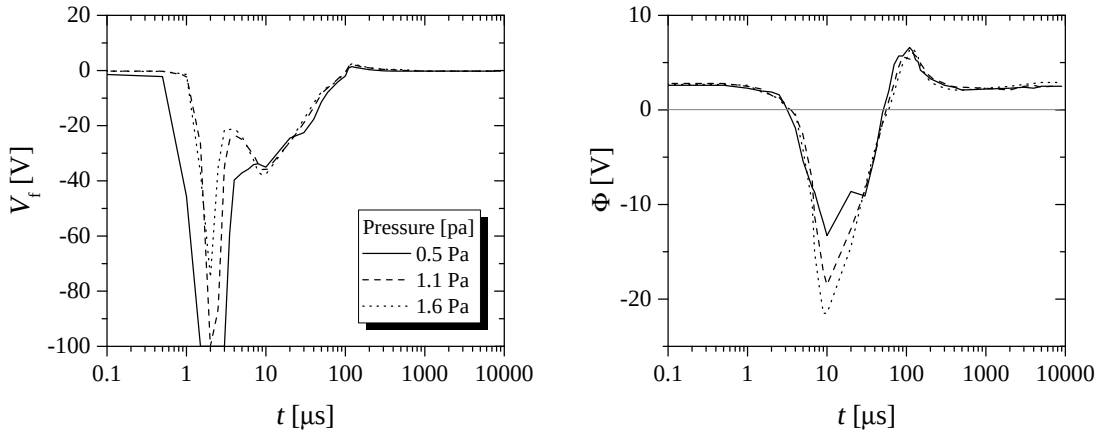

Figure 4.12: Plots of the temporal evolution of the floating V_f and Plasma Φ potentials in different Ar pressures

figure 4.12. For the plasma potential Φ the minimum value ($t \sim 10\,\mu$s) increases to a more negative value from -13 V at 0.5 Pa to -23 V at 1.6 Pa. The presence of the this marked dip in Φ seen in figure 4.6 and 4.12 is not understood however, in this period the plasma density (still dominated by argon ions) is increasing, but sputtered Ti atoms and Ti ions (of typical speed 10^6 cm s^{-1}) will begin to reach the probe position. Electrons will begin to cool in this period (as seen in figures 4.8 and 4.13) as they give up energy in ionisation and excitation of the sputtered titanium atoms. The plasma potential may in this period by necessity acquire negative values to promote the transport of (cooling) electrons across the magnetic field lines to the anode walls to maintain current continuity.

From figure 4.12 we see that increasing the pressure has a significant effect on the V_f profile particularly during the period $t = 1 - 4\,\mu$s where the absolute value of the deep floating potentials (due to the presence of beam-like electrons) is decreased. For instance, V_f is elevated from values well below -100 V at 0.5 Pa to -70 V at 1.6 Pa. In addition, the time over which the negative value in V_f persist (measured at $V_f \sim -45$ V) decreases from 2 to 0.8 μs as the pressure is increased from 0.5 Pa to 1.1 Pa. During the pulse off-time, the short-term characteristic decay times of Φ decreases from 260 to 134 μs while the long-term increases marginally from 420 to 575 μs (see on Table 1) with increasing pressure.

The effect of the operating pressure on the evolution of T_e is presented in figure 4.13. It shows clearly that the temperature for all three-electron groups; T_{est}, T_{eh}, and T_{ec} decrease with increased pressure, due to an increase in the in-elastic collision frequency (ionisation and excitation of argon). Interestingly, we can see from figure 4.13 that the T_{est} value both reduces in magnitude and time of persistence ($\tau_{persist}$) in the discharge as the pressure increased. For example, T_{est} peak temperatures decreases from 100 to 30 eV as the pressure is increase from 0.5 to 1.6 Pa and $\tau_{persist}$ decreases from 2 μs to

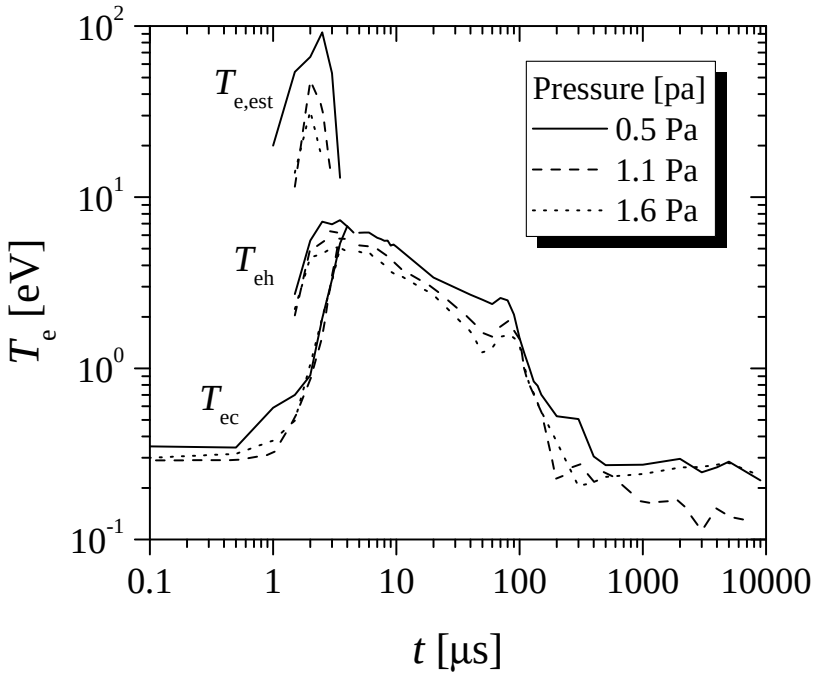

Figure 4.13: Plots of the electron temperatures for different operating pressure.

1 μs. During the pulse on-time for $t > 4\,\mu$s, the temperature values of the merged single Maxwellian electron group decreases by 50 % with increased pressure. In addition, the short and long term decay times of T_e (see Table 1) are reduced, i.e. from 52 to 38 μs and from 150 to 85 μs respectively. This is consistent with increased collision rates which cool the electron distribution, and is also consistent with lengthening plasma density decay times as described above.

4.4 Conclusions

The temporal evolution of plasma parameters at the substrate position in HiPIMS discharge have been obtained throughout the entire pulse period using a Langmuir probe for a number of different operating conditions. The results reveal both short-term and long-term phenomena, including the generation of super-thermal or beam-like electrons with effect temperatures up to 100 eV in the first 4 μs of the applied voltage pulse. These electrons greatly depress the floating potential to voltages below -500 V for periods between 1 and 2 μs depending on the operating pressure. The probe analysis also reveals two other distinct electron groups, indistinguishable from Maxwellian electrons, during this initial period, hot electrons of temperature up to 7 eV and cold electrons of temperatures < 1 eV. However as time progresses all three distribution become indistinguishable from each other to from a single group that cools for the rest of the on-time and then more quickly in the off-time. The characteristic decay in the afterglow for the plasma density, electron temperature and plasma potential show two-

fold decay times, (fast and slow), with the slow density decay times in excess of 4 ms, which leads to a relatively dense plasma existing in the vessel even at the end of the off-time i.e. after 10 ms. This clearly aids re-ignition of the plasma in the subsequent on-time, and provides seed electrons in the system.

Chapter 5

Low-pressure operation technique

5.1 Background

The collision-free or ballistic transport of sputtered particles plays an important role in the energetic condensation of metal at a substrate forming well-structured films [104]. This normally takes place at low operating pressures where the mean-free-path for collisions of the sputtered particles is longer than the target-to-substrate distance. For magnetron sputtering systems, the ballistic transport can be achieved when operating at pressures lower than 0.13 Pa, while pressures above 1.3 Pa result in the thermalisation of the sputtered particles via scattering with the background gas, and the sputtered atoms are then transported to the substrate by diffusion [105]. Thin films deposited in the regime of ballistic transport tend to have a higher density, a small grain size and comparatively good adhesion. According to the structure zone diagram by Thornton [106], the structure as well as the properties of thin films can be dramatically improved when reducing the operating pressure [107, 108]. In order to decrease the operating pressure of DC and pulsed magnetron sputtering, several techniques have been investigated including using an external plasma source [109, 110], increasing the discharge power [111, 112], optimizing the magnetic field configuration [113–115] and introducing the sputtering gas very close to the target [116, 117].

The operating pressure for HiPIMS discharges is typically higher than 0.13 Pa. However, Andersson and Anders [47] have demonstrated that the HiPIMS discharge with a high sputtering yield target (Cu target) can be operated at a pressure of only 10^{-3} Pa using the assistance of an external vacuum arc plasma source. Anders and Yushkov [94] suggested the use of remnant plasma during the off-time phase to assist the ignition for the next pulse by reducing the off-time interval i.e. increasing the discharge frequency. In their work [94], the operating pressure for a niobium HiPIMS plasma could be minimised to 0.085 Pa with a HiPIMS repetition rate of 1 kHz.

To operate HiPIMS in a low pressure regime, a sufficient background or remnant plasma provided by a pre-ioniser may be required. The superposition technique between a HiPIMS and an auxiliary power supply has been developed by a number of groups

for different proposes. Bugaev *et al.* [118] used a pre-ionisation source to ignite the pulse plasma at pressure 0.6 – 1 Pa. Vašina *et al.* [119–121] proposed the use of a low power DC pre-ioniser for a fast HiPIMS discharge with a very short pulse width of $< 10\,\mu$s at operating pressures between 0.7 – 1.4 Pa. In addition, Bandorf *et al.* [122] also introduced a high power DC discharge in addition with HiPIMS in order to increase the deposition rate at operating pressure of about 0.5 – 2 Pa.

Unlike these previous studies; here, the superposition technique is proposed to operate HiPIMS at low pressures (< 0.1 Pa) using the assistance of a low power DC discharge as a pre-ioniser. In addition, time-resolved Langmuir probe measurements at a typical substrate position have been performed to characterise the plasma. An energy-resolved mass spectrometer has been employed to measure ion energy distribution functions (IEDFs) for both metal and gas ions generated in the low pressure HiPIMS discharge.

5.2 A HiPIMS system

All experiments in this chapter and the next two chapters were carried out in a HiPIMS system which differs from that used in Chapter 4. The new HiPIMS system consisted of three main parts: a vacuum station, a magnetron source and a power supply. The detail for each parts are given as follows.

5.2.1 The vacuum station

The functions of the vacuum station are to provide a high vacuum base pressure ($\sim 10^{-4}$ Pa), control and monitor the necessary process parameters. The vacuum station consists of a vacuum vessel equipped with vacuum pumps, a variety of vacuum components and process monitoring devices.

The geometry of the vessel is ISO-5ways crossed cylinder with a diameter of 260 mm and a height of 325 mm, as shown in figure 5.1. The front flange of the vessel is equipped with a mass spectrometer. The top and the bottom flange are available for a number of plasma probes which can be vertically inserted into the vessel. Vacuum pumps, a turbo molecular pump backed by a rotary vane pump, are connected the vessel at the side flange through a 90° elbow and a butterfly valve. The back flange is reserved for pressure gauges, valves and a magnetron source.

A diagram presenting the essential components of the vacuum station is shown in figure 5.2. There are three main processes occurring on the vacuum station including evacuation, operation and ventilation. The vessel (1) was evacuated to a base pressure below 5×10^{-4} Pa using the vacuum pumps. The rotary pump (5) was employed to initially decrease the pressure down to 1 Pa, monitored by a Pirani gauge (12), before turning on the turbo pump (3) to establish the base pressure, monitored by an inverted

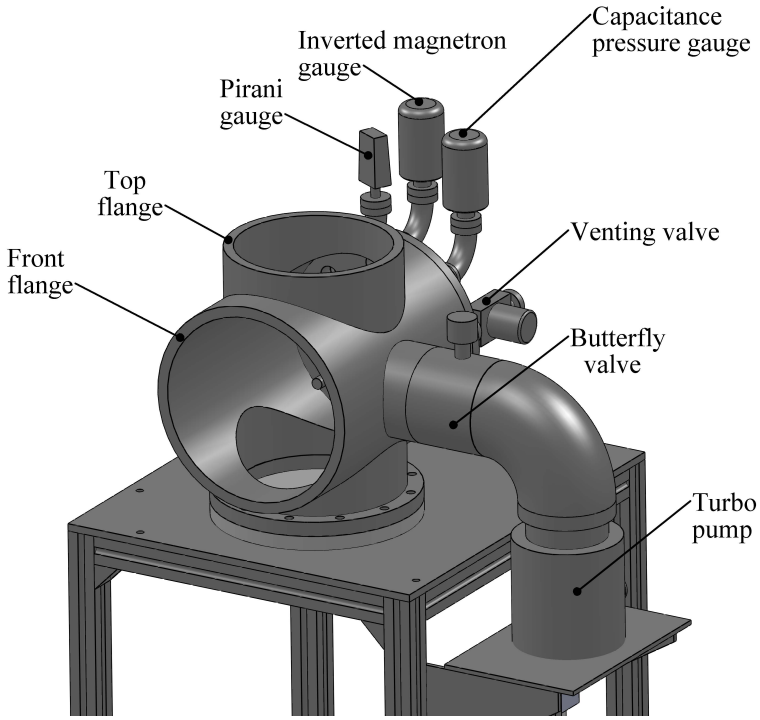

Figure 5.1: A 3-dimensional drawing of the vacuum system shown in a trimetric view. This vacuum system was employed for experiments carried out in this chapter and the rest of the thesis.

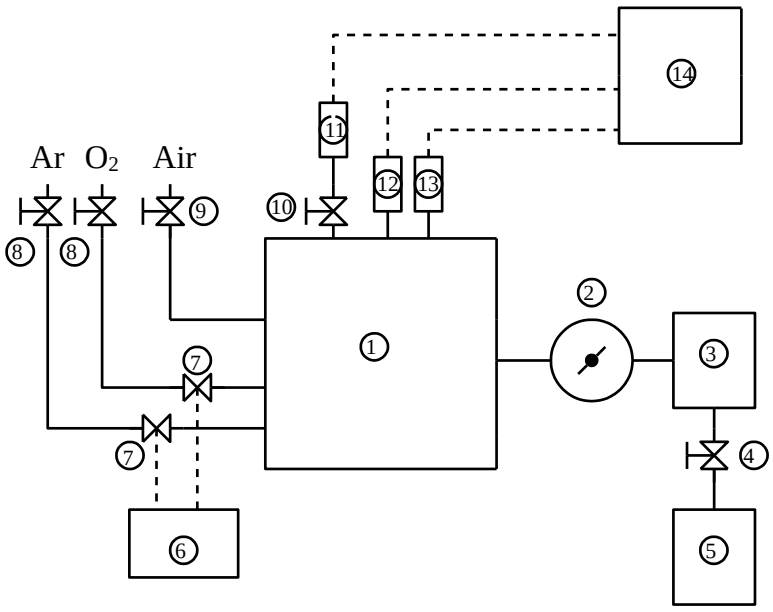

Figure 5.2: A schematic diagram of the vacuum system: (1) chamber, (2) butter fly valve, (3) turbo molecular pump, (4) isolation valve, (5) rotary pump, (6) gas flow readout, (7) mass flow controller, (8) stopping valve, (9) venting valve, (10) ball valve, (11) capacitance pressure gauge, (12) Pirani gauge, (13) inverted magnetron gauge and (14) readout for pressure gauges.

magnetron gauge (13). A selected operating pressure, monitored by a capacitance

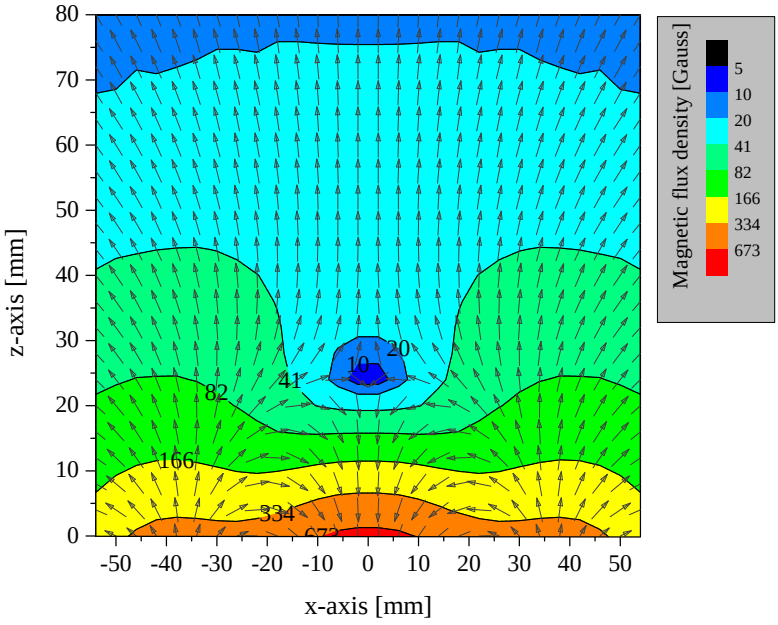

Figure 5.3: The magnetic field mapping of the unbalanced magnetron sputtering system (the target surface is located at $z = 0$ mm)

pressure gauge (11), during HiPIMS discharges was established by introducing argon gas (99.995% purity) through a mass flow controller (7). Before venting the vacuum system, the isolation valve (10) should be closed to protect the capacitance pressure gauge from over-range pressures. After turning off the turbo pump, the argon gas may be introduced to the vessel to slow down the turbo pump. Finally, air can be admitted through the venting valve (9) when the pressure in the vessel was above 10 Pa.

5.2.2 The magnetron source

The magnetron sputtering source, purchased from Gencoa Ltd, is water-cooled circular unbalance magnetron for a target size of 75 mm in diameter. The maximum discharge power of 1.75 kW can be delivered to the source via a RG393 cable. The target can be cooled during operation directly using non de-ionised water with a cooling rate of 1 litre per minute per kW. The target was mounted on a copper cooling plate using an annular clamp. The magnetic materials located behind the copper cooling plate form the unbalanced magnetic field configuration as shown in figure 5.3. In this configuration, the position of the zero magnetic field point or the magnetic null was $\sim$25 mm above the target surface. It is worth mentioning in figure 5.3 that the target surface was located at $z = 0$ with its central at $x = 0$. The centre of the sputtering racetrack was approximately 22 mm from the target centre. In addition, the magnitude of the transverse magnetic field component at the racetrack was about 430 Gauss.

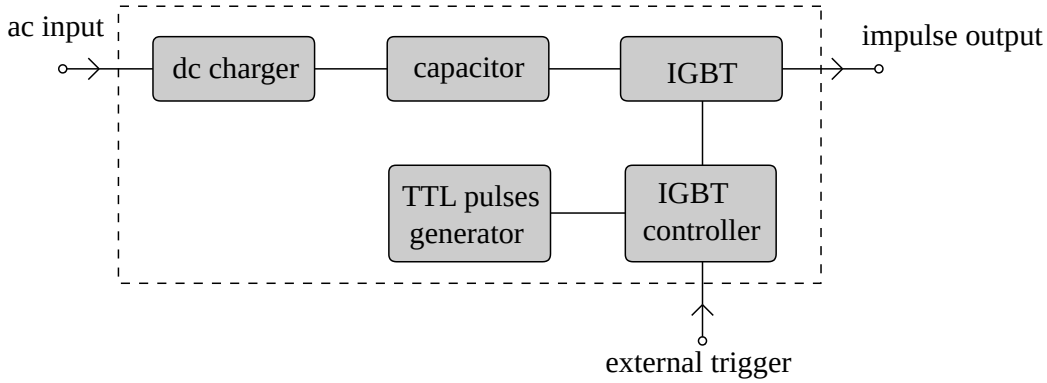

Figure 5.4: A block diagram presenting the essential parts in the impulse power supply unit including a dc charger, an energy storage capacitor, an insulator gated bipolar transistor (IGBT), an IGBT controller and a TTL pulse generator.

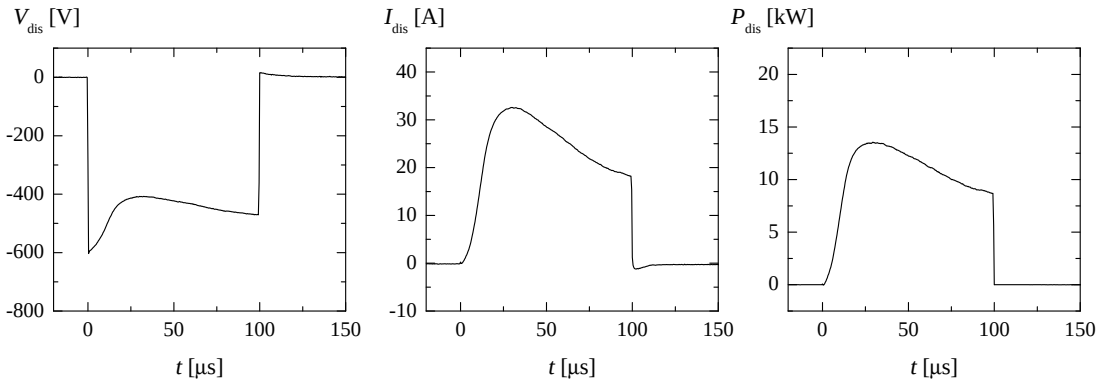

Figure 5.5: The 32 pulses averaged voltage, current and power waveforms of a HiPIMS discharge operated with a pulse width of 100 μs, a pulse repetition rate of 100 Hz, a peak voltage of -600 V and an operating pressure of 1.46 Pa.

5.2.3 The power supply

The HiPIMS power supply used here was designed in home and suitable for a rather small size of magnetron. The power supply, referred to as the impulse unit, is basically a unipolar pulse power supply delivering high power pulses to the magnetron. The principle of the impulse unit based on the resistor-capacitor (RC) circuit in which the power is charged up to a bank capacitor and discharged down to the magnetron and an internal resistor. The essential parts in the impulse unit are shown in figure 5.4 including a dc charger, an energy storage capacitor, an insulator gated bipolar transistor (IGBT), an IGBT controller and a TTL pulse generator. The maximum charging voltage applied to the capacitor was -950 V. This charging voltage was used to control an amount of the energy stored in the bank capacitor which in turn control the current and the power delivered to the magnetron. The stored energy in the capacitor was delivered to the magnetron when the IGBT was biased by a TTL pulse either from the built-in signal generator or from the external triggering signal.

An example of voltage V_{dis}, current I_{dis} and power P_{dis} waveforms measured at the target are presented in figure 5.5. The discharge was operated with process parameters of 100 μs pulse width, 100 Hz pulse repetition rate and -600 V charging voltage at 1.46 Pa argon pressure. The discharge voltage and the discharge current were measured using a $\times 100$ voltage probe (Tektronix P5100) and a 10:1 current probe (Tektronix TCP202), respectively. The waveforms were averaged using 32 pulses and recorded by a digital oscilloscope (Tektronix TDS3014). The power waveform was obtained by multiplication between the magnitude of V_{dis} and I_{dis}. Using those process parameters, a number of relevant parameters have been reported in the table below.

Table 5.1: The reported process parameters and a number of relevant parameters obtained from the discharge waveforms V_{dis}, I_{dis} and P_{dis} in figure 5.5.

Parameters	Symbol	Value	Unit
Ar Pressure	p	1.46	Pa
Pulse width	w	100	μs
Pulse repetition rate	f	100	Hz
Charging voltage	U_0	-600	V
Peak current	I_{pk}	31	A
Peak power	P_{pk}	13.4	kW
Peak current density	J_{pk}	0.7	A cm^{-2}
Peak power density	$\mathcal{P}_{\mathrm{pk}}$	0.3	kW cm^{-2}
Energy per pulse	$\langle E_{\mathrm{dis}} \rangle$	1.03	J
Averaged power	$\langle P_{\mathrm{dis}} \rangle$	103	W

Notice that J_{pk} and $\mathcal{P}_{\mathrm{pk}}$ are considered using the total area of the target (A_{tar}) which is approximately 44 cm^2. The initial voltage U_0, in fact, is $V_{\mathrm{dis}}(t)$ at $t = 0$. The energy per pulse $\langle E_{\mathrm{dis}} \rangle$ and average power $\langle P_{\mathrm{dis}} \rangle$ can be obtained from

$$\langle E_{\mathrm{dis}} \rangle = \int_0^w P_{\mathrm{dis}}(t)\, \mathrm{d}t$$

and

$$\langle P_{\mathrm{dis}} \rangle = f \langle E_{\mathrm{dis}} \rangle ,$$

respectively.

5.3 Delay times of current onset

As illustrated by the waveforms in figure 5.5, the HiPIMS discharge can be ignited and stably sustained for the given pulse conditions at a pressure of 1.46 Pa. At this pressure, the discharge current I_{dis} develops shortly after the beginning of the HiPIMS pulse resulting in an negligible delay of the onset of I_{dis}. However, it is not the case for the lower pressure operation. For instance, at the pressure of 0.49 Pa, a significant delay of the I_{dis} onset, denoted as t_{d}, can be observed $\sim 17\,\mu$s later than the beginning

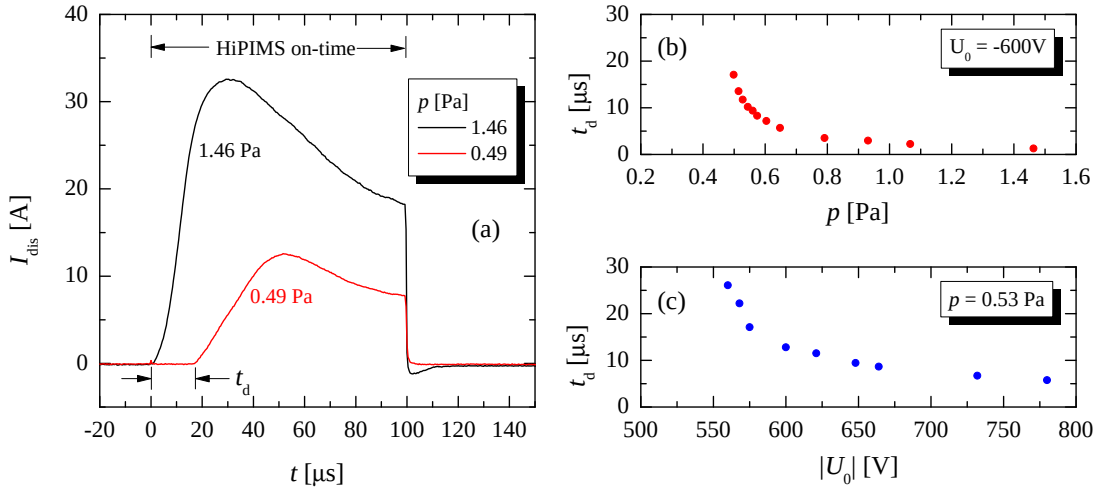

Figure 5.6: (a) Waveforms of discharge current I_{dis} during a typical HiPIMS pulse operated at a pressure p of 1.46 Pa and 0.49 Pa for a charging voltage U_0 of −600 V. Notice that the HiPIMS pulses for both cases were started at $t = 0\,\mu$s. However, the onset of I_{dis} at the lower pressure shows a noticeable delay time t_{d}. (b) The delay time t_{d} as a function of the pressure p for $U_0 = -600$ V. (c) The delay time t_{d} as a function of $|U_0|$ for $p = 0.53$ Pa.

of the HiPIMS voltage pulse, as shown in figure 5.6(a). Notice that the HiPIMS pulses for both cases were applied to the magnetron at $t = 0\,\mu$s. In addition, the delay time t_{d} was longer when the discharge was operated at a pressure lower than 0.49 Pa resulting in an instability and then extinction of the discharge for the selected conditions.

In order to operate the HiPIMS at a pressure lower than 0.49 Pa, it is necessary to decease the delay time t_{d}. One possibility is the use of the charging voltage U_0 larger than −600 V. For example, using U_0 of −800 V, t_{d} was reduced to less than 10 μs, consequently, the minimum pressure to operate the discharge was 0.36 Pa. Kouznetsov *et al.* [2] and Gudmundsson *et al.* [92] have reported that the HiPIMS discharges with a copper and a tantalum target (150 mm in diameter) can be sustained at pressures of about 0.065 Pa using at a rather large U_0 (> 1 kV). However, using U_0 in the order of kilovolt may limit the window of variation in deposition processes at the low pressure operation.

5.4 Pre-ionisation techniques

As suggested by Vašina *et al.* [120,121], a DC pre-ioniser can provide charge particles in the system and accelerate the formation of the HiPIMS plasma, shortly after applying a HiPIMS pulse. The HiPIMS current in the pre-ionisation system can be fully developed within 10 μs using a copper target with U_0 of −1000 V at pressures of 0.7 − 1.4 Pa [120]. The pre-ionisation technique not only accelerates the HiPIMS discharges [120] but also lowers the operating pressure as will be demonstrated in this section.

Here, a commercial negative DC power supply was employed as the DC pre-ioniser.

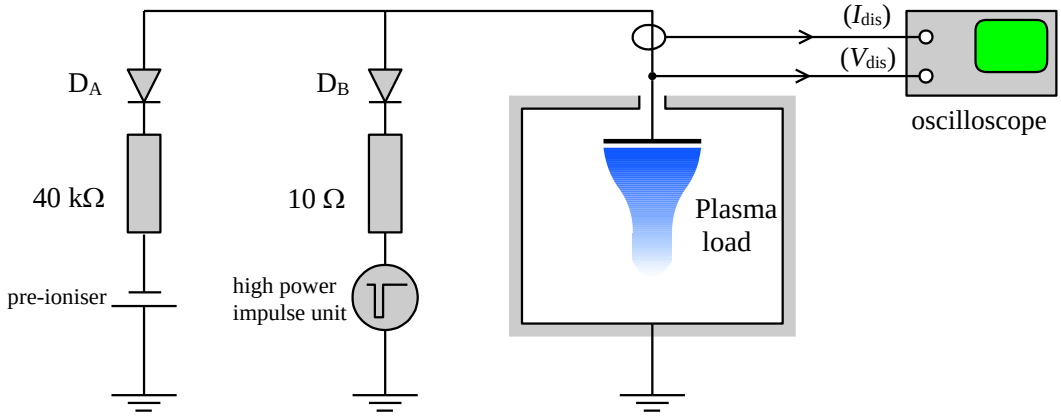

Figure 5.7: The circuit diagram of the power supply for low-pressure HiPIMS discharges.

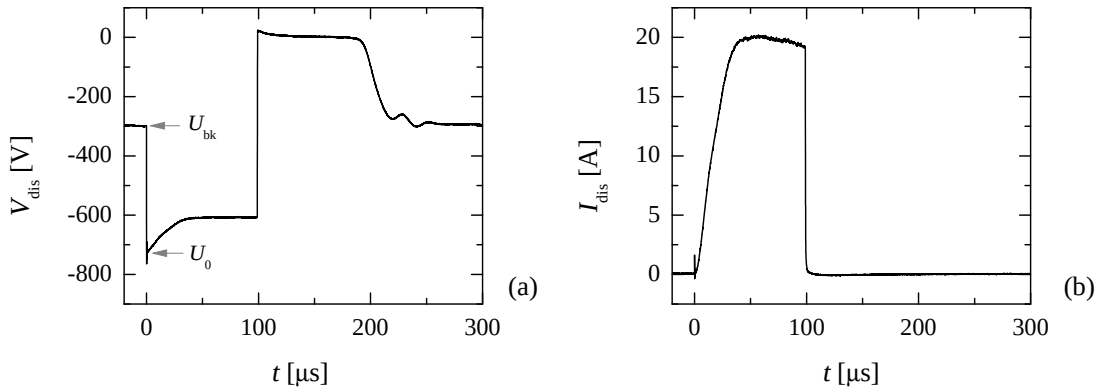

Figure 5.8: Typical voltage (V_{dis}) and current (I_{dis}) waveforms of a pre-ionised HiPIMS discharge. The discharge was operated at an argon pressure of 0.27 Pa.

The power supply was operated in voltage-regulation mode with a fixed output voltage at −1000 V measured when there were no loads. The main function of the pre-ioniser is to provide a background plasma with a sufficient density for which HiPIMS discharges can be developed at low pressures.

The pre-ioniser and the impulse unit were connected in parallel to the magnetron, as shown in figure 5.7. At the output of the impulse unit, a limiting resistor with a resistance of 10 Ω, 500 W was employed in order to protect the IGBT from the over-range of discharge current, see figure 5.7. In addition, a resistor (40 kΩ, 40 W) was also connected at the output of the pre-ioniser in order to keep the current lower than the limit current of the DC power supply (∼ 200 mA).

Since those power units, were connected in parallel, each of power units needs a diode for preventing the back-flow current form each other. In principle, these diodes allows only one of the power units to appear to the magnetron. For example, the voltage of the impulse unit can appear to the target only when the voltage of the impulse unit (in magnitude) is greater than the target voltage supplied by the pre-ioniser.

Typical voltage and current waveforms of the pre-ionised HiPIMS discharge are illustrated in figure 5.8. The discharge was operated at an argon pressure of 0.27 Pa, 100 μs pulse width, 100 Hz repetition rate. Using the voltage waveform in figure 5.8(a), the discharge can be distinguished into three different portions: (1) the background discharge before applying the HiPIMS pulse when $t < 0\,\mu$s, (2) the HiPIMS discharge during the HiPIMS pulse when $t = 0 - 100\,\mu$s and (3) the afterglow discharge during just after the HiPIMS pulse when $t = 100 - 250\,\mu$s. The background discharge is characterised by a sustaining voltage U_{bk} of -300 V and a low current in order of milliamperes supplied by the DC pre-ioniser. Note that to activate the HiPIMS mode, the initial voltage U_0 of HiPIMS pulses supplied from the impulse unit need to be larger (in magnitude) than U_{bk}, e.g. $U_0 \sim -700$ V in this case. During the pulse, the discharge current I_{dis} develops to a peak of 20 A delivered by the impulse power unit. After the termination of the HiPIMS pulse, the discharge is in the afterglow state in which V_{dis} and I_{dis} effectively drop more or less to zero. Finally, the afterglow plasma decays down and transforms to the background discharge when V_{dis} returned to the sustaining voltage.

To better understand the function of the power supplies relating with the discharge waveforms, a simple equivalent circuit shown in figure 5.9 is thus used. The circuit comprised of two power sources, the pre-ioniser and the impulse unit delivering the power to the magnetron via the diode A and the diode B, respectively. The explanation for each state of the voltage waveform are given as follows.

Background discharge: Initially, the impulse unit is inactive and the pre-ioniser is set to -1000 V. At this state, diode B is reverse biased while the diode A is forward biased resulting the voltage of -1000 V appear to the magnetron target. If the operating pressure is sufficiently high, a background discharge is then ignited indicating by a drop

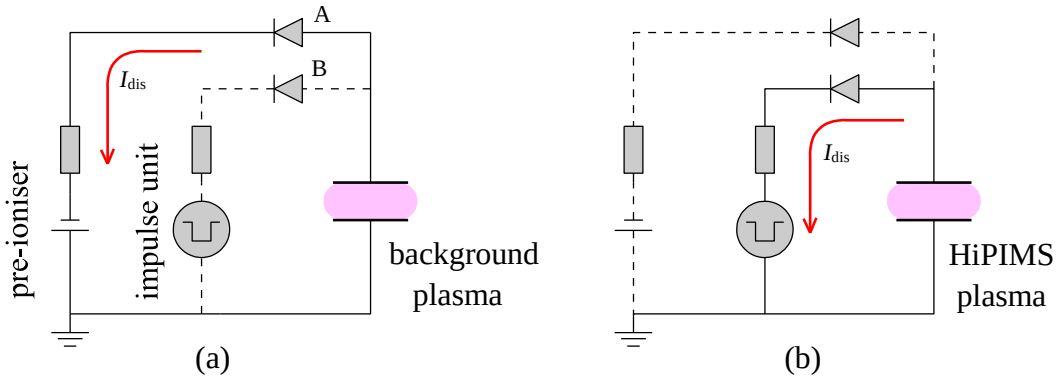

Figure 5.9: Simple equivalent of HiPIMS circuit (a) during the dc background discharge or during the off-time of HiPIMS pulses and (b) during the on-time of HiPIMS pulses. The dashed lines present an inactive path (no current flow) due to the reversing bias of the diode on the circuit path.

of the target voltage from the initial voltage to the sustaining voltage of −300 V with a discharge current of a several tens milliamp. The simple equivalent circuit during the background plasma is shown in figure 5.9(a). The discharge current flows in the outer loop of the circuit through the diode A and the pre-ioniser.

HiPIMS discharge: To activate a HiPIMS discharge, it is necessity to forward bias the diode B and reverse bias the diode A. This condition can occur when the magnitude of the voltage pulses from the impulse unit is higher than that of the sustaining voltage of the background discharge (−300 V). By applying a pulse voltage with a peak of approximately −700 V, the current delivered by the impulse unit can thus be developed as shown in figure 5.8(b). Note that during the HiPIMS discharge condition, I_{dis} flows in the inner loop of the circuit via the diode B and the impulse unit (see figure 5.9(b)).

Afterglow discharge: At the termination of the HiPIMS pulse, the bias status of those diodes are switched back to the initial state, i.e. the diode B is reversed and the diode A is forward. It implies that the discharge current is determined from the outer loop of the circuit (see figure 5.9(a)). The immediate return of V_{dis} to the sustaining voltage (−300 V) can be expected for a resistive load with a fixed resistance. However, it is not the case for the pulsed plasma load in which its impedance is highly dynamic. The voltage measured across the magnetron drops straight-away close to zero for a certain time before turning back to the sustaining voltage. This dropping of V_{dis} can be explained by the following paragraph.

As suggested from the probe measurements in the Chapter 4, the plasma does not immediately extinguish at the pulse termination. Rather, it gradually decays with a certain rate. This remnant of the plasma is often referred to as an afterglow plasma. The afterglow plasma presents a low impedance load, for example, a few tens of Ohm at the pulse termination. The impedance of the afterglow plasma is relatively low compared to the limiting resistor 40 kΩ connecting to the pre-ioniser circuit. Using the principle of voltage divider, the voltage across the plasma load is thus less than 0.1% of the output voltage of the pre-ioniser (-1000 V). Until the impedance of the afterglow plasma increases to the same order of 40 kΩ, the voltage across the magnetron thus gradually changes and returns to the sustaining voltage of −300 V. The afterglow plasma is then transformed to the background plasma providing the condition for the next HiPIMS pulse to be developed.

5.5 Plasma characterisations

In this section, the very low pressure HiPIMS plasma is characterised using a Langmuir probe and an energy-resolved mass spectrometer. The Langmuir probe was located on the discharge axis 100 mm away from the target surface. The probe consisted of a

tungsten wire with a radius r_p of 0.05 mm and a length l_p of 4.4 mm. The probe acquisition system as described in Chapter 3 was employed for time-resolved measurements. The *I-V* probe characteristics were averaged over five sweeps, with a range of probe bias voltage from −95 to +20 V. In addition, the probe measurements were performed over the full pulse cycle to obtain a complete picture of the evolution of the very low pressure HiPIMS discharge.

The mass spectrometer (EQP300; Hiden Analytical Ltd.) was used to investigate the time-averaged ion mass spectra and the ion energy distribution functions for selected ion species. The EQP consists of an ion extractor, a 45° energy filter, and a quadrupole mass filter as well as an ion-counting secondary electron multiplier. The extractor head of the EQP was equipped with a 100 μm diameter grounded orifice which faced directly to the target surface; hence, ions moving perpendicularly to the target surface were observed. To obtain ion mass spectra, the mass/charge was scanned from 0.4 to 60 amu/charge, with steps of 0.1 amu/charge at an ion energy of 0.5 eV. The discriminating voltage in the energy filter section was scanned between −10 and +20 V, with steps of 0.1 V. Assuming a similar behaviour of different isotopes [60, 123], the isotope with the highest value of abundance for each ionic species was measured and presented here. In order to obtain the highest signal, the parameters of the spectrometer were optimized before performing the measurements. The ion extractor was set at a voltage of −20 V, while the electrostatic lens in the ion extractor head was adjusted to be −185 V. These settings were used for all selected ionic species. The measurements were carried out at the same position as the Langmuir probe but not simultaneously done. The process parameters for the investigation was summarised in table below.

Table 5.2: The selected process parameters for the plasma investigation.

Parameters	Symbol	Value	Unit
Ar Pressure	p	0.08	Pa
Pulse width	τ_{pl}	100	μs
Pulse repetition rate	f_{pl}	100	Hz
Charging voltage	U_0	−800	V
Peak current	I_{pk}	20	A
Energy per pulse	$\langle E_{dis} \rangle$	0.95	J
Averaged power	$\langle P_{dis} \rangle$	95	W

5.5.1 Evolution of the plasma parameters

The evolution of the plasma parameters including energy contour from EEDFs, the electron density n_e, the effective electron temperature T_{eff}, plasma potential Φ and floating potential V_f of the pre-ionised HiPIMS discharge is shown in figure 5.10. Note that n_e and T_{eff} were calculated from the EEDF using equation 3.6 and equation 3.7, respectively.

During the first 10 μs after the pulse initiation ($t = 0\,\mu$s), the discharge is characterized by a large V_{dis} of -800 V and a low I_{dis} of less than 100 mA. The plasma parameters at this time are basically the same with that from the background plasma having the electron density of $\sim 3 \times 10^{15}\,\mathrm{m}^{-3}$. When the time progresses, the T_{eff} shows considerably high values of ~ 15 eV. The high value of T_{eff} also corresponds to the extension of the energetic tail of the EEDF in which the energy of up to ~ 50 eV can be observed. During the initial state of the HiPIMS pulse ($t \sim 0-20\,\mu$s), the sheath expands due to the growing negative target voltage while the electron density remains constant. Thus, more positive ions which are present in the sheath due to the pre-ionisation are accelerated towards the cathode. Impinging ions will then cause secondary electrons to be emitted from the target surface, gaining kinetic energy up to the equivalent of the cathode potential. This can create beam-like electrons which give rise to high effective electron temperatures during the first 5 μs after the high voltage initiation. The existence of beam-like electrons causes a very highly negative V_{f} less than -95 V.

The high-energy electrons created in this stage are important in the electron impact ionisation mechanism to generate the dense plasma during the HiPIMS pulse. The plasma density increases by ~ 3 orders of magnitude within the next 30 μs. At the same time, the discharge current rises considerably from less than 100 mA to about 20 A. During the transition from the low current to the high current discharge, T_{eff} decreases from its peak (15 eV) to 3 – 4 eV. The decrease of T_{eff} can be attributed to the dramatic increase of the plasma density in the ionisation volume. Also, the electron cooling during $t \sim 20 - 40\,\mu$s is consistent with the depletion of the energetic tail of the EEDF.

The decrease in T_{eff} is accompanied by the variation of other plasma parameters. For instance, the floating potential, V_{f}, is elevated from a very deep negative value (> -95 V) to -20 V. The plasma potential, Φ, decreases from the initial value of 5 V to a negative value of about -2.5 V at $t \sim 25\,\mu$s and then returns to a positive value of about 3 V. The electron density, n_{e}, increases to $\sim 2 \times 10^{17}\,\mathrm{m}^{-3}$ forming a dense plasma. All plasma parameters remain at relative stable values for the rest of the pulse. The stability of the plasma parameters may be attributed to the stability of the V_{dis} and I_{dis} waveforms generated by the impulse unit.

At the end of the HiPIMS pulse, V_{dis} and I_{dis} immediately fall to almost zero due to the low impedance of the afterglow plasma when compared with the limiting resistor of the pre-ionizer power supply. The voltage V_{dis} still stays at the low level for the next 50 μs (after the pulse termination) while the density of the afterglow plasma decays by ~ 1 orders of magnitude to a value of about $1 \times 10^{16}\,\mathrm{m}^{-3}$, as shown in figure 5.11. The decay in n_{e} is accompanied by new values of the electron temperature, the floating and the plasma potential. For example, T_{eff}, Φ and V_{f} change to 0.6 eV, 0.9 V and -1 V, respectively, at $t \sim 150\,\mu$s.

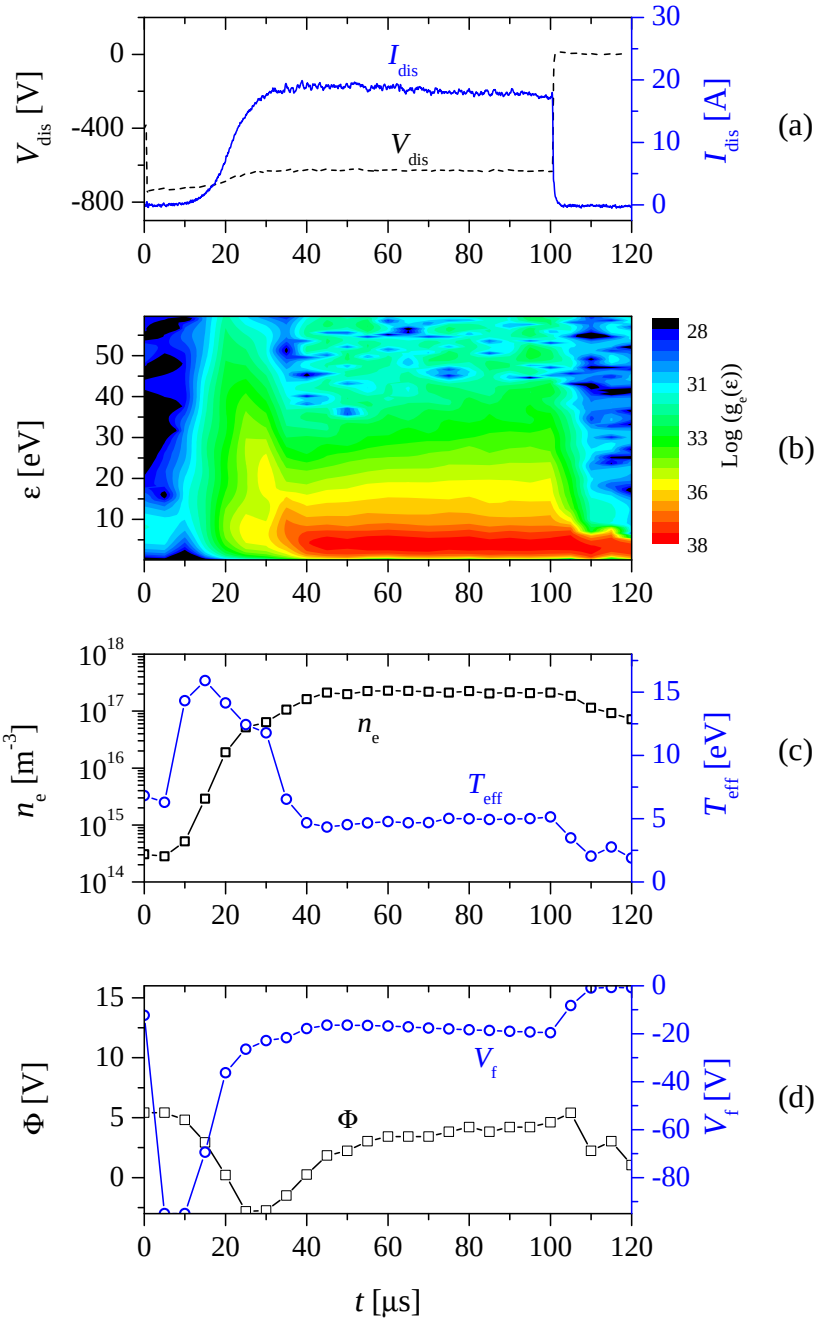

Figure 5.10: (a) the voltage V_{dis} and current I_{dis} waveforms, (b) contour plot of electron energy ε, (c) the electron energy n_{e} and the effective electron temperature T_{eff} and (d) the plasma potential Φ and floating potential V_{f} of the pre-ionised HiPIMS discharge operated with the process parameter in the Table 5.2.

During $t \sim 200-500\,\mu$s, all plasma parameters remain at the same value as those shortly after the termination except for n_{e} which decays ~ 1 order. At the same time, V_{dis} gradually returns to the DC background voltage of -400 V. It is worth noting, a peak of n_{e} during the off-time for the very low pressure operating can not be observed, which is consistent with the work of Vetushka and Ehiasarian [90] for Cr and Ti target

at a pressure of 0.28 Pa.

When $t > 500\,\mu$s, the afterglow plasma gradually transforms to the background plasma. All plasma parameters change to background values, for example, $\Phi \sim 2$ V, $V_f \sim -12$ V, $T_{eff} \sim 3$ eV and $n_e \sim 2 \times 10^{14}\,m^{-3}$. These background values will become the initial values for the next pulse of HiPIMS.

5.5.2 IMS and IEDF

In this section, time-averaged mass/charge spectra and energy distribution of ions in the HiPIMS discharge operated at a pressure (p) of 0.08 Pa and 0.53 Pa are presented and compared.

Time-averaged mass/charge spectrum and IEDF of Ar^+ during the background plasma at $p = 0.08$ Pa are plotted in figure 5.12. The spectrum for the background plasma contains only ions from the sputtering gas Ar^+, Ar^{2+} and their isotopes as well as a very small amount of H^+ coming from the vacuum system. It is clear that the background plasma itself cannot significantly produce any ions of the sputtered species due to the very low power used during the operation. The energy distribution of Ar^+

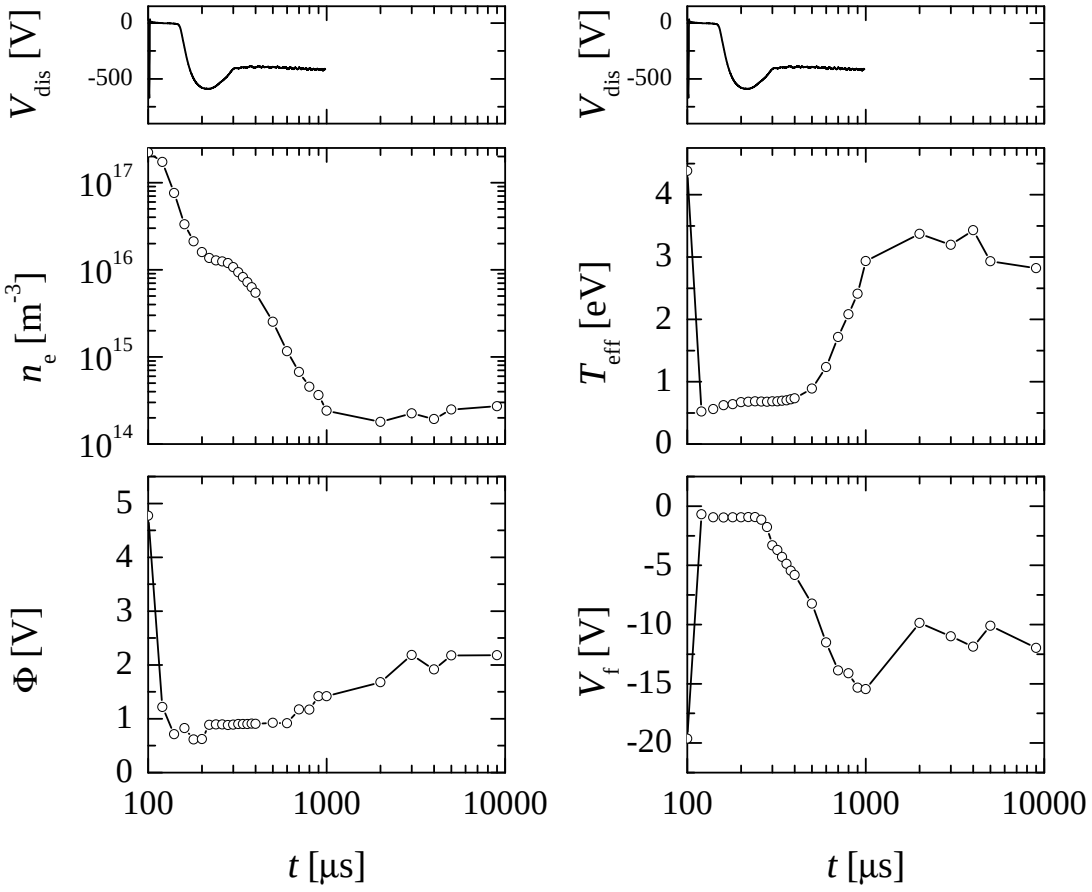

Figure 5.11: Temporal plasma parameters and the voltage waveform during off-time phase of the low-pressure HiPIMS plasma. The plasma parameters include the electron density, n_e; the effective electron temperature, T_{eff}; the plasma potential, Φ; and the floating potentila,V_f.

ion in the plasma shows a single peak at energy close to zero with an energetic tail extended to only 5 eV.

By applying the HiPIMS pulse, the ions of the sputtered species, including Ti^+ and Ti^{2+} can be observed for both operating pressures, as shown in figure 5.13. However, a small number of Ti^{3+} and Ti^{4+} ions can additionally be detected for the low pressure operation. The observation of highly charged titanium ions has been reported for a HiPIMS discharge at operating pressure 0.6 Pa with a high peak power density of 2.9 $kWcm^{-2}$ [124]. The authors [124] also listed several requirements for the occurrence of multiply charged ions, which partly involve material properties (ionisation energy and self-sputtering yield of the target material) and the power supply (high power density, long pulse on-time and maintenance of a high current at an almost constant voltage). According to the spectrum in figure 5.13(a), one can argue that the operating pressure may be added as an influencing parameter to generate the highly charged ions, i.e. lower pressure benefits the occurrence of multiply charged ions of the sputtered material.

Figure 5.14 shows the time-averaged IEDFs of the main species Ar^+, Ti^+, Ti^{2+} ions in the HiPIMS the pressures of 0.08 Pa and 0.53 Pa. The IEDF of Ar^+ shows a significant fraction of ions with an energy tail up to 15 eV. The tail in IEDF of Ar^+ may be caused by a momentum and energy transfer from the sputtered particles [63]. One should note that the horizontal axis in the IEDF plots is not the energy but the effective stopping potential. This means that the absolute energy for Ti^{2+} is found by multiplying the effective stopping potential by 2, i.e., their energies up to 40 eV can be achieved. The IEDF of metal ionic species in the HiPIMS exhibits a low energy peak at about 2 – 3 eV with a high energy tail that can be followed to around 20 eV. The low energy peak may be the results of thermalized ions diffusing through the plasma sheath while the energetic tail may originate mainly from sputtered atoms ionised in

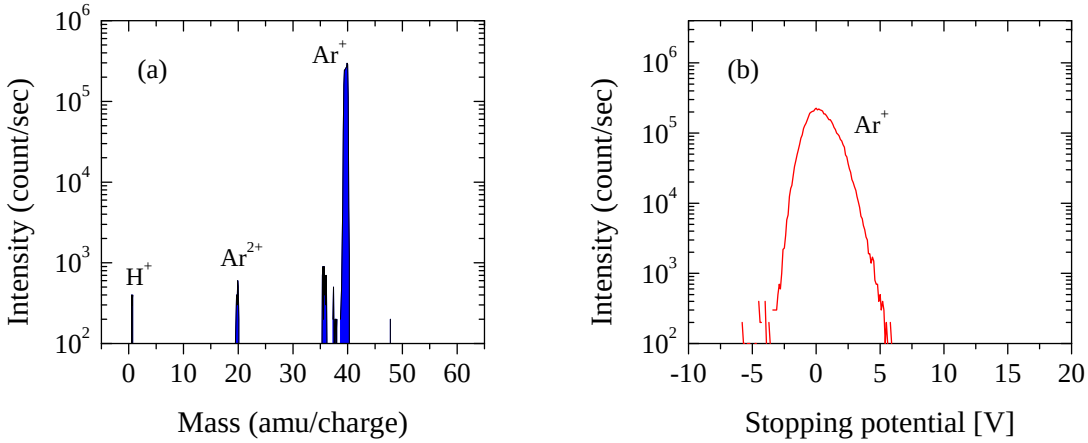

Figure 5.12: (a) Ion mass spectrum and (b) energy distribution of Ar^+ during the background discharge at p=0.08 Pa.

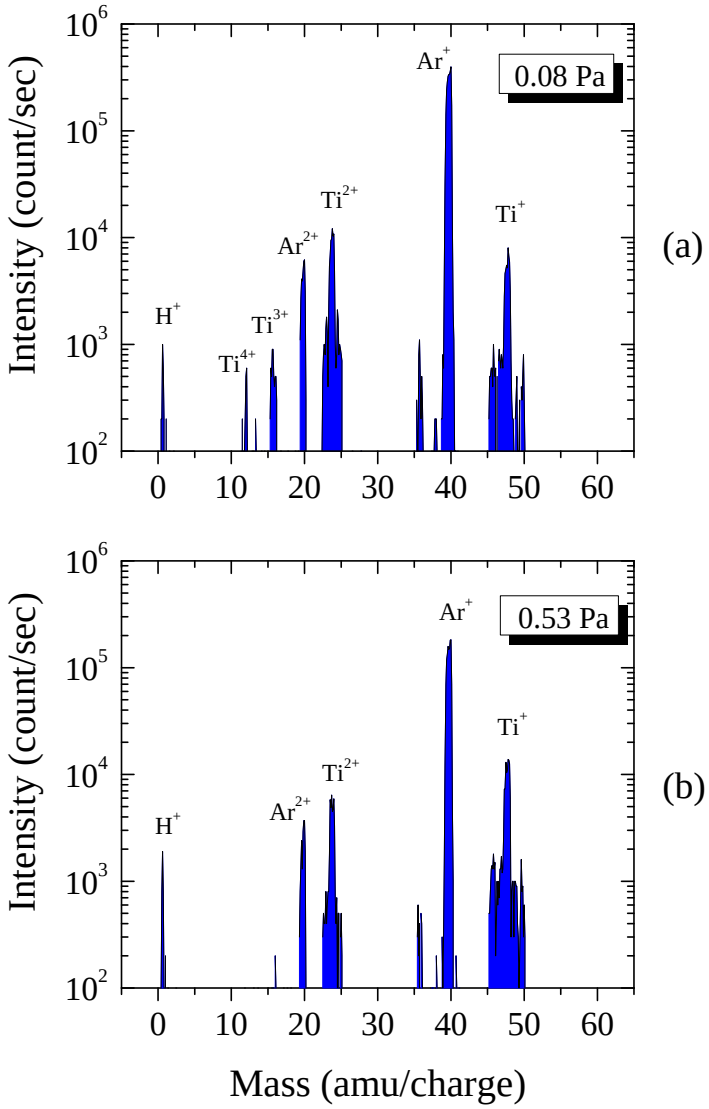

Figure 5.13: The mass spectra at the recorded energy of 0.5 eV for the HiPIMS at the operating pressure of (a) 0.08 Pa and (b) 0.53 Pa.

the torus region before entering the analyser [63].

The most striking feature of the low pressure operation is the fact that flux Ti^{2+} is higher than that of Ti^{+}. This is in contrast to the operation with the typical pressure of between 0.2 and 0.6 Pa where the flux fraction of singly charged metal ions is usually larger than the one of doubly charged ions [60, 123, 125–127]. The relative high flux fraction of Ti^{2+} can be explained by considering the large mean free path at low pressure compared with the higher pressure. That causes an increase of the probability of the high energetic species reaching the mass spectrometer without any collision with the background gas. In addition, the increase of the content of Ti^{2+} ions may also be explained by an increase in the electron temperature. Gudmundsson *et al.* reported in [55] that the EEDF is broader, i.e., a large population in energetic electrons is

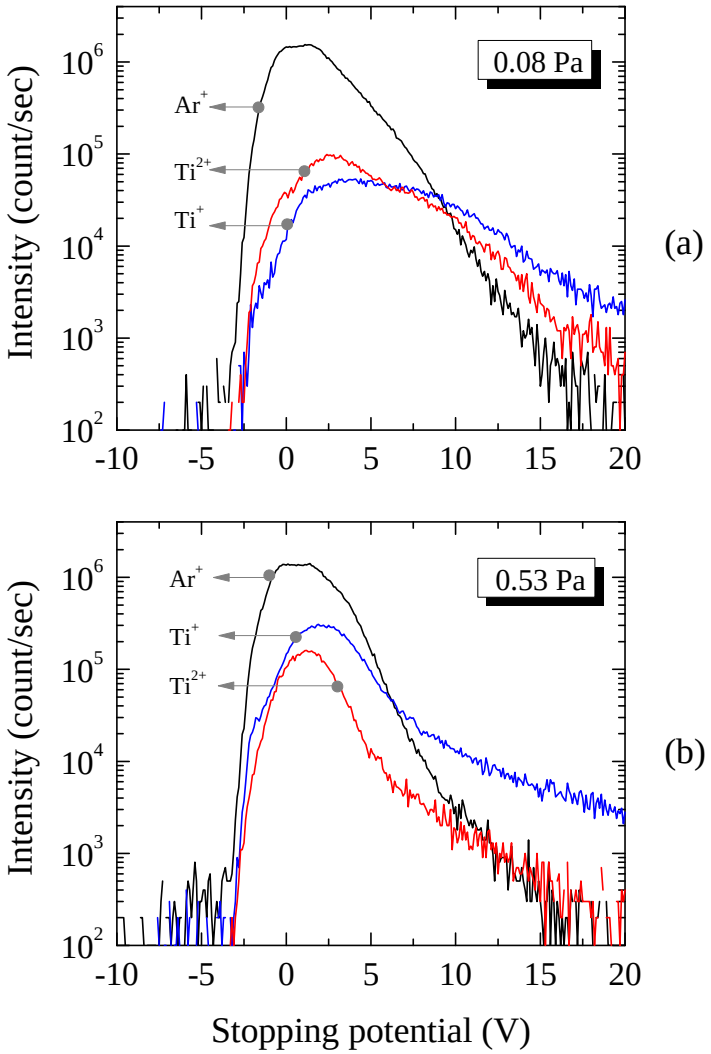

Figure 5.14: The energy distribution function of Ar^+, Ti^+, Ti^{2+} ions during the HiPIMS plasmas operated at the operating pressures (a) 0.08 Pa and (b) 0.53 Pa. It should be noted that the horizontal axis of the plots is shown in term of stopping potentials, i.e. the stopping potentials need to be multiplied by 2 to obtain the actual energy of doubly charged ions.

present in the plasma volume when operating at lower pressure.

Although low pressure operation with collision-free, high energy particle bombardment at the substrate is clearly possible as demonstrated here through the use of a pre-ioniser in HiPIMS pulsing, the bombardment of growing films with the excessive-energy ions can lead to undesired high compressive stresses [128]. The spatial distribution of metal ion fluxes may be more uniform throughout the vessel for the low pressure conditions as suggested in the work of Hecimovic and Ehiasarian [129].

5.6 Conclusions

The HiPIMS discharge assisted by a pre-ionised DC plasma can be stably operated at low pressures of less than 0.13 Pa with a low sputtering yield target. The DC

background plasma created by the pre-ioniser can reduce the HiPIMS plasma ignition delay time to less than 5 μs while the standard HiPIMS (without the assistance of the pre-ionizer) at these low-pressures cannot be ignited within the selected pulse width of 100 μs in the same operating pressure. It was concluded from the time-resolved probe measurements that a plasma with a high density of $2 \times 10^{17}\,\mathrm{m}^{-3}$ and with an effective electron temperature of 5 eV can be created at the lowest pressure of 0.08 Pa. The mass and energy distribution measurements showed an increase both in the density of high-order ionic species and in the average energy at the lowest pressure which is mainly due to the long mean free path and low frequency of collision with the background gas. Furthermore, the presence of energetic multiply ionised sputtered particles was observed and these may be beneficial in carrying momentum to the substrate so aiding in the intensification of the growing film.

Chapter 6

Ion velocity distribution functions

6.1 Background

A number of studies have shown that structures and properties of growing films can be adjusted using ion bombardment during the film growth. For instance, a void-free structure, fine grain size and smooth surface of dense CrN films with high hardness, high abrasive wear resistance and good adhesion can be achieved by energetic bombarding of the high-density metal ions during reactive HiPIMS processes [28,34,130]. Furthermore, the phase structure of thin films can be controlled by tuning the ion energy via the substrate biasing technique. For example, the Ta film with a BCC structure which is normally formed in the Ta bulk but not in Ta film deposition can be obtained in HiPIMS plasma by applying the bias voltage of -70 V to the Si substrate [131]. Measurements of the energy and flux of ions during HiPIMS processes are of essentially importance to the reproducibility of high-quality films.

Time-averaged and, in particular, time-resolved ion composition and ion energy distribution function (IEDF) in non-reactive and reactive HiPIMS plasmas have been extensively studied by a number of research groups using conventional energy-resolved mass spectrometry. Bohlmark *et al.* [60] have reported the large contribution of Ti^+ flux in the off-normal direction during HiPIMS discharge whereas Kudláček *et al.* [123] argued that Ar^+ dominates the plasma when IEDFs have been measured in the line of sight direction. The remarkably radial travelling of metal ions has been explained by the cross-field type of charged particle transport by Lundin *et al.* [53] leading to a number of efforts for coating high performance films in the sideways direction [132,133]. Greczynski and Hultman [64] argued that in time-resolved measurements, ions from the sputtering gas initially dominate the plasma composition before diminishing due to gas rarefaction with the emergence of intense metal ions as a consequence. The energy distribution of metal ions in the discharge normally consists of a high-density low-energy peak at a few electron volts and a weak energetic tail with energies of higher than 50

V. Hecimovic *et al.* [63] reported that the peak in IEDF, belonging to the thermalized metal ions, is maintained by the plasma sheath covering above the electrically grounded aperture of the spectrometer, however the high energy tail mainly originates from post-ionized sputtered species travelling directly from the target which are governed by the Sigmund and Thompson distribution. The time-resolved IEDF measurements with a 20 μs time-resolution, carried out by Hecimovic and Ehiasarian [61], revealed that the energetic tail of energy up to $\sim$70 V for singly charged chromium ions develops during the on-time phase. After the pulse termination, the energetic tail of Cr^+ slightly decays for a few hundreds of microseconds before leaving only a low-energy peak for a few microseconds. In the reactive mode, where the reactive gases such as nitrogen are introduced to the HiPIMS processes, the energetic tail for all ionic species including metal, noble and reactive ions increases as a function of the reactive gas flow due to increasing the peak current which is the result of target poisoning [64, 127].

In spite of the comprehensive investigations on the dynamic of IEDFs at a typical substrate position, the studies of spatial and, particularly, angular distributions of ion energy in HiPIMS plasmas have been restricted by the intricate arrangement of the mass spectrometer. The mass spectrometer is a potential diagnostic tool that can distinguish mass and ion species. Due to the size of the spectrometer, however, it is not practical to perform spatial-resolved IEDF measurements, which are important to understand the dynamics of ions in HiPIMS discharges.

The retarding field analyser (RFA) is an energy analyser which has typically been used to determine the velocity distribution of ions bombarding a grounded or biased substrate immersed in DC [69], RF [70,71,74] and pulsed plasmas [76,77] for depositing and etching applications. The RFA is a compact, manoeuvrable device that is suitable to perform spatial measurements. Furthermore, by operating in the normal mode as described in Chapter 4, time-resolved IEDF measurements are possible with the acquisition system that has been employed in the previous chapter for the Langmuir probe experiments.

The detail of the performance of the RFA is given in this chapter. The performance of the RFA is validated by a commercial energy-resolved mass spectrometer and a Langmuir probe. The HiPIMS plasma under a number of process conditions are then investigated using the validated RFA.

6.2 Experimental arrangement

The experiments were carried out in the HiPIMS system described in Section 5.2. A plate of titanium target (99.99% purity, 75 mm diameter, 6 mm thickness) was fitted to the circular unbalanced magnetron source. The magnetron was located in the cylindrical vacuum chamber in which a base pressure of about 6×10^{-4} Pa was established by the turbo molecular pump backed by the rotary pump. Argon gas was

introduced close to the magnetron and regulated by the mass flow controller with flow rates of between 0.7 and 4.0 sccm to establish operating pressures in the low-range of 0.13 – 0.53 Pa measured by the capacitance pressure gauge.

In order to stabilise HiPIMS plasmas at the low pressure regime, the technique of pre-ionisation was employed by applying an auxiliary (simmer) dc power supply in parallel with the home-built HiPIMS power supply. The detail of the pre-ionised HiPIMS power supply was given in Section 5.2. The example of voltage (V_{dis}) and current (I_{dis}) of the discharge is demonstrated in figure 6.1. The discharge was operated with the process conditions of 0.13 Pa Ar pressure, 100 Hz pulse repetition rate, 100 μs pulse width and $\sim$ 20 A peak current. All experiments in this chapter were performed with these selected conditions, unless stated otherwise.

A diagram of the experimental arrangement is shown in figure 6.2. The titanium target and the RFA are set in a Cartesian coordinate system (x, y, z). The target surface was placed on xy-plane at $z = 0$ at which the target centre was located at the origin of the coordinate system. As mentioned in the Chapter 3, the RFA is able to move along and rotate around a feedthrough axis allowing the change the location and orientation of the RFA during the discharge without venting the vacuum system.

The experiments in the present chapter were divided into three parts i.e. optimisation, validation and utilisation of the RFA in the HiPIMS discharge. In the first part, the RFA was optimised by tuning the voltage at the electron repelling grid to obtain the maximum reading of ion current at the collector. In the second part, the performance of the optimised RFA was validated with a variety of standard diagnos-

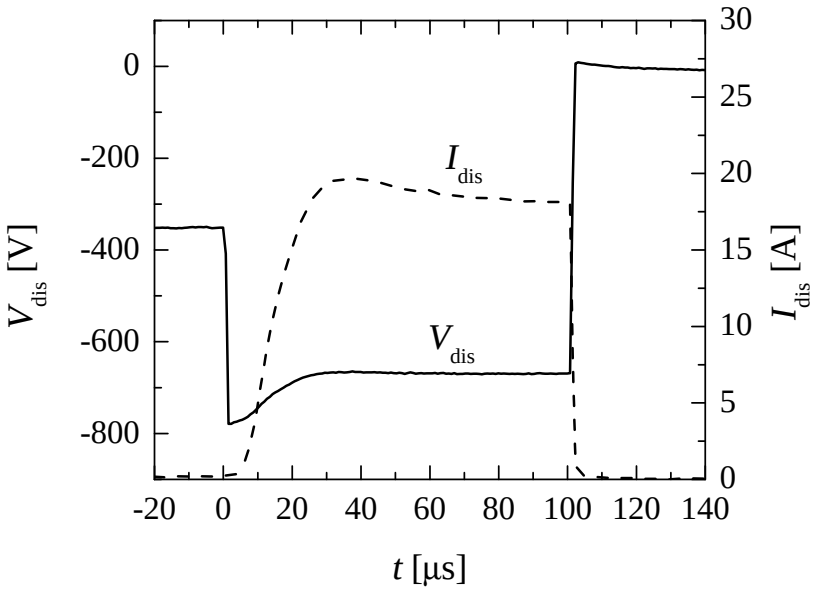

Figure 6.1: Waveforms of discharge voltage V_{dis} and current I_{dis} for the pre-ionized HiPIMS discharge with the selected process conditions: a repetition rate of 100 Hz, a pulse width of 100 μs and a peak current of 20 A at argon pressure of 0.13 Pa.

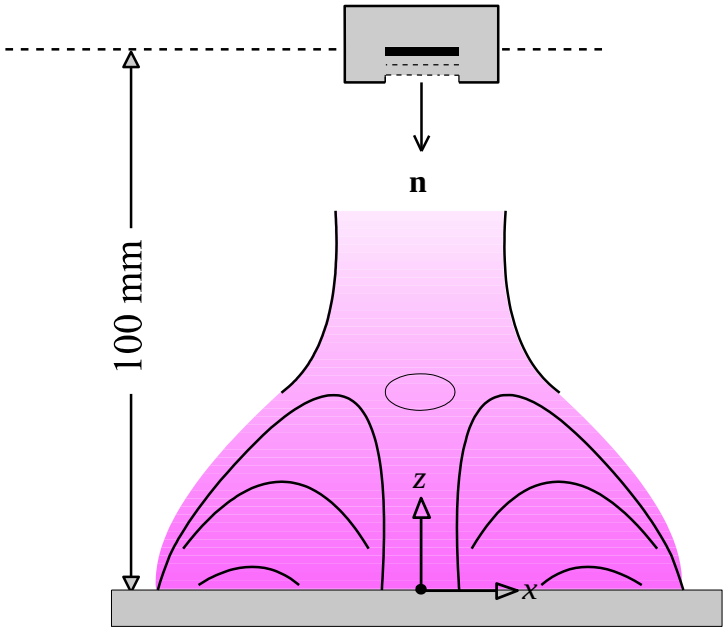

Figure 6.2: A diagram showing the RFA arrangements for time-resolved IEDF measurements. The target surface was placed on xy-plane at $z = 0$ and the RFA is located at on discharge axis 100 mm away from the target surface.

tic tools including an energy-resolved mass spectrometer (MS) and a Langmuir probe. The energy-resolved mass spectrometer was used to compare the shape of IEDF. The Langmuir probe was employed to compare the plasma potential and the peak position of IEDF obtained from the RFA. In the third part, the validated RFA was utilised to measure the time-resolved IEDFs, the average energy and the flux of ions in the HiPIMS discharge.

During the optimisation and validation, the RFA and the standard tools were located at a typical substrate position of (0, 0, 100 mm). In addition, these diagnostics tools were oriented to face directly to the target surface. During the time-resolved measurements, the RFA was in the similar location and orientation with the previous conditions . The IEDFs and Γ_i were measured using the validated RFA at $t = 0\,\mu$s to $120\,\mu$s after the pulse initiation with steps of $5\,\mu$s.

6.3 Optimisation of the RFA

In this section, the two-gridded RFA was optimised by tuning the voltage at the electron repelling grid in order to obtain the maximum signal of the collector current.

Figure 6.3(a) presents the collector current I_c as a function of the discriminating voltage V_d for a number of the electron repelling voltages V_r. The measurements were obtained during the on-time phase of HiPIMS pulses at $t = 80\,\mu$s after the pulse

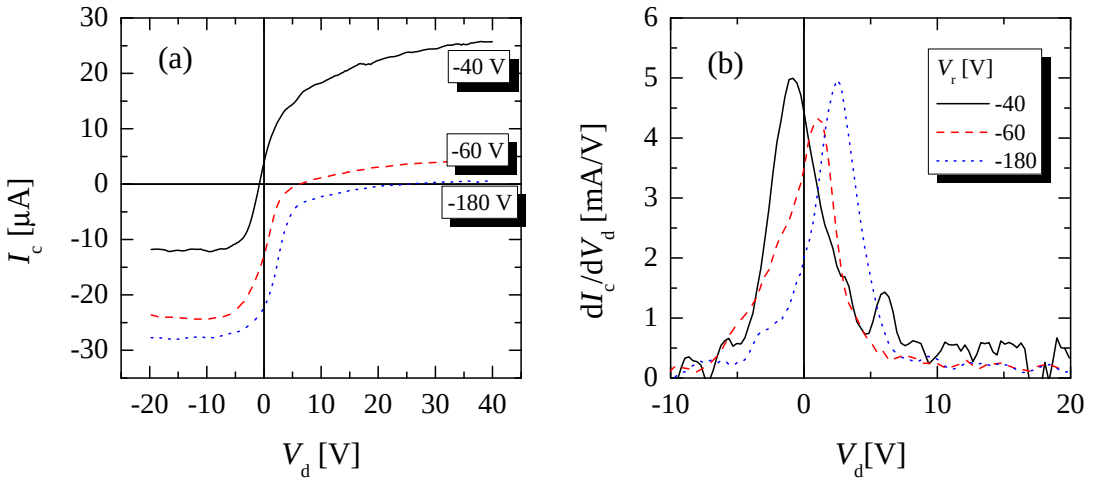

Figure 6.3: (a) The collector current I_c as a function of the discriminating voltage V_d of the RFA and (b) the dI_c/dV_d for a number of repelling voltage V_r. Note that the data were obtained at $t = 80\,\mu$s.

initiation. It is worth mentioning again that the collector current is negative when the flux at the collector is dominated by ions, i.e., $I_i > I_e$. For $V_r = -40\,$V, there is a considerable positive current in the I-V curve, e.g., $I_c \sim 25\,\mu$A at $V_d = 30\,$V. This indicates that a significant amount of electrons with energy greater than $\sim eV_r$ (40 eV) is able to reach the collector and make a contribution to I_c. An increase in V_r to $-60\,$V and then $-180\,$V can significantly reduce the contribution of these energetic electrons as the positive portion of I_c decreases down to a few microamps (e.g. $I_c \sim 1\,\mu$A at $V_d = 30\,$V for $V_r = -180$V̇).

The first derivatives dI_c/dV_d of the I-V curves plotted against V_d are shown in figure 6.3(b). For $V_r = -40\,$V, when the electron contribution is large, V_d at the peak of dI_c/dV_d is negative. The V_d at the peak of dI_c/dV_d changes to a more positive value using a more negative V_r. For example, the position of the peak of dI_c/dV_d is 2.5 V in V_d for $V_r = -180\,$V.

Obviously, the electron repelling voltage V_r has a direct influence on the I-V curves which in turn alters the dI_c/dV_d graphs. Using a high value of V_r is preferred to remove the contribution of electrons at the collector and then to obtain the corrected I-V curves. However, an excessive high V_r may causes undesired consequences. For example, the excessive V_r can create a high electric field at the region between the grid G and R (see figure 3.6). This high electric field can penetrate out and affect the trajectory of the ions arriving to the grid G. The effect of the field penetration from a high to a low electric field strength is known as the electrostatic lens effect [71]. Moreover, a strong electric field may induce arcing and, hence, permanently destroy the delicate grids. It is therefore necessary to optimise the voltage applied to the electron repelling grid.

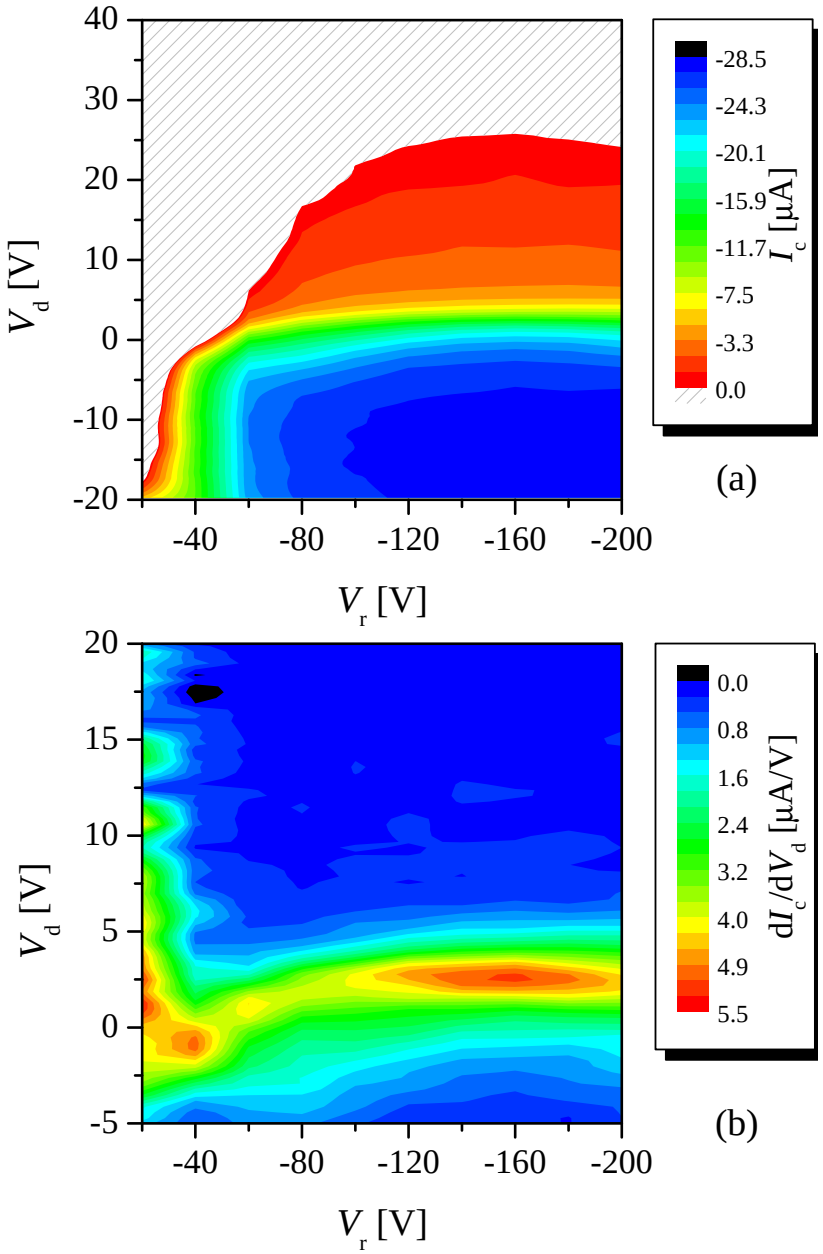

Figure 6.4: Contour plots of (a) the collector current I_c and (b) the first derivative dI_c/dV_d on the plane of the discriminating voltage V_d and the electron repelling voltage V_r. The patterned region in the contour plot of the I_c indicates the positive portion of the I_c, i.e. $I_c > 0$. The value of V_r for the optimum conditions, at which the minimum of the positive potion of I_c is accompanies by the maximum of dI_c/dV_d, is found to be $\sim -160\,\mathrm{V}$

In order to search the optimum point of operation of the RFA, V_r was thus scanned from -20 to $-200\,\mathrm{V}$ with steps of $20\,\mathrm{V}$. The contour plots of I_c and dI_c/dV_d on the plane of V_d and V_r are shown in figure 6.4. In figure 6.4(a) only the negative portion of I_c, i.e. the portion of ion dominated current, is presented in the contour. In general, the ion dominated portion substantially increases with V_r increases from $-20\,\mathrm{V}$ to

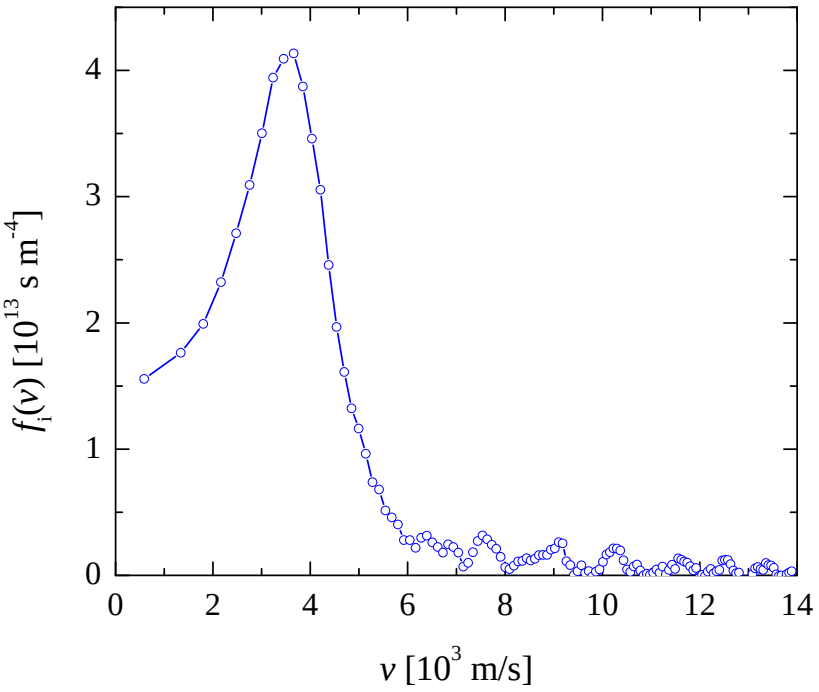

Figure 6.5: A plot of ion velocity distribution function (IVDF) obtained from the optimised RFA with $V_r = -160\,V$.

$-120\,V$. Using $V_r < -120\,V$, the peak position of dI_c/dV_d becomes more stable (see figure 6.4(b)). However, biasing the repelling grid at $V_r = -200$ V causes a noticeable decrease of the ion portion of I_c and decrease of amplitude of the dI_c/dV_d peak. The optimum condition could thus be met when the ion portion of I_c and the peak of dI_c/dV_d reach the maximum. In this case, the optimum condition occurs at $V_r \sim -160\,V$ for the given discharge conditions.

Using the equation 3.8, the ion velocity distribution function (IVDF) obtained from the optimised RFA is presented in figure 6.5. In the IVDF plot, the distribution function for singly charged ions, denoted by $f_i(v)$ on the y-axis, is plotted against the velocity $v = \sqrt{2eV_d/M_i}$ on the x-axis. The function $f_i(v)$ is used to present the number of ions per unit volume that are travelling perpendicular to the RFA with a velocity

Table 6.1: A summary of the fundamental properties on the sampling ions obtained from the IVDF in figure 6.5. Notice that $v_{i,most}$ is the velocity at the peak position of the $f_i(v)$ curve.

Ion properties	Symbol	Value	Unit	Equation
Density	n_i	1.3×10^{17}	m^{-3}	3.10
Most probable velocity	$v_{i,most}$	3.6×10^3	$m\,s^{-1}$	
Mean velocity	$\langle v_i \rangle$	3.4×10^3	$m\,s^{-1}$	3.11
Mean square velocity	$\langle v_i^2 \rangle$	1.5×10^7	$m^2\,s^{-2}$	3.12
Flux	Γ_i	4.4×10^{20}	$m^{-2}\,s^{-1}$	3.13
Energy	E_i	3.2	eV	3.14
Energy density	Ψ_i	4.1×10^{17}	$eV\,m^{-3}$	3.15

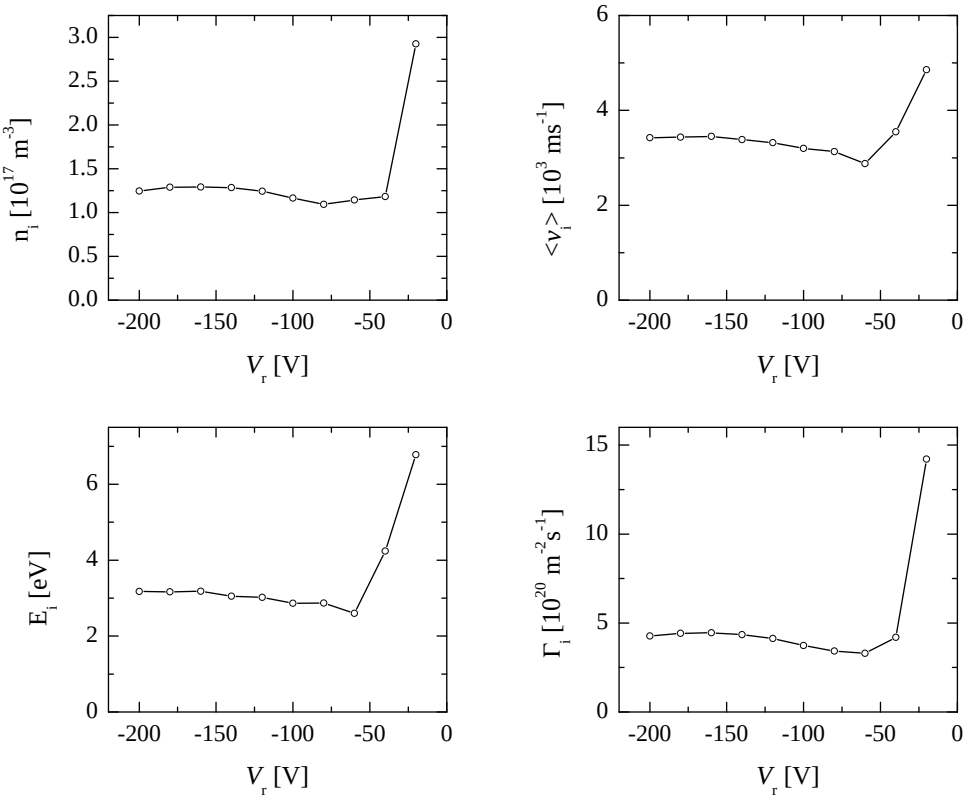

Figure 6.6: Plots of ion parameters including n_i, $\langle v_\mathrm{i}\rangle$, E_i and Γ_i, calculated from IVDF for a number of V_r.

between v and $v + \mathrm{d}v$. Using the function $f_\mathrm{i}(v)$, fundamental properties of the sampled ions are thus extracted as summarised in Table 6.1.

From the viewpoint of optimisation, V_r need to be scanned if any process conditions are changed. This is not suitable especially for time-resolved measurements. The acquisition time to obtain an I-V curve may be longer than 1 minute due to the relative low repetition rate (100 Hz) of the HiPIMS discharge. Using an estimated V_r, surrounding the optimum point, the calculated ion parameters may be applicable with an acceptable uncertainty. Figure 6.6 shows plots of selected ion parameters against V_r calculated from I-V curves in figure 6.4. When V_r is less than -75 V, the selected ion properties including n_i, $\langle v_\mathrm{i}\rangle$, E_i and Γ_i are very near to their optimum values within 20% uncertainty. For example, using $V_\mathrm{r} = -100$ V, the E_i is approximately 2.9 eV, 10% lower than E_i at the optimum point. This approach, therefore, will be applied for the investigation for the rest of the chapter.

6.4 Validation of the RFA

Figure 6.7(a) depicts a number of $\mathrm{d}I_\mathrm{c}/\mathrm{d}V_\mathrm{d}$ of the characteristics measured with the RFA at $t \sim 40-120\,\mu$s during a HiPIMS discharge at the pressure of 0.32 Pa and at a peak target current of 50 A. The $\mathrm{d}I_\mathrm{c}/\mathrm{d}V_\mathrm{d}$, for example at $t = 40\,\mu$s, contains a peak at

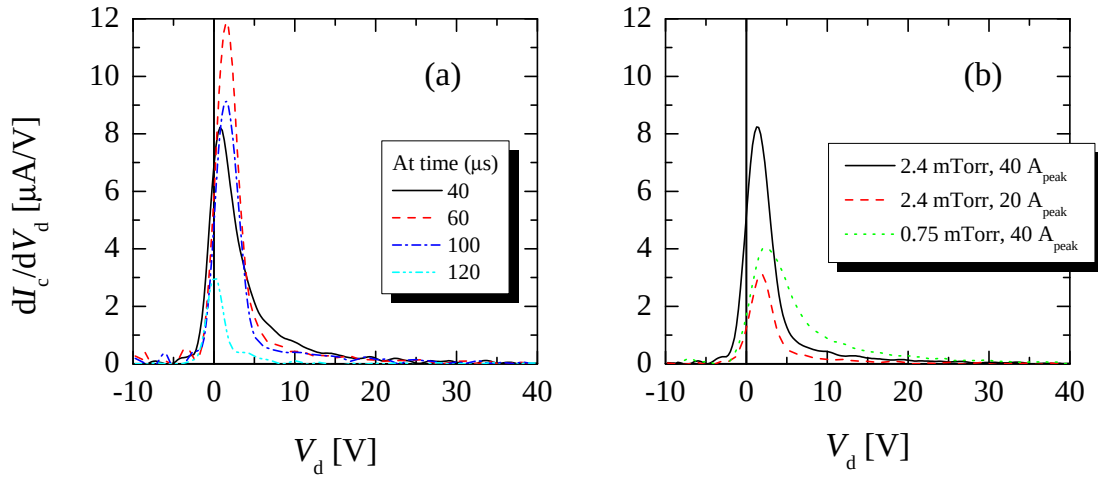

Figure 6.7: a) time-resolved IVDFs measured by the RFA with the repelling voltage of -100 V during HiPIMS pulse at pressure of 0.32 Pa and discharge current of 50 Apeak and b) the averaged IVDFs for a number of discharge conditions.

$V_d \sim 1-3$ V and a tail with corresponding up to 40 V. The peak is mainly attributed to the combination of thermalised argon and metal ions via collisions in the bulk plasma accelerated to the analyser via the plasma sheath in front of the sampling grid. The energetic tail is mainly due to post-ionised sputtered atoms travelling directly from the target as well as ions of sputtering gas reflected from the target [63]. We can clearly see the depletion of the energetic tail during the time progress. The depletion in energetic tail agrees well with the works using energy-resolved mass spectrometers [61,64]. Time-averaged dI_c/dV_d for the HiPIMS plasma can not be performed since the repetition rate (100 Hz) is quite low in comparison with the sweeping rate of the discriminating voltage ($\sim$1000 Hz). Nevertheless, time-averaged dI_c/dV_d may be determined from averaging the time-resolved dI_c/dV_d during the selected time of interest, i.e., 40 μs to 120 μs with 20 μs steps.

The time-averaged dI_c/dV_d for a number of discharge conditions are presented in figure 6.7(b). It was found that an increase of peak current causes an increase of the amplitude of low-energy peak and high-energy tail. By operating at a lower pressure, the width of the low-energy peak is wider. This can be explained by the low-collision frequency or long mean-free-paths at low pressure operation in which the ions can retain their original energy rather than thermalise through collisions with the background gas.

Comparison between time-averaged dI_c/dV_d obtained from the RFA and IEDF from the commercial spectrometer EQP is illustrated in figure 6.8(b). The plot was normalised to the discriminating voltage of +10 V. It should be noted that the IEDF using EQP was obtained from the summation of time-averaged IEDF of each main ionic species in the plasma including Ar^+, Ar^{2+}, Ti^+ and Ti^{2+} as shown in figure 6.8(a). It was found that the normalized IEDF from both devices agree well especially at the energetic tail and the position of the low energy peak. However the magnitude of the

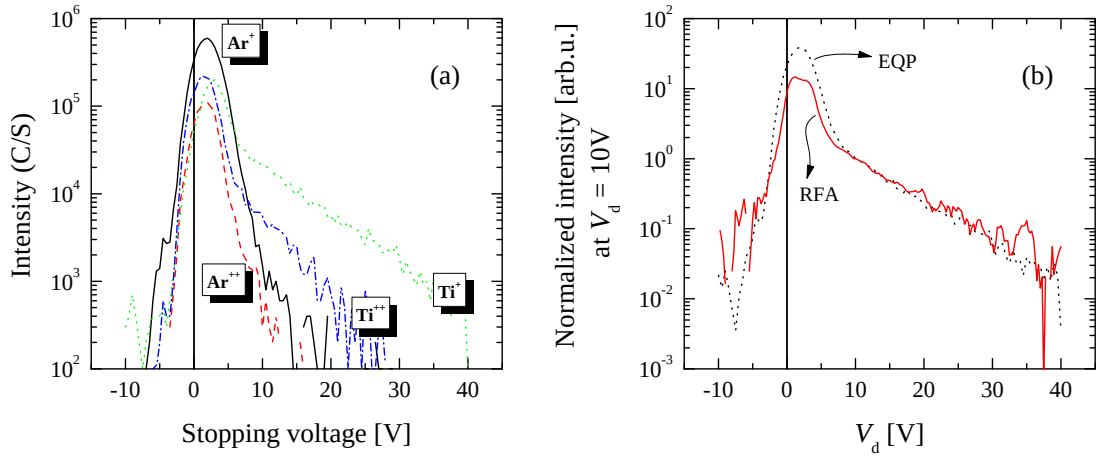

Figure 6.8: (a) IEDFs of main ionic species obtained from the commercial energy-resolved mass spectrometer EQP and (b) comparison between normalized IEDF from the EQP and $\mathrm{d}I_\mathrm{c}/\mathrm{d}V_\mathrm{d}$ from the RFA. The IEDF from EQP was obtained by summing the signal of the main ionic species including Ar^+, Ar^{2+}, Ti^+ and Ti^{2+}.

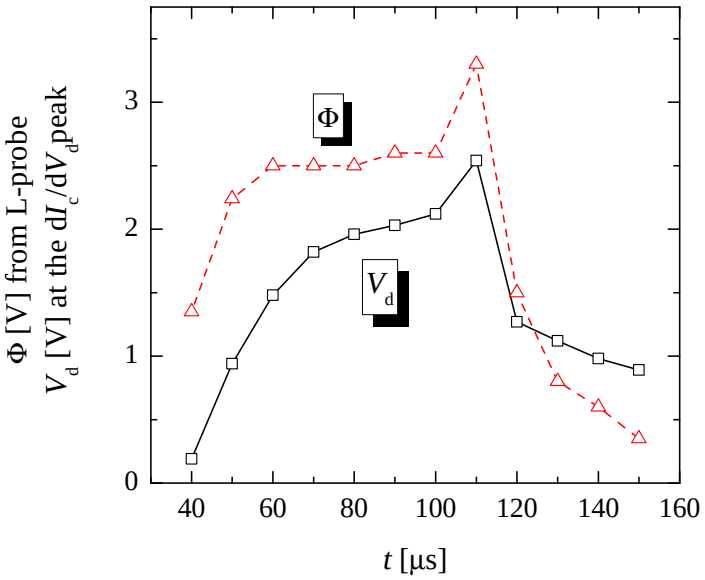

Figure 6.9: A comparison between temporal plasma potential Φ measured by the Langmuir probe (L-probe) and the voltage V_d at the peak of $\mathrm{d}I_\mathrm{c}/\mathrm{d}V_\mathrm{d}$ measured by the RFA.

low energy peak obtained from the RFA is always lower than that from the EQP. One possible explanation is that due to the low energy ions may be partly lost inside the RFA via charge exchange collisions since the pressure inside the RFA was relatively high in comparison with that in the EQP. Another reason may be due to the effect of the smoothing data process which has been performed before and after taking the first derivative. Note that the Savitzky-Golay method was used to smooth the I-V characteristics with 20 data points in smoothing window and a polynomial order of two.

Another comparison for the RFA validation was carried out with Langmuir probe

measurements. Figure 6.9 shows a comparison between V_d at the peak of dI_c/dV_d and plasma potential Φ for the Langmuir probe during $t = 40-150\,\mu$s. The trend of the V_d at the peaks agree well with the temporal evolution of Φ with an offset of about 0.8 V. The offset may be mainly due to the uncertainty of the Langmuir probe measurements in which normally have a uncertainty about 1 – 2 V. The comparison suggests that V_d at the peak position is mainly governed by the local plasma potential formed in front of the analyser. Ions are accelerated through the plasma sheath with energy corresponding to the potential difference between the plasma and the grounded aperture.

6.5 Time-resolved IEDFs

The contour plot of temporal IEDF and the selected ion parameters (Γ_i and $\langle\varepsilon_i\rangle$) during HiPIMS operated at a peak current of 20 A and argon pressure of 0.13 Pa are presented in figure 6.10. Following the temporal evolution, three phases can be distinguished during (1) the early phase $t = 0-20\,\mu$s, (2) the active phase $t = 20-100\,\mu$s and (3) the off-time phase $t > 100\,\mu$s. Note that HiPIMS pulse is stared at $t = 0\,\mu$s and terminated at $t = 100\,\mu$s, as shown in figure 6.1.

The early phase: During the early phase of HiPIMS pulse, the obtained ion current can not be interpreted due to a very low ion density. As mentioned in Chapter 3, the minimum acceptable probe current for the acquisition system is $\sim 1\,\mu$A. Using this current, the minimum ion flux at the first grid can be calculated as follows. Minimum ion flux at the collector, $I_{c,min} = eA\Gamma_{c,min}$, where e is electron charge and A is the area of RFA aperture ($1.76 \times 10^{-6}\,m^2$). Using $I_{c,min} = 1\,\mu$A, the minimum ion flux at the collector $\Gamma_{c,min}$ is $\sim 4 \times 10^{-18}\,m^{-2}\,s^{-1}$. Taking the total transparency of the grids (18%) in the RFA into account, the minimum flux at the first grid $\Gamma_{g,min}$ is approximately $2 \times 10^{-19}\,m^{-2}\,s^{-1}$. The calculated value is consistent with the minimum Γ_i measured by the RFA at $t = 20\,\mu$s as shown in figure 6.10(b).

The active phase: In the active phase, the contour of IEDF reveals a very dynamic features. The energy distribution is weak and broad with energies of up to 15 eV during the early state of this phase. As the time progresses, IEDF evolves from a broad-weak function to a narrow-dense function. The plots of temporal Γ_i and $\langle\varepsilon_i\rangle$ also show the same trend in which the maximum $\langle\varepsilon_i\rangle$ of 10 eV is found at $t \sim 30\,\mu$s while the high ion flux of $\sim 4 \times 10^{20}\,m^{-2}\,s^{-1}$ with $\langle\varepsilon_i\rangle \sim 3.5$ eV can be achieved when $t > 50\,\mu$s. This feature of the IEDF evolution agrees well with time-resolved IEDFs obtained from commercial mass spectrometers [61, 64]. One explanation for the depletion of the high energy portion is associated with the thermalisation process between the energetic sputtered particles and the background gas [63, 64]. Once ejected from the target, the sputtered particles may collide with the background gas and lose their kinetic energy.

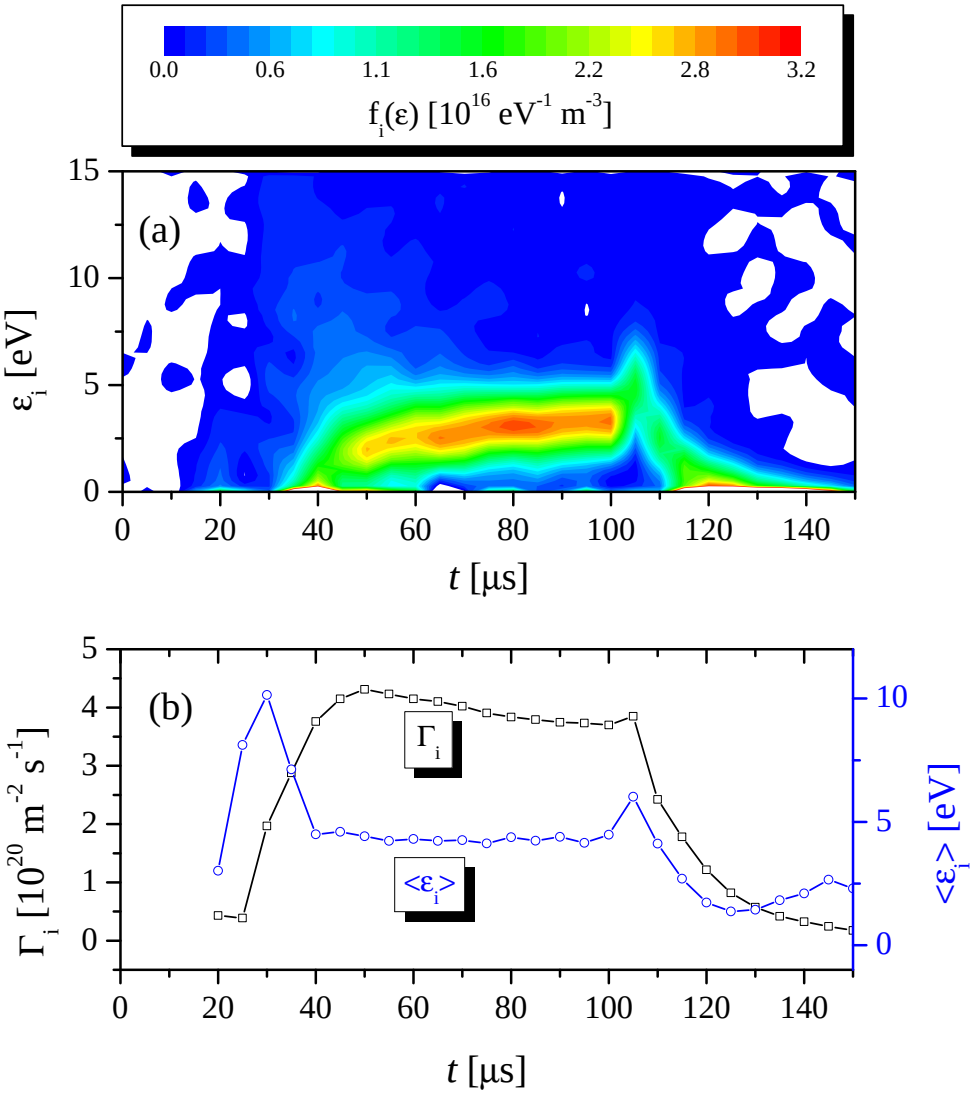

Figure 6.10: a) the contour plot of time-resolved of ion energy, (b) flux and averaged energy of the sampled ions during HiPIMS plasma for 0.13 Pa and 20 A.

The off phase: After the pulse is terminated, the peak position of the IEDF shows a ripple at $t \sim 105\,\mu$s followed by a decay in term of energy and intensity. The indication of the ripple can also be seen in Γ_i and $\langle\varepsilon_i\rangle$; for example, $\langle\varepsilon_i\rangle$ jumps from a stable level of 3.5 eV to 6.5 eV at $t \sim 105\ \mu$s. Since the decay of ion density in afterglow plasma is relatively fast, a reliable signal can not be obtained from the RFA when $t > 130\,\mu$s.

6.6 Conclusions

A two-gridded RFA, operating in the normal mode, together with the commercial Langmuir probe acquisition system, has been used to measure a time-resolved velocity distribution function of ions in HiPIMS plasma. The RFA has been constructed simply and held on the probe feed-through allowing both spatial and angular performance.

The use of low cost TEM grids allows quick replacement of the grid in the deposition system. The IVDF obtained by the RFA agrees well with the IEDF measured by the commercial energy-resolved mass spectrometer. Time-resolved IEDFs obtained for the RFA have show that the ions with $\langle \varepsilon_\mathrm{i} \rangle$ 10 eV can be generated during the initial phase of HiPIMS pulse. These energetic ions are then thermalised with the background gas resulting in the decrease of $\langle \varepsilon_\mathrm{i} \rangle$ down to ~ 3.5 eV for the rest of the pulse.

Chapter 7

Azimuthal ion fluid motions

7.1 Background

High power impulse magnetron sputtering (HiPIMS) is a new thin film deposition technique [2] in which ions formed from the sputtered particles can be the dominant ion species and play a crucial role in deposition and particle transport processes but also during the sputtering process itself [60]. This unique feature not only leads to improved microstructures and properties of the films for industrial applications but also displays new regimes in the physical phenomena at work, not observed in conventional DC or pulsed DC magnetron discharges. These include, runaway self-sustained sputtering [134], strong gas rarefaction [135], magnetic field deformation [136], magnetic de-confinement [121], anomalous (or super-Bohm) electron transport [137, 138] and cross-field side-ways ion transport [53].

Despite its attractiveness, HiPIMS suffers from lower deposition rates compared to mid-frequency pulsed or DC magnetron sputtering. Lundin *et al.* [53] suggested that a significant fraction of ions (including the post-ionized sputtered particles) is transported radially outwards, away from the discharge axis and towards the sidewalls, hence lowering the fraction of ions travelling forwards to the substrate. The mechanism proposed was based on the existence of a two-stream instability between the fast electron E×B drift and the slow ion acoustic fluid leading to an azimuthal force that drives ions tangentially towards the sidewalls. Using an energy-resolved mass spectrometer, they found a considerable flux of high energetic Ti ions leaving the discharge in a direction tangential to the electron E×B drift in the magnetic trap region. The bulky size of the spectrometer employed in [53] somewhat limited the spatial locations for the measurements and in particular the angular information in the ion energy distribution.

In this Chapter the measurements of Lundin *et al* [53]are repeated and extended using a smaller, more manoeuvrable instrument, a retarding field analyser (RFA) allowing the making of finer spatially resolved measurements. Since the analyser is readily moveable and can be rotated completely around its axis, its use here has revealed spatial and angular information on the dynamics of ions transported radially out of the

HiPIMS discharge. In addition, the modified two-stream instability model proposed by Lundin *et al.* [53] is extended by adding a drag force term arising from the collisions of ions with the background gas and the radial force originating from the radial electric field, which was deduced from supplemental emissive probe measurements. Based on these considerations, the equation of motion of the ions is solved.

7.2 Experimental arrangement

7.2.1 Operation of the HiPIMS discharge

All experiments were conducted in the HiPIMS system described in the section 5.2. The cylindrical vacuum vessel was evacuated to a base pressure of 6.5×10^{-4} Pa by the turbo molecular pump backed by the rotary pump. Argon was introduced into the vessel with a flow rate of 0.75 sccm to establish the operating pressure at 0.13 Pa. The magnetron was equipped with the 75 mm titanium target and was energized by the pre-ionised HiPIMS power generators. The generator was set to generate a HiPIMS discharge current at a repetition rate of 100 Hz, a pulse width of 100 μs and a peak of 20 A yielding an energy of 0.88 J per pulse. The waveforms of discharge voltage, V_{dis}, and current, I_{dis}, during the HiPIMS discharge operated with the selected conditions were shown in figure 6.1. The pulse initialisation, at $t = 0\,\mu$s, is characterized by a steep increase of V_{dis} (in the negative direction) followed by a steady rise of the discharge current up to the peak of 20 A at $t \sim 40\,\mu$s. After the peak, I_{dis} and V_{dis} only change marginally indicating a steady state of the discharge which was confirmed by the time-resolved IEDF in figure 6.10 . A temporal position $t = 80$ μs after pulse initialization was therefore selected for all measurements to record representative data for stable discharge operation.

Figure 7.1(a) and (b) shows the magnetron target and the RFA arrangement in a Cartesian coordinate (x, y, z) system as viewed from the top and the side, respectively. The centre of the target surface was placed on the x-y plane at $z = 0$. The centre of the target racetrack (the region of most material sputtering) is represented by a dashed circle of radius $R_{\mathrm{R}} \sim 22$ mm. The magnetic null of the unbalanced magnetron is approximately situated 30 mm above the target surface on the discharge axis (z-axis). The region below this point is referred to as the magnetic trap at which electrons can be captured and efficiently confined by the combination of magnetic and electric field.

For the spatially resolved measurements, the probe feedthrough was set to parallel to the x-axis in which the RFA can be translated along lines parallel to x-axis namely the lines L and $\bar{L}$. Both lines were located 20 mm above the target surface at $y = -35$ mm for line the L and at $y = +35$ mm for line the $\bar{L}$. The locations of both lines were considered to be outside the dense discharge region present in the magnetic trap. The RFA was scanned from $x = -60$ mm to $+60$ mm with a step size of 10 mm. The

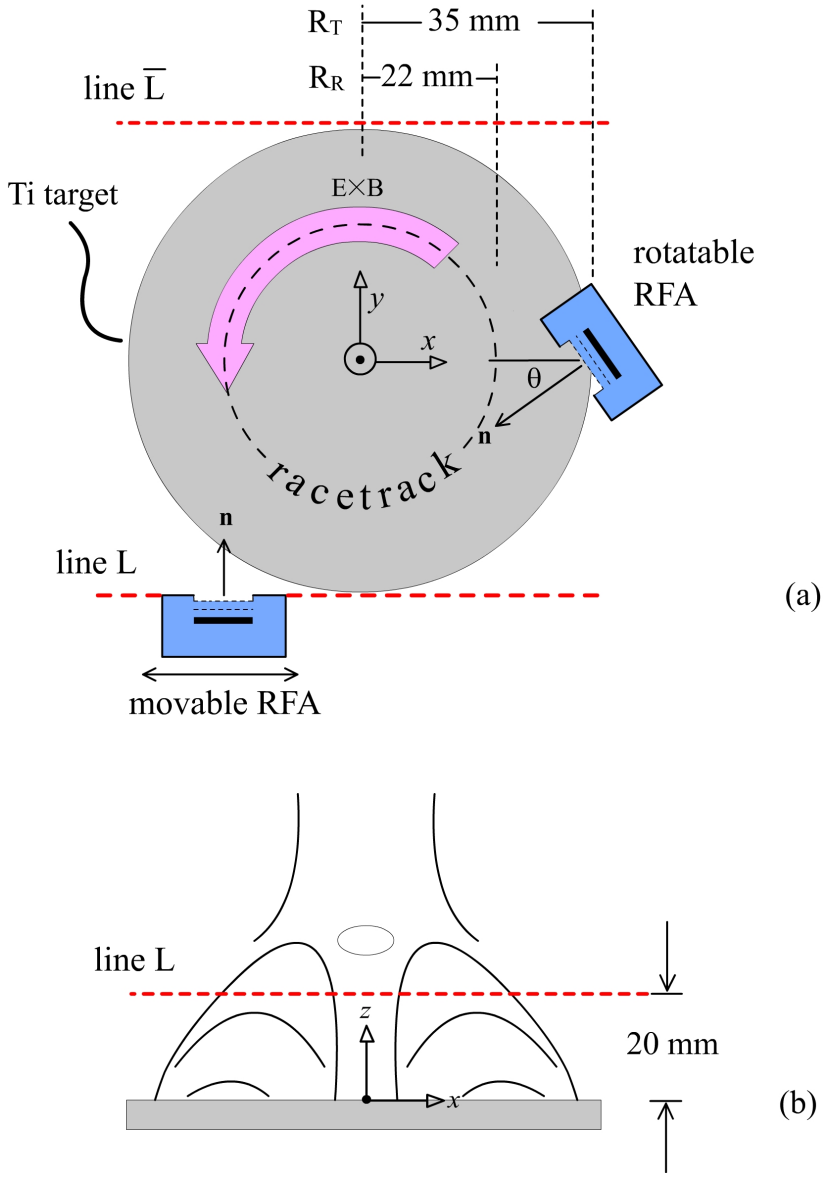

Figure 7.1: (a) Top view and (b) side view of the RFA arrangement in a Cartesian coordinate (x, y, z) system. The origin of the coordinate system is located on the centre of target surface. For spatial-resolved measurements, the RFA was translated along a line L ($y = -35$ mm, $z = 20$ mm) with the probe normal $\mathbf{n} = +\mathbf{j}$ and a line $\overline{\text{L}}$ ($y = +35$ mm, $z = 20$ mm) with $\mathbf{n} = -\mathbf{j}$, where $\mathbf{j}$ is the unit vector of the y-axis. For the angular-resolved measurements, the RFA was rotated around a point (35, 0, 20 mm). The probe angle θ is defined as the angle between $\mathbf{n}$ and the x-axis; for example $\theta = 0°$ when the probe normal is parallel to the x-axis. θ is negative when the probe is rotated clockwise. The effective radius of the racetrack (R_{R}) and the target (R_{A}) is about 22 and 35 mm, respectively.

normal vector $\mathbf{n}$ of the RFA was $+\mathbf{j}$ for the scanning on the line L and $-\mathbf{j}$ for that on the line $\bar{L}$. Note that j is the unit vector of the y-axis.

For the angular-resolved measurements, the probe feedthrough was installed to parallel to the z-axis. The location of the RFA was fixed at a position of $x = 35$ mm, $y = 0$ mm and $z = 20$ mm as shown in figure 7.1(a). The probe angle (θ) is defined as

the angle between the probe normal **n** and the x-axis. For example, $\theta = 0°$ means that the probe faces directly towards the discharge axis. The probe angle θ was negative for clockwise rotated and was positive for counter-clockwise rotated.

As described in Chapter 3, the acquisition system used for the Langmuir probe measurements was employed to obtain the I-V characteristics of the RFA. The I-V characteristic consists of 200 discrete data points of the discriminating voltage V_d in the interval $-10\,\mathrm{V}$ to $+60\,\mathrm{V}$ and the corresponding collector current values I_c. In order to reduce signal fluctuations in a low current range, the sampling number per data point and the sweeps number per scan the data acquisition for were set to 10 and 3, respectively. It implies that 6000 HiPIMS pulses were needed to complete an acquiring I-V characteristic. In addition, the acquired I-V data were mathematically smoothed using a local polynomial regression both before and after taking the first derivative.

7.3 Results and discussions

7.3.1 Spatial distributions of IEDFs

The plots, shown in figure 7.2(a), demonstrate an I-V characteristic and its first derivative for the RFA located on the line L at $x = -20\,\mathrm{mm}$. The I-V curve reveals a constant saturation current $I_\mathrm{i,sat}$ of $\sim 18\,\mu\mathrm{A}$ for low discriminating voltages $V_\mathrm{d} \lesssim 5\,\mathrm{V}$. The point where the collector current first deflects from $I_\mathrm{i,sat}$ can be identified as the plasma potential Φ in front of the RFA. Only ions, generated inside the magnetic trap, with energies $\geq e\Phi$ can reach the grounded sampling grid of the RFA. The ion velocity distribution function which is proportional to the first derivative $\mathrm{d}I_\mathrm{c}/\mathrm{d}V_\mathrm{d}$ is depicted in the same graph.

The ion energy distribution functions (IEDFs) assigned as $f_\mathrm{i}(\varepsilon)$, shown in fig-

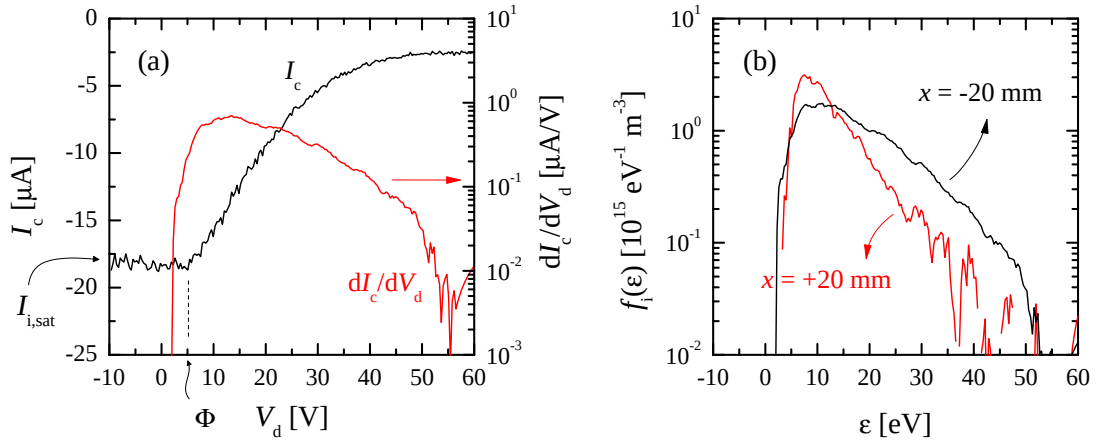

Figure 7.2: (a) An example of the I-V characteristic as well as its first derivative $\mathrm{d}I_\mathrm{c}/\mathrm{d}V_\mathrm{d}$ of the sampling ions measured on the line L at $x = -20\,\mathrm{mn}$ (see figure 7.1). (b) The IEDFs for the sampling ions measured on the line L at $x = -20\,\mathrm{mm}$ in comparison to that at $x = +20\,\mathrm{mm}$.

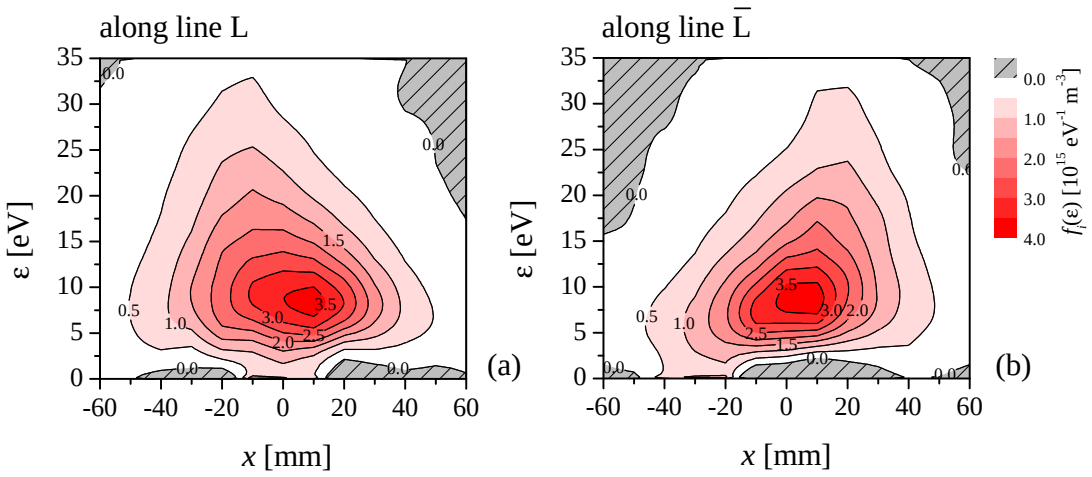

Figure 7.3: Contours of $f_i(\varepsilon)$ on energy-position plane (ε-x plane). The measurements was made along (a) the line L and (b) the line $\bar{L}$.

ure 7.2(b), were consequently obtained from dI_c/dV_d using equation 3.8 and equation 3.16. The IEDFs were recorded for two selected positions on the line L . The first position is at $x = -20$ mm while the second position is at $x = +20$ mm. Obviously, both IEDFs reveal a highly energetic tail up to several tens eV. However, this tail is more pronounced for position $x = 20$ mm where ion energies up to 50 eV were observed. This result, an asymmetric behaviour, agrees well with measurements carried out by conventional energy-resolved mass spectrometry [53].

The asymmetric behaviour indicated in figure 7.2(b) was studied more intensively by translating the RFA along those line L and $\bar{L}$ with a fine step of 10 mm. The IEDFs independence on the RFA position are plotted in figure 7.3. One can clearly see that $f_i(\varepsilon)$ reveals a high energetic tail with similar energies of ions escaping on either side of the discharge. In addition, both spatial distributions clearly show the asymmetric behaviour in which the longest energy tail of $f_i(\varepsilon)$ are not at the centre of x-axis but shifted to an offset position. The position for the longest energy tail was found at about $x = -20$ mm when the RFA was moved along line L, in contrast it changes to $x = +20$ mm when the RFA was translated on the line $\bar{L}$. It can therefore be concluded that a higher flux of energetic ions escape the plasma in a counter-clockwise direction (see figure 7.1) following the electron E×B drift, as previously reported by Lundin *et al.* in [53].

The asymmetric behaviour is further confirmed by the key parameters of the ions calculated from the distribution functions, such as mean energy $\langle \varepsilon_i \rangle$ and mean velocity $\langle v_i \rangle$, as well as ion flux Γ_i which are shown in figure 7.4. A maximum $\langle \varepsilon_i \rangle$ of 17 eV was found and $\langle v_i \rangle$ peaked at 8.1×10^3 m s^{-1}, while the highest Γ_i was 5.2×10^{20} m^{-2} s^{-1}. On a line of the RFA translation, the ion parameters at the peak position are always larger than at the opposite position on the same line. For instance, on the line L, $\langle \varepsilon_i \rangle$

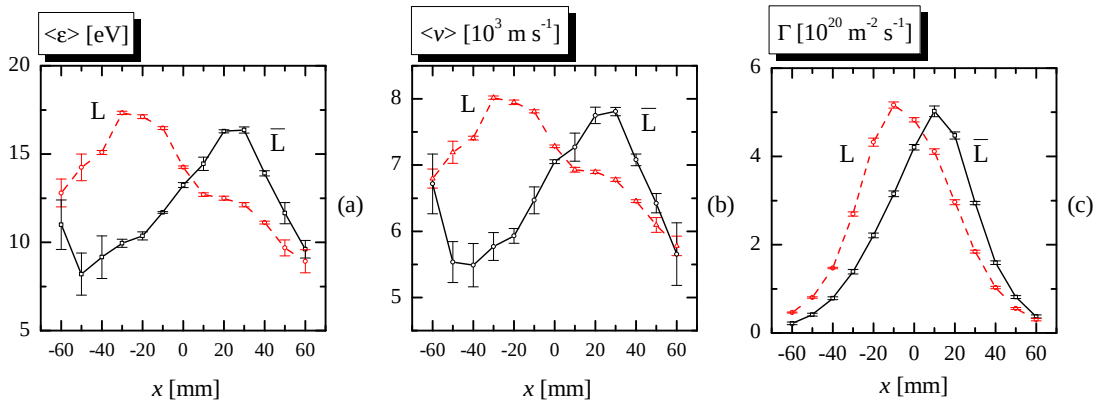

Figure 7.4: Plots of (a) mean energy $\langle \varepsilon_\mathrm{i} \rangle$, mean velocity $\langle v_\mathrm{i} \rangle$ and flux Γ_i of the ions as a function of probe position x when the probe was moved along the line L in comparison to line $\bar{L}$.

at the peak position ($x = -20\,\mathrm{mm}$) is 30% greater than that at $x = +20\,\mathrm{mm}$. This percentage of the difference is also valid for $\langle \varepsilon_\mathrm{i} \rangle$ on the line $\bar{L}$. For $\langle v_\mathrm{i} \rangle$ and Γ_i, the differences are 12% and 40%, respectively. These differences in magnitudes may be due to the fact that the RFA is only sensitive to the normal component of those parameters. For example, the magnitude of the velocity measured by the RFA is $v\cos(\delta)$ with v being the magnitude of the actual ion velocity and δ the angle between the direction of the ion velocity and the RFA normal $\mathbf{n}$. The theoretical difference in the velocity between the positions $+20\,\mathrm{mm}$ and $-20,\mathrm{mm}$, would be about 40 % using $\delta = \tan^{-1}(44/35) \sim 52°$ as an acceptance angle. However, this does not take into account that ions might also be scattered into the acceptance cone which may alter the difference of the ion parameters for the opposition positions.

In order to confirm these preliminary results, measurements were repeated by rotating the RFA around a point located at (35, 0, 20 mm). The contour of $f_\mathrm{i}(\varepsilon)$ are shown in figure 7.5(a) and an asymmetric behaviour is revealed again. Most ions and also the most energetic ions are found at an angle of 30° pointing towards the racetrack region. The $\langle \varepsilon_\mathrm{i} \rangle$, $\langle v_\mathrm{i} \rangle$ and Γ_i obtained from the measured data are displayed in figure 7.5(b) and confirm this trend. The maxima are 6.4 eV, $7.9 \times 10^3\,\mathrm{m\,s^{-1}}$ and $4 \times 10^{20}\,\mathrm{m^{-2}\,s^{-1}}$ for $\langle \varepsilon_\mathrm{i} \rangle$, $\langle v_\mathrm{i} \rangle$ and Γ_i, respectively. It appears that the measured ion flux and energy is significantly more sensitive to rotating the probe than to translating it alongside the magnetron.

7.3.2 A model of ion fluid rotation

In order to understand the dynamics of ions being ejected tangentially out of the discharge, one has to consider the forces acting on them in azimuthal and radial direction in a plane parallel to the target in a polar coordinate system (r, φ). The forces exerted on an element of ion fluid include (1) azimuthal acceleration force, (2) the radial elec-

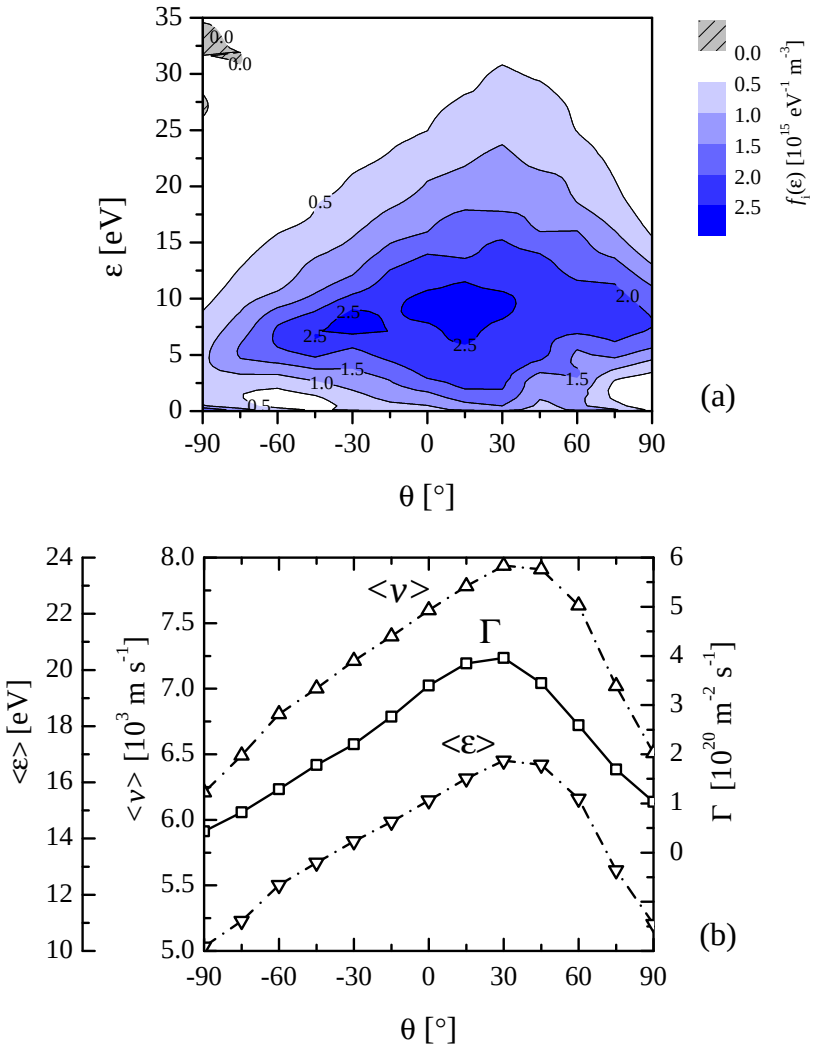

Figure 7.5: (a) The contour of the distribution function $f_{\mathrm{i}}(\varepsilon)$ plotted with the energy ε and the probe angle θ and (b) the plot of the ions parameters including mean energy $\langle\varepsilon_{\mathrm{i}}\rangle$, mean velocity $\langle v_{\mathrm{i}}\rangle$ and flux Γ_{i}.

tric field force and (3) anomalous-resistive drag force. To numerically solve the motion equation of the ions, these acting forces need to be quantified as follows.

Azimuthal acceleration force: Following the original argument of Lundin *et al.* [53], the azimuthal acceleration of the ions in HiPIMS discharges is caused by a two-stream instability. This phenomenon occurs when a high relative velocity between the fast moving electrons, i.e. with drift speed $v_{\mathrm{E}\times\mathrm{B}} = E/B$, and slow ions is present. The average azimuthal force per ion F_φ can be written as a function of the transverse resistivity $\eta_\perp$ [53] and the azimuthal current density J_φ [139] as

$$F_\varphi = -\eta_\perp e n_{\mathrm{e}} J_\varphi \tag{7.1}$$

when

$$\eta_{\perp} = \frac{B}{\omega_{\mathrm{g}} \tau_{\mathrm{coll}} e n_{\mathrm{e}}} \tag{7.2}$$

and

$$J_{\varphi} = \omega_{\mathrm{g}} \tau_{\mathrm{coll}} J_{\mathrm{d}} \tag{7.3}$$

B is the magnetic flux density, e electron charge, n_{e} electron density, ω_{g} electron angular gyro frequency, τ_{coll} the effective electron collision time, J_{d} ($=I_{\mathrm{dis}}/A_{\mathrm{tar}}$) the discharge current density and A_{tar} the effective ion collection area of the target.

Here, the azimuthal force is calculated using the parameters as summarised in the table below.

Table 7.1: A summary of the relevant parameters to calculate the average azimuthal force per ion F_{φ} in the x-y plane at $z = 20\,\mathrm{mm}$ above the target surface.

Parameters	Value	Unit
B	6×10^{-3}	T
e	1.6×10^{-19}	C
n_{e}	1×10^{18}	m^{-3}
$\omega_{\mathrm{g}}\tau_{\mathrm{coll}}$	2	–
A_{tar}	2.8×10^{-3}	m^2
$I_{\mathrm{dis}}(@t = 80\,\mu\mathrm{s})$	17	A
J_{d}	6.1×10^{3}	$\mathrm{A\,m}^{-2}$
J_{φ}	1.2×10^{4}	$\mathrm{A\,m}^{-2}$
$\eta_{\perp}$	1.9×10^{-2}	Ωm
F_{φ}	3.6×10^{-17}	$\mathrm{N\ ion}^{-1}$

It is important to note that this force accelerates the ion fluid only in the area of the discharge where the E×B electron drift is present, i.e. in the magnetic trap. For simplicity, the azimuthal force is set as a constant force inside the effective discharge radius ($\sim$30 mm) and sharply decreases to zero outside as the expression based on the error function [140]:

$$F_{\varphi}(r) = \frac{F_{\varphi o}}{2}\left(1 - \mathrm{erf}\,(\frac{r - r_0}{\varpi})\right) \tag{7.4}$$

where $F_{\varphi o} = 3.6 \times 10^{-17}\,\mathrm{N}$, $\mathrm{erf}(r)$ is an error function of r, $r_0 = 30\,\mathrm{mm}$ and $\varpi = 3.0\,\mathrm{mm}$. The plot of $F_{\varphi}(r)$ with the selected constants is plotted using the solid in figure 7.6(a).

Radial electric field force: The motion observed in the laboratory frame is a circular acceleration. Hence, a radial force F_{r} is necessary to keep the ions on their orbit. This volume force [141] from the redial electric field E_{r} can be written as

$$F_{\mathrm{r}} = n_{\mathrm{i}} e E_{\mathrm{r}}. \tag{7.5}$$

The E_{r} was obtained from the gradient of the plasma potential, i.e. $E_{\mathrm{r}} = -\frac{\mathrm{d}\Phi}{\mathrm{d}r}$. The plasma potential Φ, measured by the emissive probe on a plane $z = 20\,\mathrm{mm}$, is

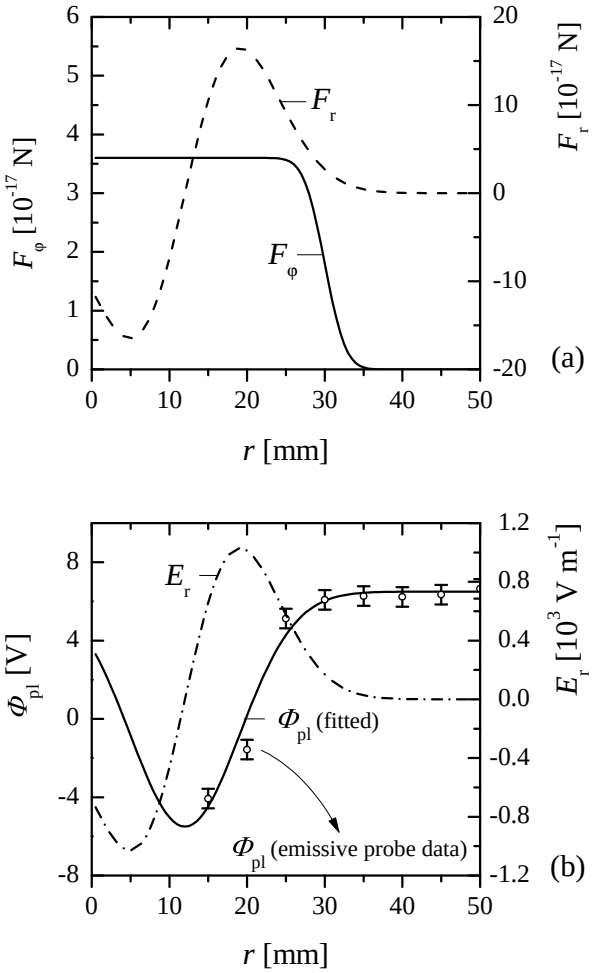

Figure 7.6: (a) function of azimuthal force F_φ and radius force F_r as well as (b) a plot of plasma potential Φ_{pl} from the emissive probe measurement, the fitting plasma potential and the radial electric field E_r as a function of radial distance r from the discharge axis.

represented by open dots in figure 7.6(b). It is worth mentioning that measurements of radial positions $< 15\,\mathrm{mm}$ were not possible due to a significant perturbation of the probe on the discharge. However, spatially resolved measurements published recently by Sanders *et al.* [142] revealed an increase in the plasma potential toward the discharge axis. The shape of the reported plasma potential distribution at a constant distance above the target is close to a Gaussian function in the form of

$$\Phi(r) = \Phi_0 - \frac{a}{w\sqrt{2\pi}} \exp\left(-\frac{(r-r_0)^2}{2w^2}\right), \tag{7.6}$$

The function $\Phi(r)$ is presented using a solid line in figure 7.6(b). The plasma potential off-set $\Phi_0 = 6.5\,\mathrm{V}$ was taken from the measured value far away from the discharge axis ($r = 50\,\mathrm{mm}$). The radial position of the potential minimum $r_0 = 12\,\mathrm{mm}$ was set to be the same position where the magnetic field is orientated parallel to the target. The fitting parameters $a = 0.21\,\mathrm{Vm}$ and $w = 7\,\mathrm{mm}$ represent the amplitude

and the width of the potential distribution. The radial electric field E_r derived from this analytical expression is displayed by the dashed line in figure 7.6(b).

Anomalous-resistive drag force: Apart from these two forces, the ion fluid element also experiences a volume drag force $F_\mathrm{d} = -n_\mathrm{i}\nu_\mathrm{coll}M_\mathrm{i}\langle v_\mathrm{i}\rangle$ caused by the ions colliding with other particles with the collision frequency $\nu_\mathrm{coll} = \sigma n\langle v_\mathrm{i}\rangle$ [4]. Here, the mass of the ions is denoted as M_i, n_i is the ion density, n is the density of particles the ions collide with, σ is the cross-section for this collision and $\langle v_\mathrm{i}\rangle$ is the mean velocity, respectively. Replacing the collision frequency, the anomalous-resistive drag force can be written as

$$F_\mathrm{d} = -n_\mathrm{i}n\sigma M_\mathrm{i}\langle v_\mathrm{i}\rangle^2\,. \tag{7.7}$$

In principle, three kinds of elastic collisions might attribute to the drag term: electron-ion, ion-ion and ion-neutral collisions. Electron-ion collisions are very inefficient in changing the momentum and energy of the ions because of the huge difference in the mass and are therefore not accounted for. Collisions between ions and ions can also be neglected, because this only leads to a redistribution of velocities amongst the ion population with no effect on the mean velocity. The only effective energy loss mechanism is collisions between fast ions and neutrals at about room temperature. The neutral density can be estimated from the background pressure using the ideal gas law, which leads to a density of $n_\mathrm{g} \sim 1\times10^{19}\,\mathrm{m}^{-3}$ for a pressure of 0.13 Pa and a temperature $T_\mathrm{g} = 300\,\mathrm{K}$ also accounting for gas rarefaction as simulations undertaken by Kadlec have revealed [42]. The only collision cross-sections available are for resonant charge exchange between titanium ions and titanium neutrals, $\sigma \sim 2\times10^{-18}\,\mathrm{m}^2$ [80]. The above mentioned value is therefore expected to give a reasonably good approximation and used for the drag force term.

The governing equation: After considering all forces acting on the element of an ion fluid, the equations of motion on the plane of interest is set in the polar coordinate system (r,φ):

Azimuthal direction:

$$\eta_\perp e n_e J_\varphi - n_i n_g \sigma M r\dot{\varphi}\sqrt{(\dot{r})^2+(r\dot{\varphi})^2} = n_i M(2\dot{r}\dot{\varphi}+r\ddot{\varphi}) \tag{7.8}$$

Radial direction:

$$n_i e E_r - n_i n_g \sigma M\dot{r}\sqrt{(\dot{r})^2+(r\dot{\varphi})^2} = n_i M(\ddot{r}-r(\dot{\varphi})^2) \tag{7.9}$$

It is worth mentioning that the derivation of these equation are given in Appendix A.4. The solution was numerically solved using the transverse resistivity $\eta_\perp = 1.9\times10^{-3}\,\Omega\mathrm{m}$, an electron and ion density $n_\mathrm{i} = n_\mathrm{e} = 1\times10^{18}\,\mathrm{m}^{-3}$, a neutral density of $n_\mathrm{g} = 1\times10^{19}\,\mathrm{m}^{-3}$, the mass $M_\mathrm{i} = 7.9\times10^{-26}\,\mathrm{kg}$ for titanium ions and the cross-section $\sigma = 2\times10^{-18}\,\mathrm{m}^2$ with the initial conditions $(t=0)$ of $r = 12\,\mathrm{mm}$ and $\dot{r},\varphi,\dot{\varphi} = 0$.

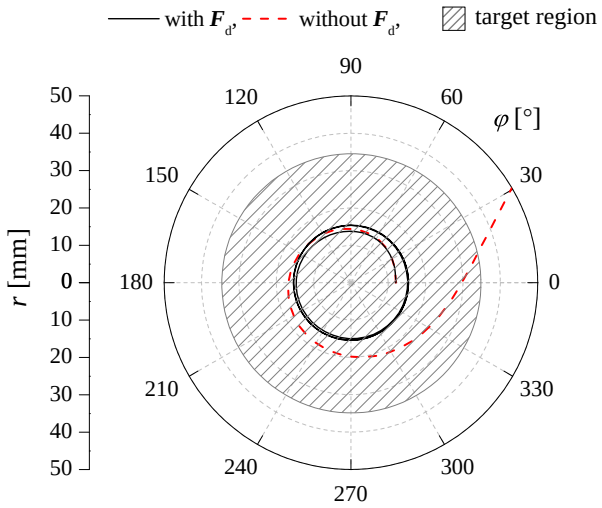

Figure 7.7: The trajectory of an ion fluid element with (solid line) and without (dashed line) the anomalous-resistive drag force F_d in polar coordinates on a plane $z = 20$ mm above the target indicated by the pattern region.

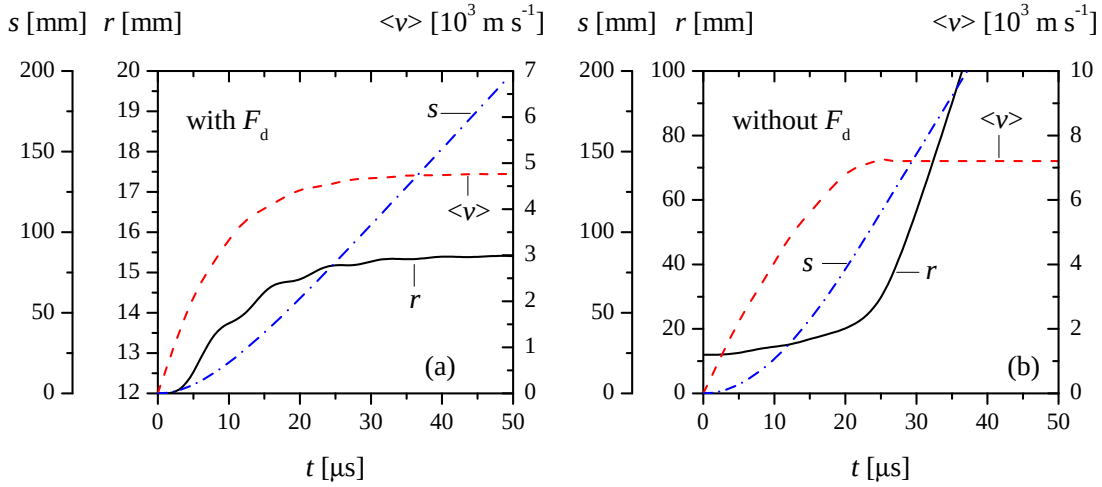

Figure 7.8: The travel distance s, radial position r and mean velocity of the ions $\langle v_i \rangle$ obtained from the model in cases which (a) include and (b) omit the anomalous-resistive drag force F_d.

The numerical solutions: The trajectory path of the fluid ion is presented in figure 7.7 by a solid line. It was found that the ions cannot escape tangentially from the rotating ion fluid if they undergo frequent collisions. However, a small fraction of the ion population might not experience any collisions. These particles follow a motion described by equations similar to the two above but without the drag force term. Such an ion can overcome the highest radial electric fields and is ejected out of the discharge as shown in figure 7.7 by a dashed line. Note that the ion fluid can escape from the magnetic trap when it spin around the discharge axis almost one cycle. This gives additional information on the ion transportation crossing field azimuthal ions proposed by Lundin *et al.* [53].

The travelling distance s, radial position r and means velocity $\langle v_\mathrm{i} \rangle$ as a function of time t are plotted in figure 7.8(a) and figure 7.8(b) for the case with and without the drag force term, respectively. The drag force limits the mean velocity of the ions to $4.8 \times 10^3\,\mathrm{m\,s^{-1}}$. These ions cannot move further than a radial distance of 15 mm away from the discharge axis. A circular motion at an almost constant radius is the consequence. Ions, which do not suffer from collisions, can leave the discharge tangentially with a terminal velocity of about $7.2 \times 10^3\,\mathrm{m\,s^{-1}}$ (equivalent to $\varepsilon \sim 13\,\mathrm{eV}$), which agrees with the mean velocities measured by the RFA (see figure 7.4). On its way to the detector, such an ion travels a total distance of about 130 mm which is about three times the mean free path ($\lambda = 50\,\mathrm{mm}$) under these conditions. The fraction of this ion population can be calculated to $\exp(-s/\lambda) = 0.07$ of the total flux of circulating ions. Hence, only a small fraction of the rotating ion fluid can be detected, which agrees with the experimental findings for the ion density, usually about $5 \times 10^{16}\,\mathrm{m^{-3}}$.

7.4 Conclusions

Velocity and energy distribution functions of ions ejected side-ways out of a HiPIMS discharge recorded by a two-gridded retarding field analyzer revealed high-energetic tails up to 50 eV, mean energies up to 17 eV and mean velocities of up to $8 \times 10^3\,\mathrm{m\,s^{-1}}$. The spatially and angularly resolved measurements showed that the ion flux, the mean velocity and mean energy (differences up to 5 eV) of the ions are distributed asymmetrically; the maxima were obtained into the direction of an oncoming ion fluid rotating in the same direction as the electron E×B drift. This supports the supposition of Lundin *et al.* [53] that a two-stream instability accelerating the ions in azimuthal direction is present. A drag force term, accounting for ion-neutral collisions, and the radial electric force were added to the model proposed in [53] and the equation of motion solved numerically. It was shown that only a small fraction of the circulating ion flux, which does not suffer from collisions, can overcome the radial electric field and leave the discharge volume in tangential direction.

Chapter 8

Ionised metal flux fraction

8.1 Introduction

In HiPIMS, a dense plasma is generated by applying high power unipolar pulses to a target, resulting in a high degree of ionisation of the sputtered species [14]. Having a significant fraction of the sputtered species ionised permits the manipulation of both the energy and direction of the sputtered species via the use of electric fields, particularly in the vicinity of the substrate [1]. These features of HiPIMS not only give the capability of high aspect ratio depositions for semiconductor manufacturing applications [143], but also improve the micro-structures and subsequent properties of hard coating films [21] as well as other functional films [20, 144]. Therefore, the ionisation degree of sputtered species, $n_\mathrm{i}/(n_\mathrm{i}+n_\mathrm{n})$, may be used as a parameter indicating the effectiveness of the discharge. A number of researchers have attempted to measure the degree of ionisation of the metal species by using, for example, the optical emission line ratio method [52] and also to predict it using time dependent global modelling [145].

Another related parameter to the metal density ratio is the metal ionised flux fraction (denoted by Θ) which is defined as the ratio of the metal ion flux to the total flux of depositing particles arriving at a substrate surface [1], i.e. $\Theta = \Gamma_\mathrm{i}/(\Gamma_\mathrm{i}+\Gamma_\mathrm{n})$. As reviewed in [1, 14], Θ in HiPIMS discharges has been reported to be in the range 4.5% to 70% with a strong dependency on the target material.

In HiPIMS, the flux fraction of metal ions, Θ, has been measured using a number of methods. Kouznetsov *et al.* [2] measured the growth rate of Cu films deposited on substrates biased at $-50\,\mathrm{V}$ and $+140\,\mathrm{V}$. The deposition rate caused by the total flux, $\Gamma_\mathrm{n}+\Gamma_\mathrm{i}$, and by the neutral flux, Γ_n, were determined from the weight gain of the negatively biased substrate and of the positively biased substrate, respectively. Ehiasarian *et al.* [21] has also employed the same method, i.e. weight gain method, to measure Θ for a Cr target. Macák *et al.* [59] estimated Θ for a $Ti_{0.5}Al_{0.5}$ target using a fitted curve from an electrical flat probe signal (to determine fluxes of metal ions) together with the deposition rate. In order to determine Θ in real time, DeKoven *et al.* [17] employed a quartz crystal microbalance (QCM) in combination with two-gridded energy

analyser (GEA) for C and Al targets.

The combination of the QCM with the GEA is a well-established technique to determine ionised metal flux fraction in metal ion sources [87] and in ionised physical vapour deposition processes [83–86]. In principle, by using a retarding or an extracting voltage in the GEA, the contribution of the metal ions to the depositing flux can be controlled. Typically, a positive retarding potential is applied to the GEA to suppress the contribution of metal ions in order to determine the neutral flux and a negative extracting potential is applied to permit both the metal ion flux and neutral flux to reach the QCM in order to determine the total flux. To distinguish from a conventional QCM, the method of using a QCM in conjunction with biased grids is referred to as g-QCM throughout this paper.

The g-QCM technique used in this investigation, as in [87], is arranged such that the ion retarding or extracting potential is applied directly to the QCM rather than an external grid. This method reduces the number of external grids required and hence increases the sensitivity of the devices as a result of an increased optical transparency, making it suitable for use in processes with low deposition rates such as HiPIMS.

For the first time, the ionised metal flux fraction in HiPIMS has been investigated experimentally over a range of different average discharge powers as controlled through the independent manipulation of initial target voltage, pulse width and frequency.

8.2 Experimental arrangements

The experiments were conducted in a laboratory scale cylindrical vessel as used in Chapter 4. The vessel was pumped to the base pressure of 4×10^{-4} Pa using a turbo pump together with a rotary pump. Sputtering argon gas (99.995% purity) was flowed into the vessel with a flow rate of 30 sccm to establish the operating pressure of 0.52 Pa measured by an absolute pressure transducer. A magnetron was equipped with a planar disk of a titanium target with a diameter of 150 mm and purity of 99.95%. The magnetic configuration of the magnetron was unbalanced type in which the position of the magnetic null was approximately 70 mm above the target surface. In addition, centre of the sputtering racetrack was approximately 45 mm away from the target centre. The tangential component of the magnetic field at the racetrack centre was about 500 mT. The gridded quartz crystal microbalance (g-QCM) as described in Chapter 3 was employed to measure IMFF in the HiPIMS discharge. The g-QCM was located 130 mm above the racetrack faced directly to the target as shown in figure 8.1.

The average discharge power was varied by three methods; the variation of initial target voltage U_0, pulse width w and pulse frequency f. When changing one of these parameters, other two parameters were fixed. For example, by lengthening the pulse width w from 40 μs to 100 μs, the initial target voltage U_0 and frequency f were kept at -510 V and 500 Hz, respectively. The pulse parameters used are summarized in

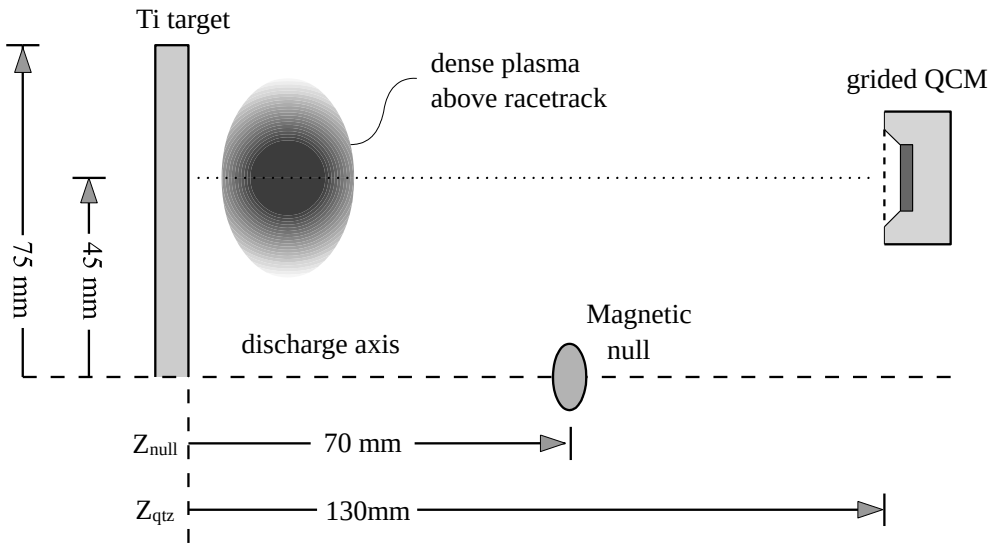

Figure 8.1: Schematic of the experimental arrangement showing a half of the symmetric discharge with following parameters: the target radius of 75 mm, the centre of the racetrack of 45 mm away from the discharge axis, the magnetic null (Z_{null}) of 70 mm away from the target surface. The gridded QCM was located above the racetrack 130 mm away from the target surface.

Table 8.1. The waveforms of discharge voltage, current and power of for three different methods are shown in figure 8.2 The average discharge power P_{avg} can be calculated from the expression [51] as

$$P_{\text{avg}} = f \int_0^w I_{\text{dis}} V_{\text{dis}} \, \mathrm{d}t \tag{8.1}$$

where V_{dis} and I_{dis} are the temporal discharge voltage and current, respectively.

Table 8.1: Summary of pulse parameters used to power up the HiPIMS discharge by adjustments of initial target voltage U_0, pulse width w and frequency f.

Approaches	U_0 [V]	w [μs]	f [Hz]
A	-404 to -450	100	500
B	-510	40 to 100	500
C	-465	100	200 to 600

8.3 Results and discussions

To demonstrate the effect of the bias voltage V_{Q}, the deposition rate R at the quartz surface was measured as a function of V_{Q} during a HiPIMS discharge (with $P_{\text{avg}} \sim 1\,\text{kW}$, $f = 500\,\text{Hz}$ and $w = 100\,\mu\text{s}$). By scanning V_{Q} between $-60\,\text{V}$ and $+60\,\text{V}$, the plot reveals two regions where the measured deposition rate R plateaus, as illustrated in figure 8.3. When $V_{\text{Q}} < -40\,\text{V}$, both metal neutrals and ions can arrive at the quartz surface since there is no potential barrier for the ions to overcome and the rate R

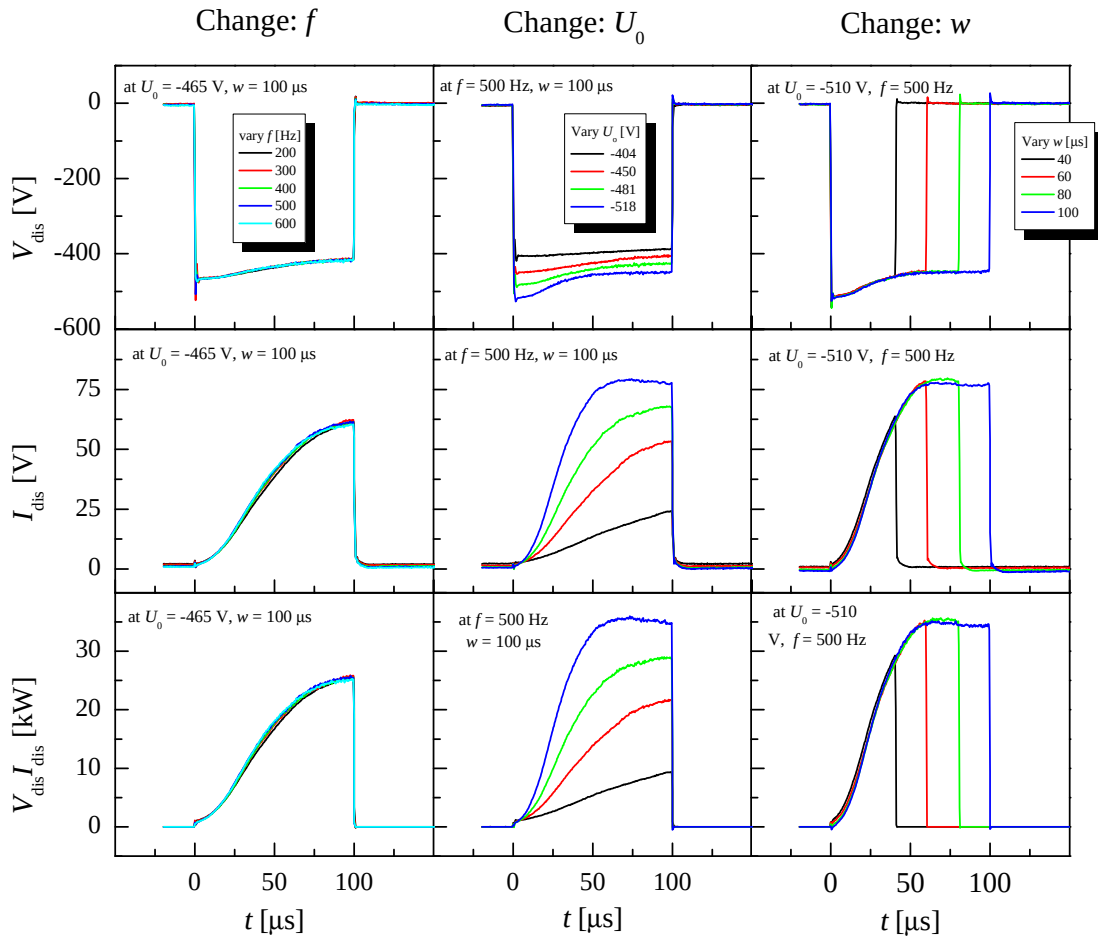

Figure 8.2: The waveforms of discharge voltage, current and power of for three different methods to power up the discharge by changing the frequency f, the initial target voltage U_0 and the pulse width w. The plot shows that is proportional to the P_{avg} in the investigate range

saturates at ~ 0.55 Ås^{-1}. The deposition rate in this case is representative of the total deposition rate R_{t}. In contrast, when $V_{\text{Q}} > +20$ V, the ion contribution is suppressed and the rate R saturates at a lower value of ~ 0.35 Ås^{-1}. In this case, a potential barrier at the gap between the grid and the quartz surface is formed in which singly charged metal ions with kinetic energy of less than $e|V_{\text{Q}} - \Phi|$ can be eliminated from the depositing flux, where Φ is the local plasma potential. Therefore, the deposition rate as measured using a large positive V_{Q} is representative of the metal neutral flux R_{n} only. Using the R_{t} and R_{n} together with the geometry factor G (~ 0.73), the ionized metal flux fraction calculated from equation 3.21 is approximately 29%.

Using the measured R_{n} and the calculated Θ, the actual deposition rates of metal neutrals (R_{N}), metal ions (R_{I}) and the total deposition rate ($R_{\text{T}} = R_{\text{N}} + R_{\text{I}}$) at the first grid surface can be determined. The figure 8.4 shows plots of R_{N}, R_{I}, R_{T} and Θ as a function of P_{avg} varied by three different methods: changing the initial target voltage U_0, the pulse width w and the pulse frequency f. For comparison, the total deposition

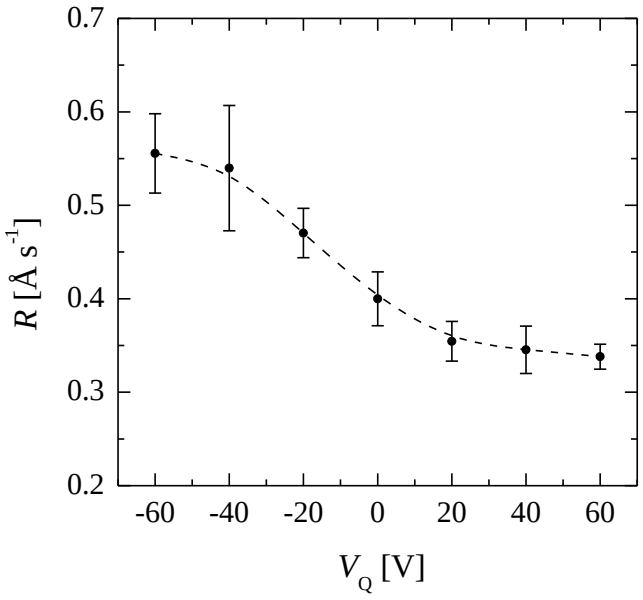

Figure 8.3: The deposition rate R for different bias voltages V_{Q} at the quartz surface during a HiPIMS discharge ($P_{\mathrm{avg}} \sim 1\,\mathrm{kW}$, $f = 500\,\mathrm{Hz}$, $w = 100\,\mu\mathrm{s}$). Using the total deposition rate R_{t} (R at $V_{\mathrm{Q}} \sim -60\,\mathrm{V}$) and the neutral deposition rate R_{n} (R at $V_{\mathrm{Q}} \sim +60\,\mathrm{V}$), the ionized metal flux fraction is approximately equal to 29%.

rate R_{T} for direct-current magnetron sputtering (DCMS) operated at the same argon pressure is displayed. In agreement with previous reports employing a conventional QCM arrangement [146], R_{T} in HiPIMS is found to be lower than that for DCMS across the measured range of P_{avg}. Irrespective of the method used to control the average power, all deposition rates (R_{N}, R_{I} and R_{T}) were observed to increase with P_{avg}. However, the corresponding Θ was found to decrease from a typical value of approximately 50% at $P_{\mathrm{avg}} \sim 0.3$ kW down to 30% at $P_{\mathrm{avg}} \sim 1.3$ kW.

A fundamental overview of deposition rates in HiPIMS discharges is given in detail by Anders [51]. During the sputtering process, neutral particles are ejected from the target surface as a result of bombardment by energetic ions. The particles flux (Γ_{sp}) sputtered from the target is dependent upon both the flux (Γ_{bi}) and energy ($\varepsilon_{\mathrm{bi}}$) of bombarding ions, which is in turn related to the discharge voltage I_{dis} and current V_{dis}.

For a plasma containing electrons and singly charge ions, Γ_{sp} can be written as$\Gamma_{\mathrm{sp}} \propto \Gamma_{\mathrm{bi}} \cdot \gamma\left(\varepsilon_{\mathrm{bi}}\right)$ where $\gamma\left(\varepsilon_{\mathrm{bi}}\right)$ is the sputtering yield as a function of the energy of bombarding ions. The flux of bombarding ions relates to the discharge current at the target as $\Gamma_{\mathrm{bi}} = I_{\mathrm{dis}} / \left(eA_{\mathrm{tar}}\right)$. The sputtering yield relates to the discharge voltage as $\gamma \propto \sqrt{eV_{\mathrm{dis}}}$. Thus, the sputtered flux Γ_{sp} generated at the target, for the case of a HiPIMS discharge with a frequency f and a pulse width w, can be written as [51]

$$\Gamma_{\mathrm{sp}} \propto f \int_0^w I_{\mathrm{dis}} \sqrt{V_{\mathrm{dis}}}\, \mathrm{d}t \tag{8.2}$$

When travelling towards the substrate, the metal neutral flux has a probability α of

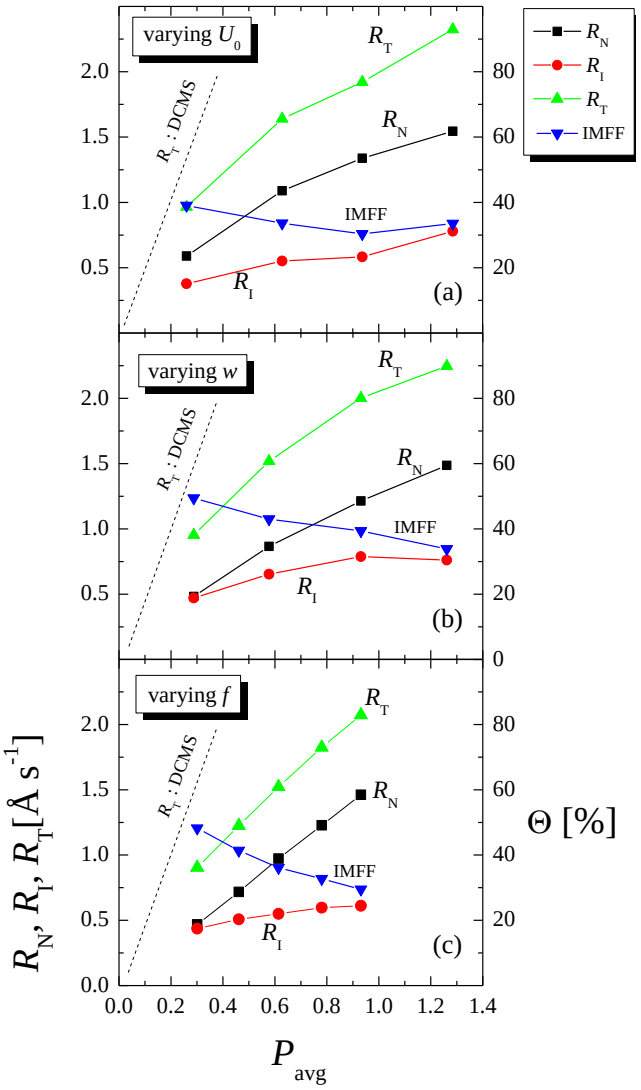

Figure 8.4: A plot of deposition rate of metal neutrals (R_{N}), metal ions (R_{I}), the total rate (R_{T}) and the ionized metal flux fraction, Θ, as a function of average power P_{avg} varied by changing (a) the initial target voltage, (b) pulse width and (c) frequency. The dotted line represents the total deposition rate of a conventional DC magnetron sputtering (DCMS). All types of deposition rates represent the rates on the grid R (the corresponding -40 V bias substrate).

being ionised by the dense magnetized plasma above the target surface. Hence, the flux of metal neutrals arriving at the substrate can be written as $(1-\alpha)\Gamma_{\mathrm{sp}}$, that is if the sticking coefficient of the neutral species is unity. The newly formed metal ion flux can be expressed as $\alpha\Gamma_{\mathrm{sp}}$, however, there is a finite probability β of the ionised flux returning back to the target due to the ion retarding potential gradient extending into the plasma adjacent to the target surface [50, 147]. Assuming a sticking coefficient of unity for the metal ions, the metal ion flux reaching the substrate is therefore $\alpha(1-\beta)\Gamma_{\mathrm{sp}}$. Based on this model, the deposition rates caused by the neutral and ion fluxes can be written as

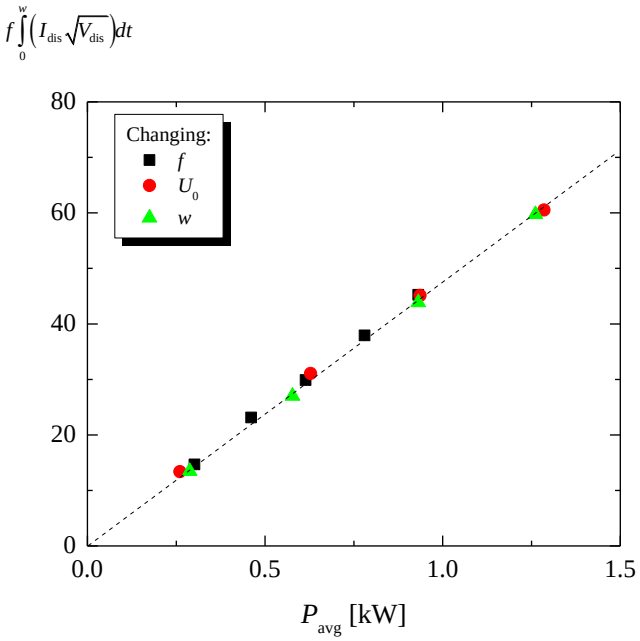

Figure 8.5: Plot of $f\int_0^w I_{\mathrm{dis}}\sqrt{V_{\mathrm{dis}}}\,\mathrm{d}t$ as a function P_{avg} of for three different methods to power the discharge. The plot shows that $f\int_0^w I_{\mathrm{dis}}\sqrt{V_{\mathrm{dis}}}\,\mathrm{d}t$ is proportional to the P_{avg} in the investigate range. Therefore, $\Gamma_{\mathrm{sp}} \propto P_{\mathrm{avg}}$ can be assumed for simplification.

$$R_{\mathrm{N}} = K(1-\alpha)\Gamma_{\mathrm{sp}} \tag{8.3}$$

and

$$R_{\mathrm{I}} = K(1-\beta)\alpha\Gamma_{\mathrm{sp}}, \tag{8.4}$$

respectively, where K is an arbitrary constant [51]. Hence, the total deposition rate RT is given by

$$R_{\mathrm{T}} = K(1-\alpha\beta)\Gamma_{\mathrm{sp}}, \tag{8.5}$$

The plot of Γ_{sp} as a function of P_{avg}, using different waveforms of V_{dis} and I_{dis}, revealed that the metal flux generated at the target is proportional to the average discharge power in the investigated range as shown in figure 8.5. As a result, the assumption of $\Gamma_{\mathrm{sp}} \sim P_{\mathrm{avg}}$ can be made for simplification. This then implies that the total deposition rate R_{T} should experience a linear increase with P_{avg}, assuming that α and β approach a value of zero or little change with P_{avg}, which is likely the case in a conventional DCMS device. In HiPIMS, however, much larger values for α and β (with an upper limit of 1) have been widely reported [49,145]. Moreover, different pulse parameters used in the discharge can cause a significant charge in α and β. Following this framework, the three methods of power control are considered in turn and an explanation responsible for the relationships between P_{avg} and R_{N} and R_{I} is given.

Increasing the power by means of increasing the initial target voltage U_0 directly enhances electron density in the plasma and consequently increases the values of both α and β. An increased electron density typically results in a greater probability of ionisation of the sputtered metal neutrals (i.e. an increased value of α). Additionally, a higher U_0 also results in a greater ion retarding potential in the vicinity of the target and an extended pre-sheath region which leads to a higher probability of metal ions returning to the target (i.e. increased value of β). As a consequence, both R_{N} and R_{I} show a non-linear increase with increasing P_{avg} when controlled by increasing the value of U_0, as seen in figure 8.4(a).

When controlling P_{avg} by changing the pulse width w, the time evolution of α and β during the pulse on-time may need to be considered. When using a short pulse on-time (e.g. $w = 40\,\mu$s), the discharge current is prevented from reaching a peak value, resulting in a low ionisation probability α when compared with longer pulse on-times. However, a short pulse on-time reduces the probability of the discharge developing into a self-sputtering mode due to a decreased ion return probability β [52]. By operating with a longer pulse on-time, both α and β tend to increase as the discharge current is allowed to develop beyond a peak value and into a steady state (e.g. when $w = 100\,\mu$s).

It is predicted from the model presented in [51] that R_{N} and R_{I} should be exactly proportional to the HiPIMS frequency for identical discharge current-voltage-time waveforms since values of α and β are fixed for identical waveforms. As shown in figure 8.4(c), when the average discharge power is varied by means of changing f, R_{N} is found to increase proportionally with P_{avg}. However, this is not the case for R_{I}, which is shown to have a non-proportional relationship and a less pronounced increase with P_{avg}. This unexpected behavior of RI may be attributed to the thermalization of metal ions in the afterglow plasma. It has been reported by Hecimovic and Ehiasarian [148] that, when using a titanium target, metal ions are still present in the system during the pulse off-time. By accounting for these residual metal ions, the expression for R_{I} can be modified and written as

$$R_{\mathrm{I}} = \alpha(1-\beta)\Gamma_{\mathrm{sp}} + f\int_{t_{\mathrm{on}}}^{t_{\mathrm{off}}} \Gamma_{\mathrm{AF}}(t)\,\mathrm{d}t \tag{8.6}$$

The first term on the right hand side of equation 8.6 is associated with the metal ions present during the pulse on-time and is assumed constant for a fixed w while the second term is related to the decay of metal ion density in the pulse off-time. When operating a HiPIMS discharge with a low frequency (a longer off-time interval), the second term in equation 8.6 increases as the metal ions have a longer time period in which to arrive at the substrate and a higher value of Θ is observed. In contrast, when operating with a higher frequency (a shorter off-time interval), the second term will decrease as the metal ions have less time to be collected at the substrate. The diminished metal ion flux results in an observed decrease in Θ, as illustrated in figure 8.4(c).

8.4 Conclusions

In the present work, the ionized metal flux fraction during HiPIMS discharges was investigated using a biased quartz crystal microbalance in conjunction with a gridded electron suppressor. In addition, the deposition rate caused by the metal neutral flux R_{N} and the metal ion flux R_{I} at a substrate biased to $-40\,\mathrm{V}$ were determined separately. The ionized metal flux fraction for a titanium target during typical HiPIMS operation was found to be in the range of $30-50\%$. It was also found that as the average discharge power was increased, the flux fraction of metal ions arriving at the substrate decreased. The mechanism responsible for the observed decrease in the ionized metal flux fraction is proposed to be a combination of the ionisation probability of the sputtered species and the ion-returning effect as well as the presence of metal ions in the afterglow plasma during the pulse off-time.

Chapter 9

Conclusions and future work

9.1 Conclusions of the study

Plasma investigations, specifically on the measurements of plasma parameters in the HiPIMS discharges using electrical diagnostic tools, were presented.

The primary diagnostic tools used were the cylindrical Langmuir probe, the two-gridded retarding filed analyser and the gridded quartz crystal microbalance. The Langmuir probe was used to obtain various properties of the electrons such as the density (n_e), the temperature (T_e) and the electron energy distribution function (EEDF). The retarding field analyser was employed to measure the ion velocity distribution function (IVDF) and the other related parameters of ions such as the ion energy distribution function (IEDF), the mean velocity $\langle v_i \rangle$, the mean energy $\langle \varepsilon_i \rangle$ and the ion flux Γ_i. An energy-resolved mass spectrometer and an emissive probe were utilised as supplementary diagnostic tools to measure the IEDF of specific ion species and the local plasma potential Φ, respectively. The gridded quartz crystal microbalance was developed to measure the metal ionised flux fraction. As a consequent, the deposition flux caused by metal neutrals and ions can be independently determined.

The fundamental properties of plasma electrons such as n_e, T_e, the EEDF were investigated by performing time-resolved Langmuir probe measurements, as described in Chapter 4. The measurements, with a time-resolution of less than $0.5\,\mu$s, were performed throughout the whole period of a HiPIMS discharge. Using the sufficient time-resolution, the fast phenomena occurring in the pulse was identified. During the initial state of the HiPIMS pulse (the first $4\,\mu$s), three distinct groups of electrons were observed, namely, super-thermal, hot and cold electrons with effective temperatures of $70-100\,$eV, $5-7\,$eV and $0.8-1\,$eV, respectively. Beyond this state, these electrons merge to form a single-temperature Maxwellian with an electron temperature between $3-5\,$eV for the rest of the pulse. The presence of the super-thermal electrons group pushes the probe floating potential V_f to very negative value deeper than $-95\,$V during the initial period of the pulse. The very negative V_f in HiPIMS discharges was also confirmed by the independent probe biasing method in which $V_f < -500\,$V was

observed. Long-term phenomena during the afterglow was also investigated. In the afterglow plasma, the electron density decays initially with a fast rate and ultimately with a slow rate. The characteristic time for the fast and the slow rates of the plasma density were $30-40\,\mu$s and $3-4\,$ms, respectively. The long decay time caused the relative high density remnant plasmas ($\sim 10^{15}\,\mathrm{m}^{-3}$) at the end of the off-time, which serves as the plasma seed for the next discharge pulse.

At low pressures (below 0.53 Pa), a noticeable delay time in the waveform of the HiPIMS discharge current was observed. The delay time, becoming on the same order of time as the HiPIMS pulse width, was found to limit the minimum operating pressure in HiPIMS discharges. In Chapter 5, the combination of a DC pre-ioniser and a HiPIMS power supply was proposed for operating HiPIMS discharges in the low-pressure range. The pre-ioniser was used to provide the background plasma with an electron density of $10^{15}\,\mathrm{cm}^{-3}$ which aids the HiPIMS current to develop with a negligible delay time. With the assistance of the pre-ioniser, the minimum pressure that a HiPIMS discharge could be operated at was approximately 0.08 Pa for the system used here. Using the energy-resolved mass spectrometer, the ion composition and IEDF for the low-pressure HiPIMS discharge were investigated. The mass/charge spectrum, measured for ions with an energy of 0.5 eV, showed that the intensity of Ti^{2+} ions was larger than that of Ti^{+} in the low-pressure operation. In addition, highly charged ions including Ti^{3+} and Ti^{4+} were also found in the low-pressure operation. It was suggested from the mass/charge spectrum that the average charge stage of metal ions increased with decreasing operating pressure. Time-averaged IEDF measurements revealed that a larger population of energetic metal ions was obtained at the pressure of 0.08 Pa in comparison with that at 0.53 Pa. The increase of the average charge state and the energy of metal ions was suggested to be beneficial in carrying the momentum to the substrate, enhancing the density of the growing films.

In thin film deposition, ion bombardment during the film growth is an important strategy for increasing the mobility of the depositing particles, which in turn improves the overall properties of the growing films. Several studies have shown that by adjusting the energy of the bombarding ions, the microstructure of the growing film can be modified [25]. Monitoring the energy and related parameters of the bombarding ions during the deposition process is thus of importance. A retarding field analyser (RFA), as described in Section 3.3, was developed to measure the IVDF, IEDF, $\langle v_\mathrm{i}\rangle$, $\langle \varepsilon_\mathrm{i}\rangle$ and Γ_i during HiPIMS discharges. The two-gridded configuration of the RFA, operating in the normal mode, was chosen, allowing a commercial acquisition system for the Langmuir probes to be employed for gathering the time-resolved IEDF measurements, as performed in Chapter 6. The IEDF obtained from the RFA was shown to be consistent with measurements using a commercial energy-resolved mass spectrometer. Time-resolved IEDF measurements revealed that high-energy ions with $\langle \varepsilon_\mathrm{i}\rangle \sim 10\,$eV

were found during the initial $20-30\,\mu$s of the HiPIMS pulse. The $\langle\varepsilon_{\mathrm{i}}\rangle$ of the energetic ions decreased from 10 eV to 3 – 5 eV for the rest of the pulse due to thermalisation with the residual gases.

Deposition rates during a HiPIMS discharge have been reported to be lower than that during dc magnetron sputtering operating at the same average power. One explanation for the low rate of deposition in HiPIMS discharges, proposed by Lundin *et al.* [53], is associated with the anomalous transport mechanism of ions in the azimuthal direction caused by a two-stream instability between the fast electron E×B drift, and the slow ion fluid. As a result, a fraction of metal ions are lost from the discharge volume to the side walls, consequently lowering the number of metal ions travelling to substrates located at the typical position. The study of the ions escaping in the azimuthal direction was extended in Chapter 7. Using the maneuverable RFA, spatial and angular IEDF measurements for the escaping ions were measured. The IEDF measurements revealed the asymmetric features in which the $\langle\varepsilon_{\mathrm{i}}\rangle$ was maximum (~ 17 eV) at a specific position and probe angle corresponding to the line-of-sight path of oncoming rotating ion fluid. To understand the dynamics of the azimuthally ejected ions, the circular motion equations of the ion fluid element was modelled. The model included three exerting volume forces namely the azimuthal driving force [53], the radial electric field forces and the anomalous drag force. The equations were solved numerically, revealing that unless it suffered from collisions with the background gas, the ion element was able to leave the discharge tangentially, with an $\langle v_{\mathrm{i}}\rangle$ of 7.2×10^{3} m s^{-1} corresponding to an $\langle\varepsilon_{\mathrm{i}}\rangle$ of ~ 13 eV which agrees well with the $\langle\varepsilon_{\mathrm{i}}\rangle$ measured by the RFA.

The flux ratio of bombarding ions to depositing neutrals at a substrate is an important process parameter influencing to film microstructure [149]. In HiPIMS, this flux ratio closely relates with the ionised metal flux fraction (IMFF). Using a biased quartz crystal microbalance in combination with a gridded electrode (g-QCM), the IMFF in a HiPIMS discharge operated with a titanium target has been investigated. Moreover, the deposition rate caused by metal neutrals (R_{N}) and metal ions (R_{I}) can be determined separately. With the selected configuration, the g-QCM can achieve an acceptable sensibility which is suitable for HiPIMS discharges where the deposition rate is rather low. In Chapter 8, the IMFF and R_{N} and R_{I} are investigated for different average power density controlled by varying three different parameters; initial target voltage, pulse width and pulse frequency. The average discharge power was varied from 0.3 to 1.3 kW and, irrespective of the power control method used, an associated decrease in the flux fraction (from 50% to 30%) was observed. The mechanisms responsible for this decrease in the time-averaged the flux fraction of metal ions were discussed including the ionization of metal neutral, the ion-returning back to the target and the presence of metal ions in the afterglow.

9.2 Suggestion for future work

Further development in miniature RFA would be of interest to explore the energy distribution functions and the related parameters of ions inside the magnetised zone. The RFA needs to be compact enough for translating and rotating inside the magnetised volume near the target with less perturbation to the discharge. With the capabilities of translating and rotating the RFA, azimuthal ions circulating inside the magnetised zone can be further investigated. A direct investigation may be useful in verifying the models for the ion fluid motions circling above the target in the azimuthal direction. Furthermore, by turning the RFA away from the magnetron target, ions travelling back to the target due to the presheath expansion in the magnetised zone may be investigated.

The ability to operate a HiPIMS discharge at a very low pressure ($< 0.13\,\mathrm{Pa}$) may be useful for exploring physical phenomena occurring in the HiPIMS discharge. One such interesting phenomena is gas rarefaction [42, 46, 94]. This is the reduction of the gas density in the vicinity of the target due to heating from the energetic sputtered flux [150]. During the on-time of a HiPIMS pulse, the decrease in argon density above the target can either significantly reduce the target current [46] or even shut off the discharge [94]. During the off-time interval, gas species should diffuse back to the target region within a refilling time ranging between 50 and 100 μs after the pulse termination as pointed out by Lundin *et al.* [46]. If the pulse width of the HiPIMS discharge is longer than the refilling period, a second rise of the discharge current due to the returning of the sputtering gas could be expected. Therefore, the oscillation of discharge current within a long HiPIMS pulse should be observed due to the back and forth motion of the sputtering gas. Some observations in the oscillation of the current waveforms in a long HiPIMS pulse are presented in Appendix B.

Appendix

Appendix A

Derivations

A.1 A brief of OML theory

The comprehensive derivation for orbital motion limited (OML) theory can be found in a number of plasma textbooks [4, 65, 82]. However, a brief of OML theory [151] are summarised as follows.

Consider singly charged ions mass M are being collected by a cylindrical probe having a radius (r_p), a length (l_p), an area ($A_\mathrm{p} = 2\pi r_\mathrm{p} l_\mathrm{p}$) and the impact parameter (h_p) as shown in figure A.1. Assume that the collecting ions have an initial velocity v (at the plasma sheath-edge) and arrive to the probe with velocity v_c. If the potential at the plasma sheath-edge is Φ and the potential at the probe is V_c, the equation of energy conservation of the ions can be written as

$$\begin{aligned} \frac{Mv^2}{2} + e\Phi &= \frac{Mv_\mathrm{c}^2}{2} + eV_\mathrm{c} \\ 1 &= \left(\frac{v_\mathrm{c}}{v}\right)^2 - \frac{2e\left(\Phi - V_\mathrm{c}\right)}{Mv^2} \end{aligned}$$

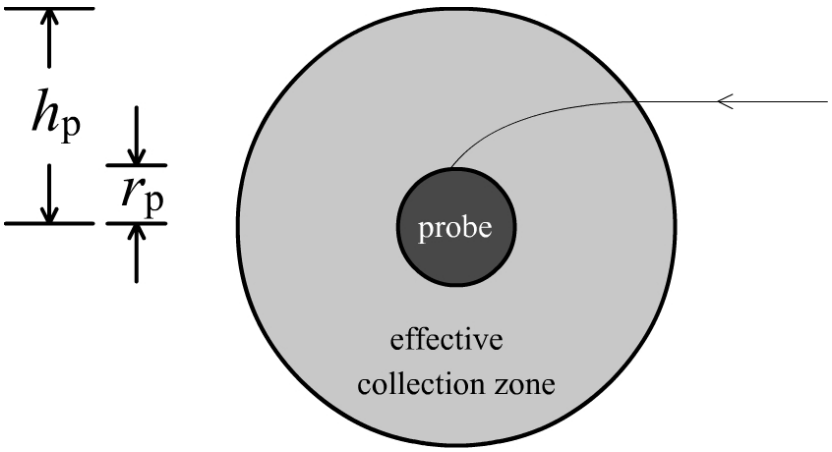

Figure A.1: A cross-section diagram showing the orbital trajectory of an ions arriving to a cylindrical probe having a radius r_p and an impact parameter h_p.

$$\therefore \frac{v_c}{v} = \sqrt{1+\frac{2e\left(\Phi - V_c\right)}{Mv^2}}$$

Using the conservation of angular momentum, the impact parameter h_p can be written as

$$\begin{aligned} Mvh_p &= Mv_c r_p \\ h_p &= r_p\left(\frac{v_c}{v}\right) \\ \therefore h_p &= r_p\sqrt{1+\frac{2e\left(\Phi - V_c\right)}{Mv^2}} \end{aligned}$$

If the effective area to collect the ions is $A_{eff}(= 2h_p l_p)$, the ion current I_i due to the collecting ions with any velocity v is

$$\begin{aligned} \mathrm{d}I_i &= evA_{eff}\,\mathrm{d}n \\ \mathrm{d}I_i &= ev2h_p l_p\,\mathrm{d}n \\ \mathrm{d}I_i &= \left[2el_p r_p\sqrt{1+\frac{2e\left(\Phi - V_c\right)}{Mv^2}}\right] v\,\mathrm{d}n \end{aligned}$$

If the ions follow a Maxwellian distribution function with a temperature T_i and a density n_i, thus ion density n having velocities between v and $v + \mathrm{d}v$ for a cylindrical probe is

$$\mathrm{d}n = n_i\left(\frac{M}{2\pi k_B T_i}\right)\exp\left(-\frac{Mv^2}{2k_B T_i}\right)2\pi v\,\mathrm{d}v$$

Therefore,

$$\mathrm{d}I_i = \left[2el_p r_p\sqrt{1+\frac{2e\left(\Phi - V_c\right)}{Mv^2}}\right] v\,n_i\left(\frac{M}{2\pi k_B T_i}\right)\exp\left(-\frac{Mv^2}{2k_B T_i}\right)2\pi v\,\mathrm{d}v$$

and

$$I_i = 4el_p r_p n_i\int_0^\infty\left(\frac{M}{2k_B T_i}\right)\sqrt{1+\frac{2e\left(\Phi - V_c\right)}{Mv^2}}\exp\left(-\frac{Mv^2}{2k_B T_i}\right)\mathrm{d}v$$

Using the approximation technique proposed in [151], the ion current can be written as

$$I_i = 2\pi n_i r_p l_p e\frac{2}{\sqrt{\pi}}\sqrt{\frac{k_B T_i}{2\pi M}}\sqrt{1+\frac{e\left(\Phi - V_c\right)}{k_B T_i}}$$

Consider the ion current at the ion saturation region where $e\left(\Phi - V_c\right) \gg k_B T_i$, thus $\frac{e(\Phi - V_c)}{k_B T_i} \gg 1$.

$$I_i \approx 2\pi n_i r_p l_p e\frac{2}{\sqrt{\pi}}\sqrt{\frac{k_B T_i}{2\pi M}}\sqrt{\frac{e\left(\Phi - V_c\right)}{k_B T_i}}$$

Therefore, the ion current predicted using the OML theory can be written as

$$I_i \approx \frac{\sqrt{2}}{\pi}eA_p n_i\sqrt{\frac{e\left(\Phi - V_c\right)}{M}},$$

where $A_p(= 2\pi r_p l_p)$ is the area of the cylindrical probe.

A.2 The estimation for Maxwellian electron density

Assume that electrons follow a Maxwellian distribution function, the random flux of the electrons to the probe can be written as

$$\Gamma = \frac{n_{\mathrm{o}}\bar{v}}{4}\exp\left(-\frac{e\Delta\phi}{k_{\mathrm{B}}T_{\mathrm{e}}}\right),$$

where

$$\bar{v} = \sqrt{\frac{8k_{\mathrm{B}}T_{\mathrm{e}}}{\pi m_{\mathrm{e}}}}.$$

When the probe potential is equal to the plasma potential, i.e. ($\Delta\phi$=0). The electron flux arriving to the probe is written as

$$\Gamma = \frac{n_{\mathrm{o}}}{4}\sqrt{\frac{8k_{\mathrm{B}}T_{\mathrm{e}}}{\pi m_{\mathrm{e}}}}.$$

The electron current when $\Delta\phi$=0 is $I_{\mathrm{SAT}} = e\Gamma A_{\mathrm{p}}$. Therefore, the electron density can be written as

$$n_{\mathrm{o}} = \frac{I_{\mathrm{SAT}}}{eA_{\mathrm{p}}\sqrt{(k_{\mathrm{B}}T_{\mathrm{ex}})/(2\pi m_{\mathrm{e}})}}.$$

A.3 IVDF from the first derivative of an I-V curve

Ions arriving to the collector establish the ion current as following.

$$\begin{aligned} I_{\mathrm{c}} &= \chi A e < n v > \\ &= \chi A e \int v f_{\mathrm{i}}(v) \mathrm{d}v \end{aligned}$$

Due to

$$\begin{aligned} \frac{1}{2} M_{\mathrm{i}} v^2 &= e\left(\Phi - V_{\mathrm{d}}\right) \\ \mathrm{d}\left(\frac{1}{2} M_{\mathrm{i}} v^2\right) &= \mathrm{d}\left[e\left(\Phi - V_{\mathrm{d}}\right)\right] \\ M_{\mathrm{i}} v \mathrm{d}v &= -e \mathrm{d}V_{\mathrm{d}} \\ v \mathrm{d}v &= -\frac{e}{M_{\mathrm{i}}} \mathrm{d}V_{\mathrm{d}} \end{aligned}$$

Therefore

$$\begin{aligned} I_{\mathrm{c}} &= -\chi A e \int f_{\mathrm{i}}(v) \frac{e}{M_{\mathrm{i}}} \mathrm{d}V_{\mathrm{d}} \\ \frac{\mathrm{d}I_{\mathrm{c}}}{\mathrm{d}V_{\mathrm{d}}} &= -\frac{\chi A e^2}{M_{\mathrm{i}}} f_{\mathrm{i}}(v) \\ f_{\mathrm{i}}(v) &= -\frac{M_{\mathrm{i}}}{\chi A e^2} \frac{\mathrm{d}I_{\mathrm{c}}}{\mathrm{d}V_{\mathrm{d}}} \end{aligned}$$

A.4 The equations of circular motion

A point Q, in the polar coordinate, can be described with the radial coordinate r and the azimuthal coordinate φ or (r, φ), as shown in figure A.2. In vector field of applications, unit vectors of the polar coordinate the polar coordinate are $\hat{r}$ and $\hat{\varphi}$ which are related to the unit vectors $\hat{i}$ and $\hat{j}$ of the Cartesian (x, y) system as

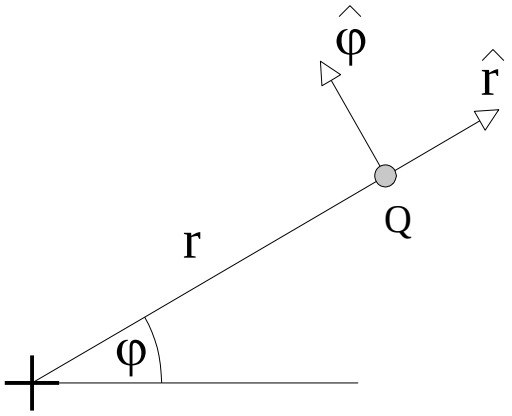

Figure A.2: A point Q in the polar coordinate (r, φ) with unit vectors $\hat{r}$ and $\hat{\varphi}$

$$\hat{r} = \hat{i}\cos(\varphi) + \hat{j}\sin(\varphi)$$
$$\hat{\varphi} = -\hat{i}\sin(\varphi) + \hat{j}\cos(\varphi)$$

A position vector in the polar coordinate can be represented by $\vec{r}$, for example $\vec{r} = r\hat{r}$ is the position vector of an object at the point Q. The vector velocity of the object is therefore

$$\vec{v} = \frac{\mathrm{d}}{\mathrm{d}t}(r\hat{r})$$
$$\vec{v} = \frac{\mathrm{d}r}{\mathrm{d}t}\hat{r} + r\frac{\mathrm{d}\hat{r}}{\mathrm{d}t}$$

Since

$$\frac{\mathrm{d}\hat{r}}{\mathrm{d}t} = \frac{\mathrm{d}\varphi}{\mathrm{d}t}\hat{\varphi},$$

then

$$\vec{v} = \frac{\mathrm{d}r}{\mathrm{d}t}\hat{r} + r\frac{\mathrm{d}\varphi}{\mathrm{d}t}\hat{\varphi},$$

or

$$\vec{v} = \dot{r}\hat{r} + r\omega\hat{\varphi},$$

where ω is the angular velocity of the object. Consequently, the vector of the acceleration $\vec{a}$ can be obtained from the derivative of the velocity vector $\vec{v}$ as

$$\vec{a} = \left(\ddot{r} - r(\dot{\varphi})^2\right)\hat{r} + \left(2\dot{r}\dot{\varphi} + r\ddot{\varphi}\right)\hat{\varphi}.$$

It means that the magnitude of the acceleration in $\hat{r}$ and $\hat{\varphi}$ component are

$$a_{\mathrm{r}} = \ddot{r} - r(\dot{\varphi})^2,$$

and

$$a_{\varphi} = 2\dot{r}\dot{\varphi} + r\ddot{\varphi},$$

respectively.

A.4.1 Radial force: $\vec{F}_{\mathrm{r}}$

The radial force $\vec{F}_{\mathrm{r}}$ can be determined from the radial electric field, $\vec{E}_{\mathrm{r}}$, written as

$$\vec{F}_{\mathrm{r}} = n_{\mathrm{i}} e \vec{E}_{\mathrm{r}}.$$

The radial electric field can be obtained from the gradient of plasma potential Φ as the expression of

$$\vec{E}_{\mathrm{r}} = -\hat{r}\frac{\mathrm{d}\varphi(r)}{\mathrm{d}r}$$

Using the fitted function $\varphi(r)$ in equation 7.6, the radial force can be written as

$$\vec{F}_{\mathrm{r}} = -\hat{r} n_{\mathrm{i}} e \, \frac{a\sqrt{2}\,(r - r_0)\exp\left(-\frac{(r-r_0)^2}{2w^2}\right)}{2w^3\sqrt{\pi}}$$

Using the fitting parameters of $r_0 = 12\,\mathrm{mm}$, $a = 0.21\,\mathrm{V}$ and $w = 7\,\mathrm{mm}$, the radius force $\vec{F}_{\mathrm{r}}$ can be plotted as shown in figure 7.6(a).

A.4.2 Drag force: $\vec{F}_{\mathrm{d}}$

Drag force is defined as

$$\vec{F}_{\mathrm{d}} = |\vec{F}_{\mathrm{d}}|\hat{d},$$

where $\hat{d}$ is the unit vector of the drag force. The magnitude of the drag force can be determined from

$$|\vec{F}_{\mathrm{d}}| = M n_{\mathrm{g}} \sigma \, |\vec{v}|^2$$

Since

$$|\vec{v}| = \sqrt{(\dot{r})^2 + (r\omega)^2},$$

therefore

$$|\vec{F}_{\mathrm{d}}| = M n_{\mathrm{g}} \sigma \left[(\dot{r})^2 + (r\omega)^2\right]$$

The unit vector of the drag force is defined as

$$\hat{d} = -\frac{\vec{v}}{|\vec{v}|}$$

Substituting for $\vec{v}$ and $|\vec{v}|$ gives

$$\hat{d} = -\left[\frac{\dot{r}}{\sqrt{(\dot{r})^2 + r^2\omega^2}}\hat{r} + \frac{r\omega}{\sqrt{(\dot{r})^2 + r^2\omega^2}}\hat{\varphi}\right].$$

Therefore, the drag force can thus be written as

$$\vec{F}_{\mathrm{d}} = -\frac{\vec{v}}{|\vec{v}|}$$

$$\vec{F}_{\mathrm{d}} = \left(-\dot{r}Mn_{\mathrm{g}}\sigma\sqrt{(\dot{r})^2 + r^2\omega^2}\right)\hat{r} + \left(-r\omega Mn_{\mathrm{g}}\sigma\sqrt{(\dot{r})^2 + r^2\omega^2}\right)\hat{\varphi}.$$

Appendix B

Gas oscillation

During HiPIMS discharges, the large amount of power density applied to the target causes an decrease in sputtering gas density in the target vicinity. The reduction of sputtering gas, known as gas rarefaction, is due to energy and momentum transfer from the energetic sputtered particles the the sputtering gas [38] and the direct loss from neutrals to ions of sputtering gas [46]. As a result, the target current can be reduced [46] or even shut off the discharge [94] owing to the lack of sputtering gas, for example argon ions, and of the subsequent secondary electrons emitted from the target surface. During the HiPIMS off-time, the energetic sputtered fluxes decay out. As a consequence, the remote sputtering gas species could diffuse back to the target region. Anders and Yushkov [94] have suggested that the returned flux of metastable argon neutrals can assist in the ignition process for the next HiPIMS pulse. In addition, Lundin *et al.* [46] have pointed out that the time that gas refill back by thermal velocity is in the range $50-100\,\mu$s.

If the width of HiPIMS pulses is long enough compared with the refilling period of sputtering gas, the rise of discharge current due to the returning of the sputtering gas should be observed. Consequently, the oscillation of the discharge current with a frequency associated with the gas loss and refill period would be expected. In this appendix, the oscillation of the waveforms of discharge voltage and current can be observed. The characteristic of the oscillation (for example amplitude, frequency and shape) are compared for a number of process conditions.

The experiments was conducted in the HiPIMS system as described in Section 5.2. A titanium target with a diameter of 75 mm was used as the magnetron target. The pressure of the vessel was initially reduced to the base of 5×10^{-4} Pa. The argon gas was introduced with a flow rate in range $5.00-0.65$ sccm to set the operating pressure in range $0.33-0.08$ Pa. In order to operate the HiPIMS at the low pressure range, the pre-ionisation technique was applied to the system (see Chapter 5). The width of HiPIMS pulses was fixed at 10 ms in order to observe the long term of the discharge dynamics. Using such long pulse width, it was necessary to decrease the pulse repetition rate

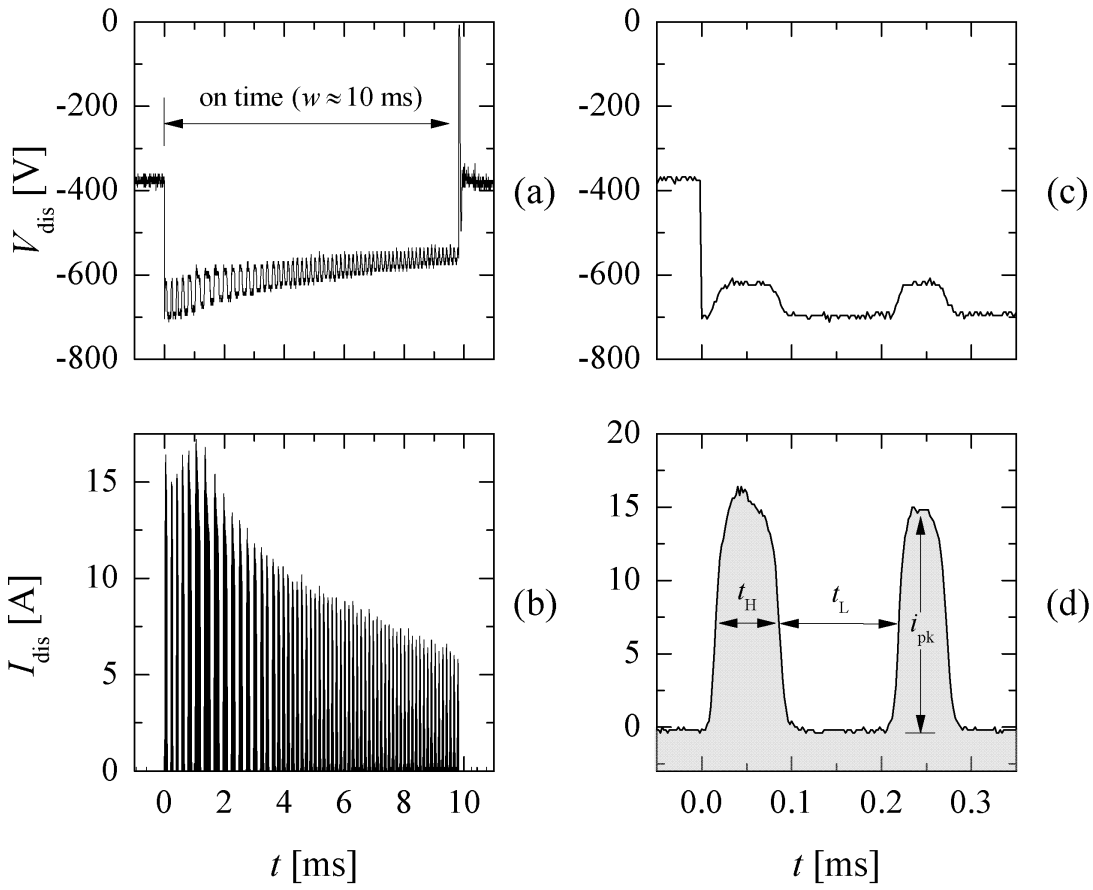

Figure B.1: The waveforms of (a) discharge voltage, V_{dis}, and (b) discharge current, I_{dis}, during a long pulsed HiPIMS discharge operated at the argon pressure of 0.10 Pa, a pulse width of 10 ms and a repetition rate of 0.8 Hz.

down to 0.8 Hz preventing the over range of the power dissipation during the discharge. Consequently, waveforms of the discharge voltage and current were captured in the single short mode. The process parameters and conditions are summarised in the table below.

Table B.1: The selected process parameters to observe the dynamics of long pulsed HiPIMS discharges.

Parameters	Symbol	Value	Unit
Ar Pressure	p	0.33 – 0.08	Pa
Pulse width	w	10	ms
Pulse repetition rate	f	0.8	Hz
Charging voltage	U_0	−450 to −800	V

Figure B.1 shows the waveforms of discharge voltage V_{dis} and discharge current I_{dis} during a 10 ms width of a HiPIMS pulse. The discharge was operated with the initial discharge voltage U_0 of ~ -700 V and at the argon pressure of 0.10 Pa. As shown in figure B.1(a) and (b), the oscillation is pronounced on V_{dis} waveform which accompanies

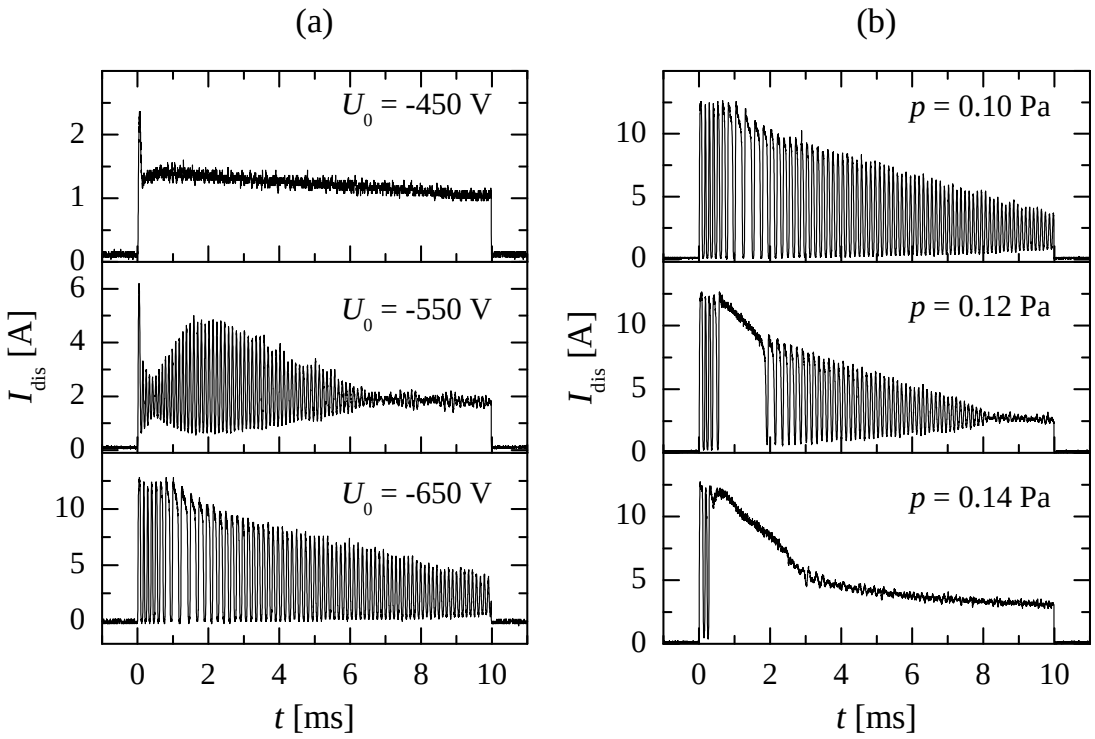

Figure B.2: The waveform of I_{dis} (a) for a number of the initial target voltage U_0 at $p = 0.10\,\text{Pa}$ and (b) for a number of the argon pressure p at $U_0 = -650\,\text{V}$.

by multi pulses in the waveforms of I_{dis}, called as current pulse-lets, throughout the pulse on-time. For example, the oscillation in the magnitude of V_{dis} between $-700\,\text{V}$ and $-600\,\text{V}$ and the variation of discharge current between zero and a peak (ranged in $10 - 17\,\text{A}$) are observed during the first few milliseconds.

The magnified plots for V_{dis} and I_{dis} during $t = 0 - 0.3\,\text{ms}$ are shown in figure B.1(c) and (d), respectively. The magnified plots clearly show that V_{dis} drops from the initial value U_0 of $\sim -700\,\text{V}$ to a value of $\sim -600\,\text{V}$ during the high current period (denoted by t_{H}). At $t \sim 0.09\,\text{ms}$, the discharge voltage returns close to U_0, while the discharge current sharply decreases to almost zero. The discharge current is still that low for a certain period of time (denoted by t_{L}). At $t \sim 0.2\,\text{ms}$, for example, a new current pulse-let is self formed which accompanies by an decrease in V_{dis}. The time interval t_{H} may be defined as the width at the half of the current peak ($i_{\text{pk}}/2$), which is $\sim 70\,\mu\text{s}$ for the first current pulse-let. Using the same idea, t_{L} is the time interval between two current pulse-lets ($\sim 130\,\mu\text{s}$) as shown in figure B.1(d). Using t_{L} and t_{H}, the frequency of the events is $1/(t_{\text{L}} + t_{\text{H}})$, which is approximately equal to 5,kHz.

The waveforms of HiPIMS current for a number of initial voltage U_0 are shown in figure B.2(a). Using a low U_0 of $-450\,\text{V}$, for example, there is no the strong oscillation of the current waveform. The target current jumps to a 2.5 A peak current at the pulse beginning followed by a lower stable level of 1.5 A for the rest of the pulse. Increasing U_0 to $-550\,\text{V}$, however, causes I_{dis} to oscillate around its equilibrium level of 2 A. It is

worth noting that the shape of the current waveform for this condition is nearly almost a sinusoidal waveform with a constant frequency of $\sim 9\,\mathrm{kHz}$. Further an increase in U_0 the shape of I_{dis} tends to change from the sinusoid to the pulse-let with lower frequencies. The oscillation of I_{dis} waveform can be clearly observed only at a low pressure range. As shown in figure B.2(b), I_{dis} stops to oscillate at the operating pressure of larger than $0.14\,\mathrm{Pa}$. The oscillation observed in V_{dis} and strongly in I_{dis} may be attributed to the cycles of Ar gas loss and refill in the target vicinity, explained as follows.

During the rising edge of HiPIMS current, dense argon ions are developed causing high fluxes of sputtered particles (Ti particles in this case). The Ti fluxes can effectively transfer their energy and momentum to the argon particles causing a reduction of argon density, known as gas rarefaction. Moreover, the region gas rarefaction may extend from the target surface up to $\sim 30\,\mathrm{mm}$ above the racetrack [42]. The gas rarefaction changes plasma composition from argon-ion dominated to metal-ion dominated plasma especially above the target racetrack. Since metal ions generally cannot produce the secondary electrons from the target [38], the discharge current, therefore, significantly decrease. In the case of the strong gas rarefaction, the discharge current may drop down to almost zero switching the discharge to the low current mode. The period of gas rarefaction may be indicated by t_{H} as seen in figure B.2(d). Since the sputtering process is paused during the low current mode, argon particles surrounding the the magnetron can be able to diffuse back or refill to the target surface. Lundin *et al.* [46] has pointed out that the gas refill process may take $50-100\,\mu\mathrm{s}$ for argon room temperature travelling $20\,\mathrm{mm}$ back to the target. Arriving of the argon gas consequently reignite the discharge and self-switch the discharge to the high current mode gain. Time for the refill process, therefore, may be indicated by t_{L} (see figure B.2(d)). The range of t_{L} observed in this study is between $75-125\,\mu\mathrm{s}$ which is the same order as suggested in [46].

In conclusion, the oscillation on the target current waveforms has been observed in a HiPIMS discharge with the Ti target operated at the low pressure range. The oscillation is postulated to be the cycle of gas loss and gas refill in front of the magnetron target. The high fluxes of titanium sputtered species cause the loss of argon gas in the target vicinity during the high current mode. The refill of the argon gas occurs during the low current mode. The returning of the argon gas to the target causes self ignition resulting in the next development of discharge current and sputtering process.

Appendix C

List of symbols

A_{tar}	target area
B_{r}	radial component of magnetic field strength
B_{z}	axial component of magnetic field strength
Ψ_{i}	energy density of ions
ε_{e}	electron energy
ε_{i}	ion energy
$\mathrm{d}I_{\mathrm{c}}/\mathrm{d}V_{\mathrm{d}}$	first derivative of I-V curve
$f_{\mathrm{i}}(\varepsilon)$	ion energy distribution function
$f_{\mathrm{i}}(v)$	ion velocity distribution function
Γ_{i}	ion flux
Γ_{sp}	flux of sputtered particles
$g_{\mathrm{e}}(\varepsilon)$	electron energy distribution function
I_{c}	collector current
I_{dis}	discharge current
I_{e}	electron current
I_{ec}	current of cold electrons
I_{eh}	current of hot electrons
$I_{\mathrm{e,OML}}$	electron current calculated using OML theory
$I_{\mathrm{e,sat}}$	electron saturation current
I_{i}	ion current
$I_{\mathrm{i,OML}}$	ion current calculated using OML theory
$I_{\mathrm{i,sat}}$	ion saturation current
Θ	ionised metal flux fraction
I_{p}	probe current
I_{pk}	peak current
λ_{De}	Debye length
λ_{en}	mean free path of electron-neutral collisions
λ_{iex}	mean free path of ion charge exchange collisions
λ_{in}	mean free path of ion-neutral collisions
l_{p}	probe length
m_{e}	electron mass
$\langle\varepsilon_{\mathrm{i}}\rangle$	mean energy of ions
$\langle\Gamma_{\mathrm{i}}\rangle$	mean flux of ions
$\langle v_{\mathrm{i}}\rangle$	mean velocity of ions
$\langle v_{\mathrm{i}}^2\rangle$	mean square velocity of ions

M_i	ion mass
n_e	electron density
n_ec	density of cold electrons
n_eh	density of hot electrons
n_est	density of super thermal electrons
$n_\mathrm{e,EDF}$	electron density calculated using EEDF
$n_\mathrm{e,OML}$	electron density calculated using OML theory
$n_\mathrm{e,sat}$	electron density calculated using electron saturation current
n_g	gas density
n_i	ion density
$n_\mathrm{i,OML}$	ion density calculated using OML theory
n_n	neutral density
P_dis	discharge power
r_gy	Larmor radius
R_i	deposition rate of ions at the QCM
R_I	deposition rate of ions at the first grid
R_n	deposition rate of neutrals at the QCM
R_N	deposition rate of neutrals at the first grid
r_p	probe radius
R_t	total deposition rate at the QCM
R_T	total deposition rate at the first grid
σ_iex	cross section of ion charge collisions
t_d	delay time of I_dis onset
T_e	electron temperature
T_ec	temperature of cold electrons
T_eff	effective electron temperature
T_eh	temperature of hot electrons
T_est	temperature of super thermal electrons
U_bk	target voltage of the background discharge
U_0	peak voltage of HiPIMS pulse
V_b	probe bias voltage
V_d	discriminating voltage
V_dis	discharge voltage
$v_\mathrm{E\times B}$	E×B drift velocity
V_f	floating potential
V_Q	ion repelling voltage at the QCM
V_R	electron repelling voltage used in g-QCM
V_s	suppression voltage for secondary electrons

Bibliography

[1] U. Helmersson, M. Lattemann, J. Bohlmark, A. P. Ehiasarian, and J. T. Gudmundsson. Ionized physical vapor deposition (IPVD): A review of technology and applications. *Thin Solid Films*, 513(1-2):1–24, 2006.

[2] V. Kouznetsov, K. Macák, J. M. Schneider, U. Helmersson, and I. Petrov. A novel pulsed magnetron sputter technique utilizing very high target power densities. *Surf. Coat. Technol.*, 122(2-3):290–293, 1999.

[3] B. Chapman. *Glow discharge processes: sputtering and plasma etching.* Wiley-Interscience, 1980.

[4] M. A. Lieberman and A. J. Lichtenberg. *Principles of Plasma Discharges and Materials Processing.* Wiley-Interscience, 2005.

[5] R. A. Powell and S. M. Rossnagel. *PVD for Microelectronics; Sputter Deposition Applied to Semiconductor Manufacturing.* Academic Press, 1999.

[6] J. A. Hopwood. *Ionized Physical Vapor Deposition.* Academic Press, 2000.

[7] D. M. Mattox. *Handbook of Physical Vapor Deposition (PVD) Processing.* Elsevier, 2nd edition, 2010.

[8] J. A. Thornton. Magnetron sputtering: basic physics and application to cylindrical magnetrons. *J. Vac. Sci. Technol.*, 15(2):171, 1978.

[9] R. K. Waits. Planar magnetron sputtering. *J. Vac. Sci. Technol.*, 15(2):179, 1978.

[10] R.D Arnell and P.J Kelly. Recent advances in magnetron sputtering. *Surf. Coat. Technol.*, 112(13):170, 1999.

[11] I. Safi. Recent aspects concerning DC reactive magnetron sputtering of thin films: A review. *Surf. Coat. Technol.*, 127(23):203, 2000.

[12] P. J. Kelly and R. D. Arnell. Magnetron sputtering: a review of recent developments and applications. *Vacuum*, 56(3):159 – 172, 2000.

[13] S. Schiller, K. Goedicke, J. Reschke, V. Kirchhoff, S. Schneider, and F. Milde. Pulsed magnetron sputter technology. *Surf. Coat. Technol.*, 61(13):331 – 337, 1993.

[14] J. T. Gudmundsson, N. Brenning, D. Lundin, and U. Helmersson. High power impulse magnetron sputtering discharge. *J. Vac. Sci. Technol. A*, 30(3):030801, 2012.

[15] J. Weichart, M. Elghazzali, S. Kadlec, and A. P. Ehiasarian. PVD processes in high aspect ratio features by HIPIMS. In *SVC - 52nd Annual Technical Conference of Society of Vacuum Coaters*, page 201, Santa Clara, CA USA, 2009.

[16] J. Robertson. Diamond-like amorphous carbon. *Mater. Sci. Eng. R*, 37(4):129–281, 2002.

[17] B. M. DeKoven, P. R. Ward, R. E. Weiss, D. J. Christie, R. A. Scholl, W. D. Sproul, F. Tomasel, and A. Anders. Carbon thin film deposition using high power pulsed magnetron sputtering. In *SVC - 46th Annual Technical Conference Proceedings of the Society of Vacuum Coaters*, page 158, San Francisco, CA, USA, 2003.

[18] A. Aijaz, K. Sarakinos, D. Lundin, N. Brenning, and U. Helmersson. A strategy for increased carbon ionization in magnetron sputtering discharges. *Diamond Relat. Mater.*, 23(0):1–4, 2012.

[19] E. Wallin, T. I. Selinder, M. Elfwing, and U. Helmersson. Synthesis of α-al$_2$o$_3$ thin films using reactive high-power impulse magnetron sputtering. *EPL (Europhysics Letters)*, 82(3):36002, 2008.

[20] S. Konstantinidis, J. P. Dauchot, and M. Hecq. Titanium oxide thin films deposited by high-power impulse magnetron sputtering. *Thin Solid Films*, 515(3):1182 – 1186, 2006.

[21] A. P. Ehiasarian, W. D. Mnz, L. Hultman, U. Helmersson, and I. Petrov. High power pulsed magnetron sputtered CrN$_x$ films. *Surf. Coat. Technol.*, 163-164:267–272, 2003.

[22] M. Lattemann, U. Helmersson, and J. E. Greene. Fully dense, non-faceted 111-textured high power impulse magnetron sputtering TiN films grown in the absence of substrate heating and bias. *Thin Solid Films*, 518(21):5978 – 5980, 2010.

[23] R. Machunze, A. P. Ehiasarian, F. D. Tichelaar, and G.C.A.M. Janssen. Stress and texture in HIPIMS TiN thin films. *Thin Solid Films*, 518(5):1561 – 1565, 2009.

[24] M. Aiempanakit, U. Helmersson, A. Aijaz, P. Larsson, R. Magnusson, J. Jensen, and T. Kubart. Effect of peak power in reactive high power impulse magnetron sputtering of titanium dioxide. *Surf. Coat. Technol.*, 205(20):4828 – 4831, 2011.

[25] D. Lundin and K. Sarakinos. An introduction to thin film processing using high-power impulse magnetron sputtering. *J. Mater. Res.*, 27(5):780, 2012.

[26] K. Sarakinos, J. Alami, and S. Konstantinidis. High power pulsed magnetron sputtering: A review on scientific and engineering state of the art. *Surf. Coat. Technol.*, 204(11):1661–1684, 2010.

[27] O. R. Monteiro. Thin film synthesis by energetic condensation. *Annu. Rev. Mater. Res.*, 31:111, 2001.

[28] A. P. Ehiasarian, P. Eh. Hovsepian, L. Hultman, and U. Helmersson. Comparison of microstructure and mechanical properties of chromium nitride-based coatings deposited by high power impulse magnetron sputtering and by the combined steered cathodic arc/unbalanced magnetron technique. *Thin Solid Films*, 457(2):270–277, 2004.

[29] K. Sarakinos, J. Wördenweber, F. Uslu, P. Schulz, J. Alami, and M. Wuttig. The effect of the microstructure and the surface topography on the electrical properties of thin Ag films deposited by high power pulsed magnetron sputtering. *Surf. Coat. Technol.*, 202(11):2323, 2008.

[30] J. Alami, K. Sarakinos, F. Uslu, and M. Wuttig. On the relationship between the peak target current and the morphology of chromium nitride thin films deposited by reactive high power pulsed magnetron sputtering. *J. Phys. D: Appl. Phys.*, 42(1):015304, 2009.

[31] J. Alami, P. O. A. Persson Persson, D. Music, J. T. Gudmundsson, J. Bohlmark, and U. Helmersson. Ion-assisted physical vapor deposition for enhanced film properties on nonflat surfaces. *J. Vac. Sci. Technol. A*, 23(2):278–280, 2005.

[32] J. Alami, S. Bolz, and K. Sarakinos. High power pulsed magnetron sputtering: Fundamentals and applications. *Journal of Alloys and Compounds*, 483(1-2):530–534, 2009.

[33] J. Lin, J. J. Moore, W. D. Sproul, S. L. Lee, and J. Wang. Effect of Negative Substrate Bias on the Structure and Properties of Ta Coatings Deposited Using Modulated Pulse Power Magnetron Sputtering. *IEEE Trans. Plasma Sci.*, 38:3071, 2010.

[34] M. Lattemann, A. P. Ehiasarian, J. Bohmark, P. A. O. Persson, and U. Helmersson. Investigation of high power impulse magnetron sputtering pretreated interfaces for adhesion enhancement of hard coatings on steel. *Surf. Coat. Technol.*, 200(22-23):6495–6499, 2006.

[35] C. Reinhard, A. P. Ehiasarian, and P. Eh. Hovsepian. CrN/NbN superlattice structured coatings with enhanced corrosion resistance achieved by high power impulse magnetron sputtering interface pre-treatment. *Thin Solid Films*, 515:3685, 2007.

[36] A. P. Ehiasarian, J. G. Wen, and I. Petrov. Interface microstructure engineering by high power impulse magnetron sputtering for the enhancement of adhesion. *J. Appl. Phys.*, 101:054301, 2007.

[37] A. Anders. Self-sputtering runaway in high power impulse magnetron sputtering: The role of secondary electrons and multiply charged metal ions. *Appl. Phys. Lett.*, 92(20):201501, 2008.

[38] A. Anders. Discharge physics of high power impulse magnetron sputtering. *Surface and Coatings Technology*, 205, Supplement 2(0):S1 – S9, 2011.

[39] J. T. Gudmundsson. Ionization mechanism in the high power impulse magnetron sputtering (HiPIMS) discharge. *J. Phys.: Conf. Ser.*, 100(8):082013, 2008.

[40] M. A. Raadu, I. Axns, J. T. Gudmundsson, C. Huo, and N. Brenning. An ionization region model for high-power impulse magnetron sputtering discharges. *Plasma Sources Sci. Technol.*, 20(6):065007, 2011.

[41] J. Alami, K. Sarakinos, G. Mark, and M. Wuttig. On the deposition rate in a high power pulsed magnetron sputtering discharge. *Appl. Phys. Lett.*, 89(15):154104, 2006.

[42] S. Kadlec. Simulation of neutral particle flow during high power magnetron impulse. *Plasma Processes and Polymers*, 4(S1):S419–S423, 2007.

[43] C. Vitelaru, D. Lundin, G. D. Stancu, N. Brenning, J. Bretagne, and T. Minea. Argon metastables in HiPIMS: time-resolved tunable diode-laser diagnostics. *Plasma Sources Sci. Technol.*, 21(2):025010, 2012.

[44] C. Huo, M. A. Raadu, D. Lundin, J. T. Gudmundsson, A. Anders, and N. Brenning. Gas rarefaction and the time evolution of long high-power impulse magnetron sputtering pulses. *Plasma Sources Sci. Technol.*, 21(4):045004, 2012.

[45] A. Anders, J. Andersson, and A. Ehiasarian. High power impulse magnetron sputtering: Current-voltage-time characteristics indicate the onset of sustained self-sputtering. *J. Appl. Phys.*, 102(11):113303, 2007.

[46] D. Lundin, N. Brenning, D. Jädernäs, P. Larsson, E. Wallin, M. Lattemann, M. A. Raadu, and U. Helmersson. Transition between the discharge regimes of high power impulse magnetron sputtering and conventional direct current magnetron sputtering. *Plasma Sources Sci. Technol.*, 18(4):045008, 2009.

[47] J. Andersson and A. Anders. Gasless sputtering: Opportunities for ultraclean metallization, coatings in space, and propulsion. *Appl. Phys. Lett.*, 92(22):221503, 2008.

[48] A. Anders, J. Capek, M. Hala, and L. Martinu. The recycling trap: a generalized explanation of discharge runaway in high-power impulse magnetron sputtering. *J. Phys. D: Appl. Phys.*, 45(1):012003, 2012.

[49] M. Samuelsson, D. Lundin, J. Jensen, M. A. Raadu, J. T. Gudmundsson, and U. Helmersson. On the film density using high power impulse magnetron sputtering. *Surf. Coat. Technol.*, 205(2):591–596, 2010.

[50] A. Mishra, P. J. Kelly, and J. W. Bradley. The evolution of the plasma potential in a HiPIMS discharge and its relationship to deposition rate. *Plasma Sources Sci. Technol.*, 19(4):045014, 2010.

[51] A. Anders. Deposition rates of high power impulse magnetron sputtering: Physics and economics. *J. Vac. Sci. Technol. A*, 28(4):783–790, 2010.

[52] S. Konstantinidis, J. P. Dauchot, M. Ganciu, A. Ricard, and M. Hecq. Influence of pulse duration on the plasma characteristics in high-power pulsed magnetron discharges. *J. Appl. Phys.*, 99(1):013307, 2006.

[53] D. Lundin, P. Larsson, E. Wallin, M. Lattemann, N. Brenning, and U. Helmersson. Cross-field ion transport during high power impulse magnetron sputtering. *Plasma Sources Sci. Technol.*, 17(3):035021, 2008.

[54] J. T. Gudmundsson. The high power impulse magnetron sputtering discharge as an ionized physical vapor deposition tool. *Vacuum*, 84(12):1360, 2010.

[55] J. T. Gudmundsson, P. Sigurjonsson, P. Larsson, D. Lundin, and U. Helmersson. On the electron energy in the high power impulse magnetron sputtering discharge. *J. Appl. Phys.*, 105(12):123302, 2009.

[56] J. Bohlmark, J.T. Gudmundsson, J. Alami, M. Latteman, and U. Helmersson. Spatial electron density distribution in a high-power pulsed magnetron discharge. *IEEE Trans. Plasma Sci.*, 33(2):346, 2005.

[57] A. P. Ehiasarian, R. New, W. D. Münz, L. Hultman, U. Helmersson, and V. Kouznetsov. Influence of high power densities on the composition of pulsed magnetron plasmas. *Vacuum*, 65(2):147–154, 2002.

[58] I. Swindells, J. W. Bradley, and P. J. Kelly. Spatially-resolved optical emission from a bi-polar pulsed DC magnetron discharge. *Surf. Coat. Technol.*, 203(3-4):391–395, 2008.

[59] K. Macák, V. Kouznetsov, J. Schneider, U. Helmersson, and I. Petrov. Ionized sputter deposition using an extremely high plasma density pulsed magnetron discharge. *J. Vac. Sci. Technol. A*, 18(4 II):1533–1537, 2000.

[60] J. Bohlmark, M. Lattemann, J. T. Gudmundsson, A. P. Ehiasarian, Y. Aranda Gonzalvo, N. Brenning, and U. Helmersson. The ion energy distributions and ion flux composition from a high power impulse magnetron sputtering discharge. *Thin Solid Films*, 515(4):1522–1526, 2006.

[61] A. Hecimovic and A. P. Ehiasarian. Time evolution of ion energies in HIPIMS of chromium plasma discharge. *J. Phys. D: Appl. Phys.*, 42(13):135209, 2009.

[62] S. Kadlec, C. Quaeyhaegens, G. Knuyt, and L. M. Stals. Energy distribution of ions in an unbalanced magnetron plasma measured with energy-resolved mass spectrometry. *Surf. Coat. Technol.*, 89:177 – 184, 1997.

[63] A. Hecimovic, K. Burcalova, and A. P. Ehiasarian. Origins of ion energy distribution function (IEDF) in high power impulse magnetron sputtering (HIPIMS) plasma discharge. *J. Phys. D: Appl. Phys.*, 41(9):095203, 2008.

[64] G. Greczynski and L. Hultman. Time and energy resolved ion mass spectroscopy studies of the ion flux during high power pulsed magnetron sputtering of Cr in Ar and Ar/N_2 atmospheres. *Vacuum*, 84(9):1159–1170, 2010.

[65] F. F. Chen and J. P. Chang. *Lecture Notes on Principles of Plasma Processing.* Plenum/Kluwer, 2002.

[66] L. S. Pilling and D. A. Carnegie. Validating experimental and theoretical langmuir probe analyses. *Plasma Sources Sci. Technol.*, 16(3):570–580, 2007.

[67] F. F. Chen. Langmuir probes in RF plasma: surprising validity of OML theory. *Plasma Sources Sci. Technol.*, 18(3):035012, 2009.

[68] F. Magnus and J. T. Gudmundsson. Digital smoothing of the Langmuir probe I-V characteristic. *Rev. Sci. Instrum.*, 79(7):073503, 2008.

[69] S. Jager, B. Szyszka, J. Szczyrbowski, and G. Brauer. Comparison of transparent conductive oxide thin films prepared by a.c. and d.c. reactive magnetron sputtering. *Surf. Coat. Technol.*, 98(1-3):1304–1314, 1998.

[70] S. G. Ingram and N. S. J. Braithwaite. Ion and electron-energy analysis at a surface in an rf discharge. *Journal of Physics D-Applied Physics*, 21(10):1496–1503, 1988.

[71] C. Bohm and J. Perrin. Retarding-field analyzer for measurements of ion energy-distributions and secondary-electron emission coefficients in low-pressure radio-frequency discharges. *Review of Scientific Instruments*, 64(1):31–44, 1993.

[72] J. R. Woodworth, M. E. Riley, D. C. Meister, B. P. Aragon, M. S. Le, and H. H. Sawin. Ion energy and angular distributions in inductively coupled radio frequency discharges in argon. *J. Appl. Phys.*, 80(3):1304–1311, 1996.

[73] E. A. Edelberg, A. Perry, N. Benjamin, and E. S. Aydil. Compact floating ion energy analyzer for measuring energy distributions of ions bombarding radio-frequency biased electrode surfaces. *Review of Scientific Instruments*, 70(6):2689–2698, 1999.

[74] D. Gahan, B. Dolinaj, and M. B. Hopkins. Retarding field analyzer for ion energy distribution measurements at a radio-frequency biased electrode. *Review of Scientific Instruments*, 79(3):033502, 2008.

[75] C. Hayden, D. Gahan, and M. B. Hopkins. Ion energy distributions at a capacitively and directly coupled electrode immersed in a plasma generated by a remote source. *Plasma Sources Sci. Technol.*, 18(2):025018, 2009.

[76] G. D. Conway, A. J. Perry, and R. W. Boswell. Evolution of ion and electron energy distributions in pulsed helicon plasma discharges. *Plasma Sources Sci. Technol.*, 7(3):337–347, 1998.

[77] J. Prager, R. Winglee, T. Ziemba, B. R. Roberson, and G. Quetin. Ion energy characteristics downstream of a high power helicon. *Plasma Sources Sci. Technol.*, 17(2):025003, 2008.

[78] T. Baloniak, R. Reuter, C. Flotgen, and A. von Keudell. Calibration of a miniaturized retarding field analyzer for low-temperature plasmas: geometrical transparency and collisional effects. *Journal of Physics D-Applied Physics*, 43(5):055203, 2010.

[79] S. G. Ingram, B. M. Annaratone, and M. Ohuchi. Design and use of a gridded probe in a low-pressure rf argon discharge. *Review of Scientific Instruments*, 61(7):1883–1891, 1990.

[80] B. M. Smirnov. Tables for cross sections of the resonant charge exchange process. *Physica Scripta*, 61(5):595–602, 2000.

[81] J. E. Allen. On the plotting of electron and ion distribution functions. *J. Phys. D: Appl. Phys.*, 25(12):1839, 1992.

[82] P. Chabert and N. St. J. Braithwaite. *Physics of Radio-Frequency Plasmas*. Cambridge university Press, 2011.

[83] S. M. Rossnagel and J. Hopwood. Magnetron sputter deposition with high levels of metal ionization. *Appl. Phys. Lett.*, 63(24):3285, 1993.

[84] K. M. Green, D. B. Hayden, D. R. Juliano, and D. N. Ruzic. Determination of flux ionization fraction using a quartz crystal microbalance and a gridded energy analyzer in an ionized magnetron sputtering system. *Rev. Sci. Instrum.*, 68(12):4555, 1997.

[85] D. B. Hayden, D. R. Juliano, K. M. Green, D. N. Ruzic, C. A. Weiss, K. A. Ashtiani, and T. J. Licata. Characterization of magnetron-sputtered partially ionized aluminum deposition. *J. Vac. Sci. Technol. A*, 16(2):624–627, 1998.

[86] L. Meng, R. Raju, R. Flauta, H. Shin, D. N. Ruzic, and D. B. Hayden. In situ plasma diagnostics study of a commercial high-power hollow cathode magnetron deposition tool. *J. Vac. Sci. Technol. A*, 28(1):112–118, 2010.

[87] K. Nakamura, A. Wakayama, and K. Yukimura. Effects of reactive gas addition on ionization of metal atoms in droplet-free metal ion sources. *Surf. Coat. Technol.*, 201(15):6655, 2007.

[88] T. G. Snodgrass, J. H. Booske, W. Wang, A. E. Wendt, and J. L. Shohet. Gridless ionized metal flux fraction measurement tool for use in ionized physical vapor deposition studies. *Rev. Sci. Instrum.*, 70(2):1525, 1999.

[89] J. T. Gudmundsson, J. Alami, and U. Helmersson. Evolution of the electron energy distribution and plasma parameters in a pulsed magnetron discharge. *Appl. Phys. Lett.*, 78(22):3427–3429, 2001.

[90] A. Vetushka and A. P. Ehiasarian. Plasma dynamic in chromium and titanium HIPIMS discharges. *J. Phys. D: Appl. Phys.*, 41(1):015204, 2008.

[91] A. D. Pajdarová, J. Vlček, P. Kudláček, and J. Lukáš. Electron energy distributions and plasma parameters in high-power pulsed magnetron sputtering discharges. *Plasma Sources Sci. Technol.*, 18(2):025008, 2009.

[92] J. T. Gudmundsson, J. Alami, and U. Helmersson. Spatial and temporal behavior of the plasma parameters in a pulsed magnetron discharge. *Surf. Coat. Technol.*, 161(2-3):249–256, 2002.

[93] J. Alami, J. T. Gudmundsson, J. Bohlmark, J. Birch, and U. Helmersson. Plasma dynamics in a highly ionized pulsed magnetron discharge. *Plasma Sources Sci. Technol.*, 14(3):525–531, 2005.

[94] A. Anders and G. Y. Yushkov. Plasma "anti-assistance" and "self-assistance" to high power impulse magnetron sputtering. *J. Appl. Phys.*, 105(7):073301, 2009.

[95] H. Bäcker and J. W. Bradley. Observations of the long-term plasma evolution in a pulsed dc magnetron discharge. *Plasma Sources Sci. Technol.*, 14(3):419–431, 2005.

[96] N. Brenning, I. Axns, M. A. Raadu, D. Lundin, and U. Helmerson. A bulk plasma model for dc and HiPIMS magnetrons. *Plasma Sources Sci. Technol.*, 17(4):045009, 2008.

[97] T. A. Van Der Straaten, N. F. Cramer, I. S. Falconer, and B. W. James. The cylindrical DC magnetron discharge: II. The negative space charge mode. *J. Phys. D: Appl. Phys.*, 31(2):191–206, 1998.

[98] J. W. Bradley and T. Welzel. Physics and phenomena in pulsed magnetrons: An overview. *J. Phys. D: Appl. Phys.*, 42(9):093001, 2009.

[99] J. W. Bradley, H. Bäcker, P. J. Kelly, and R. D. Arnell. Time-resolved Langmuir probe measurements at the substrate position in a pulsed mid-frequency DC magnetron plasma. *Surf. Coat. Technol.*, 135(2-3):221–228, 2001.

[100] S. W. Lee, S. H. Seo, J. H. In, C. W. Chung, and H. Y. Chang. Characterization of pulsed plasma in unbalanced magnetron argon discharge. *Phys. Plasmas*, 12(6):063502, 2005.

[101] S.-H. Seo, J.-H. In, and H.-Y. Chang. Experimental investigation of plasma dynamics in dc and short-pulse magnetron discharges. *Plasma Sources Sci. Technol.*, 15(2):256, 2006.

[102] P. Poolcharuansin and J. W. Bradley. Short- and long-term plasma phenomena in a HiPIMS discharge. *Plasma Sources Sci. Technol.*, 19(2):025010, 2010.

[103] H. Bäcker, J. W. Bradley, P. J. Kelly, and R. D. Arnell. Using Langmuir probes to measure the plasma decay rates in pulsed RF magnetron discharges. *J. Phys. D: Appl. Phys.*, 34(18):2709–2714, 2001.

[104] A. Anders. *Cathodic Arcs: From Fractal Spots to Energetic Condensation.* Springer, 2008.

[105] R. A. Powell and S. M. Rossnagel. *PVD for Microelectronics; Sputter Deposition Applied to Semiconductor Manufacturing.* Academic Press, 1999.

[106] J. A. Thornton. Influence of apparatus geometry and deposition conditions on the structure and topography of thick sputtered coatings. *J. Vac. Sci. Technol.*, 11(4):666–670, 1974.

[107] S. M. Rossnagel, M. A. Russak, and J. J. Cuomo. Pressure and plasma effects on the properties of magnetron sputtered carbon films. *J. Vac. Sci. Technol. A*, 5(4):2150–2153, 1987.

[108] V. Assunção, E. Fortunato, A. Marques, H. acuteAguas, I. Ferreira, M. Costa, and R. Martins. Influence of the deposition pressure on the properties of transparent and conductive ZnO:Ga thin-film produced by r.f. sputtering at room temperature. *Thin Solid Films*, 427(1-2):401–405, 2003.

[109] J. J. Cuomo and S. M. Rossnagel. Hollow-cathode-enhanced magnetron sputtering. *J. Vac. Sci. Technol. A*, 4(3):393, 1986.

[110] J. Xu, X. Deng, S. Yu, W. Lu, and T. Ma. Plasma enhanced direct current planar magnetron sputtering technique employing a twinned microwave electron cyclotron resonance plasma source. *J. Vac. Sci. Technol. A*, 19(2):425–428, 2001.

[111] W. Posadowski. Low pressure magnetron sputtering using ionized, sputtered species. *Surf. Coat. Technol.*, 49(1-3):290–292, 1991.

[112] S. Kadlec and J. Musil. Low pressure magnetron sputtering and selfsputtering discharges. *Vacuum*, 47(3):307–311, 1996.

[113] S. Kadlec and J. Musil. Optimized magnetic field shape for low pressure magnetron sputtering. *J. Vac. Sci. Technol. A*, 13(2):389–393, 1995.

[114] W. M. Posadowski. Plasma parameters of very high target power density magnetron sputtering. *Thin Solid Films*, 392(2):201–207, 2001.

[115] I. V. Svadkovski, D. A. Golosov, and S. M. Zavatskiy. Characterisation parameters for unbalanced magnetron sputtering systems. *Vacuum*, 68(4):283–290, 2002.

[116] J. W. Bradley, D. M. Willett, and Y. Aranda Gonzalvo. Hollow cathode magnetrons with target gas feed. *J. Vac. Sci. Technol. A*, 17(6):3333–3339, 1999.

[117] J. Musil, P. Baroch, H. Poláková, J. Vlček, K. H. Nam, and J. G. Han. Magnetron with gas injection through hollow cathodes machined in sputtered target. *Surf. Coat. Technol.*, 148(2-3):296–304, 2001.

[118] S. P. Bugaev, V. G. Podkovyrov, K. V. Oskomov, S. V. Smaykina, and N. S. Sochugov. Ion-assisted pulsed magnetron sputtering deposition of ta-C films. *Thin Solid Films*, 389(1-2):16–26, 2001.

[119] P. Vašina, M. Meško, M. Ganciu, J. Bretagne, C. Boisse-Laporte, L. De Poucques, and M. Touzeau. Reduction of transient regime in fast preionized high-power pulsed-magnetron discharge. *Europhys. Lett.*, 72(3):390–395, 2005.

[120] P. Vašina, M. Meško, J. C. Imbert, M. Ganciu, C. Boisse-Laporte, L. De Poucques, M. Touzeau, D. Pagnon, and J. Bretagne. Experimental study of a preionized high power pulsed magnetron discharge. *Plasma Sources Sci. Technol.*, 16(3):501–510, 2007.

[121] P. Vašina, M. Meško, L. De Poucques, J. Bretagne, C. Boisse-Laporte, and M. Touzeau. Study of a fast high power pulsed magnetron discharge: Role of plasma deconfinement on the charged particle transport. *Plasma Sources Sci. Technol.*, 17(3):035007, 2008.

[122] R. Bandorf, S. Falkenau, K. Schiffmann, H. Gerdes, and U. Heckmann. Properties of nichrome sputtered by HIPIMS in unipolar and DC-superimposed mode. In *SVC - 51st Annual Technical Conference Proceedings*, pages 317–320, Chicago, IL USA, 2008.

[123] P. Kudláček, J. Vlček, K. Burcalová, and J. Lukáš. Highly ionized fluxes of sputtered titanium atoms in high-power pulsed magnetron discharges. *Plasma Sources Sci. Technol.*, 17(2):025010, 2008.

[124] J. Andersson, A. P. Ehiasarian, and A. Anders. Observation of Ti^{4+} ions in a high power impulse magnetron sputtering plasma. *Appl. Phys. Lett.*, 93(7):071504, 2008.

[125] A. P. Ehiasarian, Y. A. Gonzalvo, and T. D. Whitmore. Time-resolved ionisation studies of the high power impulse magnetron discharge in mixed argon and nitrogen atmosphere. *Plasma Process. Polym.*, 4(S1):S309–S313, 2007.

[126] J. Vlček, P. Kudláček, K. Burcalová, and J. Musil. High-power pulsed sputtering using a magnetron with enhanced plasma confinement. *J. Vac. Sci. Technol. A*, 25(1):42–47, 2007.

[127] J. Lin, J. J. Moore, W. D. Sproul, B. Mishra, J. A. Rees, Z. Wu, R. Chistyakov, and B. Abraham. Ion energy and mass distributions of the plasma during modulated pulse power magnetron sputtering. *Surf. Coat. Technol.*, 203(24):3676–3685, 2009.

[128] J. A. Thornton and D.W. Hoffman. Stress-related effects in thin films. *Thin Solid Films*, 171(1):5 – 31, 1989.

[129] A. Hecimovic and A. P. Ehiasarian. Spatial and temporal evolution of ion energies in high power impulse magnetron sputtering plasma discharge. *J. Appl. Phys.*, 108(6):063301, 2010.

[130] J. Alami, K. Sarakinos, F. Uslu, C. Klever, J. Dukwen, and M. Wuttig. On the phase formation of titanium oxide films grown by reactive high power pulsed magnetron sputtering. *J. Phys. D: Appl. Phys.*, 42(11):115204, 2009.

[131] J. Alami, P. Eklund, J. M. Andersson, M. Lattemann, E. Wallin, J. Bohlmark, P. Persson, and U. Helmersson. Phase tailoring of Ta thin films by highly ionized pulsed magnetron sputtering. *Thin Solid Films*, 515(7-8):3434–3438, 2007.

[132] J. Alami, P. Eklund, J. Emmerlich, O. Wilhelmsson, U. Jansson, H. Hogberg, L. Hultman, and U. Helmersson. High-power impulse magnetron sputtering of Ti-Si-C thin films from a Ti_3SiC_2 compound target. *Thin Solid Films*, 515(4):1731–1736, 2006.

[133] A. Aijaz, D. Lundin, P. Larsson, and U. Helmersson. Dual-magnetron open field sputtering system for sideways deposition of thin films. *Surf. Coat. Technol.*, 204(14):2165–2169, 2010.

[134] J. Andersson and A. Anders. Self-sputtering far above the runaway threshold: An extraordinary metal-ion generator. *Phys. Rev. Lett.*, 102(4):045003, 2009.

[135] D. Horwat and A. Anders. Compression and strong rarefaction in high power impulse magnetron sputtering discharges. *J. Appl. Phys.*, 108(12):123306, 2010.

[136] J. Bohlmark, U. Helmersson, M. VanZeeland, I. Axnäs, J. Alami, and N. Brenning. Measurement of the magnetic field change in a pulsed high current magnetron discharge. *Plasma Sources Sci. Technol.*, 13(4):654, 2004.

[137] D. Lundin, U. Helmersson, S. Kirkpatrick, S. Rohde, and N. Brenning. Anomalous electron transport in high power impulse magnetron sputtering. *Plasma Sources Sci. Technol.*, 17(2):025007, 2008.

[138] N. Brenning, R. L. Merlino, D. Lundin, M. A. Raadu, and U. Helmersson. Faster-than-Bohm Cross-B Electron Transport in Strongly Pulsed Plasmas. *Phys. Rev. Lett.*, 103(22):225003, 2009.

[139] S. M. Rossnagel and H. R. Kaufman. Langmuir probe characterization of magnetron operation. *J. Vac. Sci. Technol. A*, 4:1822, 1986.

[140] A. D. Polyanin and A. I. Chernoutsan. *A Concise Handbook of Mathematics, Physics, and Engineering Sciences*. CRC Press, Taylor & Francis Group, 2011.

[141] D. Halliday, R. Resnick, and J. Walker. *Fundamentals of physics*. John Wiley & Sons, Inc., 2011.

[142] J. M. Sanders, A. Rauch, R. J. Mendelsberg, and A. Anders. A synchronized emissive probe for time-resolved plasma potential measurements of pulsed discharges. *Review of Scientific Instruments*, 82(9):093505, 2011.

[143] S. M. Rossnagel. Directional and ionized physical vapor deposition for microelectronics applications. *J. Vac. Sci. Technol. B*, 16:2585, 1998.

[144] V. Sittinger, F. Ruske, W. Werner, C. Jacobs, B. Szyszka, and D.J. Christie. High power pulsed magnetron sputtering of transparent conducting oxides. *Thin Solid Films*, 516(17):5847, 2008.

[145] N. Brenning, C. Huo, D. Lundin, M. A. Raadu, C. Vitelaru, G. D. Stancu, T. Minea, and U. Helmersson. Understanding deposition rate loss in high power impulse magnetron sputtering: I. Ionization-driven electric fields. *Plasma Sources Sci. and Technol.*, 21(2):025005, 2012.

[146] M. Hála, J. Čapek, O. Zabeida, J. E. Klemberg-Sapieha, and L. Martinu. Pulse management in high power pulsed magnetron sputtering of niobium. *Surf. Coat. Technol.*, 206(19):4186, 2012.

[147] A. Rauch, R. J. Mendelsberg, J. M. Sanders, and A. Anders. Plasma potential mapping of high power impulse magnetron sputtering discharges. *J. Appl. Phys.*, 111(8):083302, 2012.

[148] A. Hecimovic and A. P. Ehiasarian. Temporal Evolution of the Ion Fluxes for Various Elements in HIPIMS Plasma Discharge. *IEEE Trans. Plasma Sci.*, 39(4):1154–1164, 2011.

[149] I. Petrov, F. Adibi, J. E. Greene, L. Hultman, and J.-E. Sundgren. Average energy deposited per atom: A universal parameter for describing ion-assisted film growth? *Appl. Phys. Lett.*, 63(1):36, 1993.

[150] S. M. Rossnagel. Gas density reduction effects in magnetrons. *J. Vac. Sci. Technol. A*, 6(1):19, 1988.

[151] J. E. Allen. Probe theory - the orbital motion approach. *Phys. Scripta*, 45(5):497, 1992.